Experimental Investigation of the Plasma-Wall Transition

DISSERTATION

zur Erlangung des akademischen Grades
doctor rerum naturalium
(Dr. rer. nat.)
im Fach Physik

eingereicht an der
Mathematisch-Naturwissenschaftlichen Fakultät I
Humboldt-Universität zu Berlin

von
Herr Dipl.-Phys. Tilmann Alexander Lunt
geboren am 27.09.1976 in Hamburg

Präsident der Humboldt-Universität zu Berlin:
Prof. Dr. Dr. h.c. Christoph Markschies

Dekan der Mathematisch-Naturwissenschaftlichen Fakultät I:
Prof. Dr. Christian Limberg

Gutachter:

1. Prof. Dr. Gerd Fußmann
2. Prof. Dr. Uwe Schumacher
3. Dr. habil. Hans-Stephan Bosch

eingereicht am:	14.2.2008
Tag der mündlichen Prüfung:	17.7.2008

Abstract

In the present work the streaming behavior of a magnetized argon plasma impinging on a neutralizing surface was investigated. For that purpose the ion velocity distribution was measured non-invasively as a function of the distance to the surface by means of Laser Induced Fluorescence. The spatial resolution was typically $\Delta z = 0.5$ mm.
Two situations are investigated, (a): when practically the whole plasma streams onto a large target ($\varnothing = 100$ mm), and (b): when the size of the target ($\varnothing = 15$ mm) is significantly smaller than the diameter of the plasma column. In both cases the streaming velocity u_i was at least as high as the ion acoustic sound speed, as already predicted by Bohm in 1949. Under fusion relevant conditions this is the first direct observation of the Bohm criterion. Approaching the target surface the Mach number $M = u/c_s$ increases from values of around 0.5 to 1 on typical scales of $\lambda_a = 30$ mm and $\lambda_b = 5$ mm, respectively. In order to explain these very short scale lengths the measured data were compared with a collisional-diffusive model in the case of (a) and with Hutchinson's model[27] in the case of (b). A good agreement was achieved in (a) by assuming a very low neutral gas temperature of about 400 K. In (b) the model fits the data excellently when the transport coefficient is chosen as high as $D = 20$ m^2/s. Such a high transport cannot be caused solely by diffusion. Partly it is explained by finite gyro-radii effects, but presumably time dependent phenomena, like drift waves, play an important role.
In addition the dependence on the angle between surface normal and B-field was investigated. The supersonic fluxes found in the immediate vicinity of the surface are described fairly well by the model developed by Chodura[10]. By contrast the size of the region, where Mach numbers greater one appear is significantly smaller than predicted.

Keywords:
plasma wall interaction, Bohm criterion, laser induced fluorescence, ion sensitive probes

Zusammenfassung

In der vorliegenden Arbeit wurde das Strömungsverhalten eines magnetisierten Argonplasmas beim Auftreffen auf eine neutralisierende Oberfläche untersucht. Mit Hilfe der Laserinduzierten Fluoreszenz wurde dazu nichtinvasiv die Geschwindigkeitsverteilung der Ionen mit einer Ortsauflösung von standardmäßig $\Delta z = 0.5$ mm als Funktion des Abstandes zur Oberfläche gemessen.
Zwei Situationen wurden untersucht (a): praktisch das ganze Plasma strömt auf ein großes Target ($\varnothing = 100$ mm) und (b) die Größe des Targets ist wesentlich kleiner ($\varnothing = 15$ mm) als der Durchmesser der Plasmasäule. Unmittelbar vor der Oberfläche war in beiden Fällen die Strömungsgeschwindigkeit u_i mindestens so groß wie die Ionenschallgeschwindigkeit c_s, genau wie von Bohm bereits 1949 vorhergesagt[3]. Unter fusionsrelevanten Bedingungen ist dies die erste direkte Beobachtung des Bohmkriteriums.
Bei Annäherung an die Oberfläche steigt die Machzahl $M = u/c_s$ von 0.5 auf 1 auf typischen Skalenlängen $\lambda_a = 30$ mm bzw. $\lambda_b = 5$ mm an. Um diese kurzen Längen erklären zu können wurden die Messdaten in (a) mit einem Stoß-Diffusionsmodell und im Falle von (b) mit dem Modell von Hutchinson[27] verglichen. Eine gute Übereinstimmung in (a) wurde erzielt, wenn eine sehr niedrige Neutralgastemperatur von etwa 400 K angenommen wird. Die Messdaten in (b) werden sehr gut durch das Modell wiedergegeben, wenn ein Transportkoeffizient von $D = 20$ m^2/s angenommen wird. Ein derartig hoher Transport kann unmöglich allein durch Diffusion verursacht werden. Teilweise kann dieser Transport anhand der endlichen Gyroradien erklärt werden, vermutlich aber spielen auch zeitabhängige Phänomene, wie z.B. Driftwellen eine wichtige Rolle.
Weiterhin wurde die Abhängigkeit von dem Winkel zwischen Flächennormalen und B-Feld untersucht. Die unmittelbar vor der Oberfläche auftretenden Überschallströmungen werden verhältnismäßig gut von dem Modell von Chodura[10] beschrieben. Im Gegensatz dazu ist die Größe der Zone in der Machzahlen größer eins auftreten deutlich kleiner, als vom Modell vorhergesagt.

Schlagwörter:
Plasma-Wand-Wechselwirkung, Bohm Kriterium, Laserinduzierte Fluoreszenz, Ionensensitive Sonden

Contents

Chapter 1

Introduction

While significant developments in technology have taken place over the last years, the most commonly used technique to supply energy has remained the same since the very beginning of humanity: the burning of organic fuels. However, over the last decades great efforts have been made to investigate nuclear fusion, which could one day provide a source of clean, safe and practically inexhaustible energy. To date, the most successful attempt to realize fusion is the Tokamak experiment developed in the former USSR in 1968. The idea is to confine a deuterium-tritium plasma in a magnetic field at such high temperatures that the thermal energies are sufficient to overcome the Coulomb repulsion of the nuclei and to enable their fusion. Every single fusion reaction releases an energy of 17.6 MeV, *i.e.* about six orders of magnitude more than a typical chemical reaction.
Initial assessments concerning the realizability of this technique were far too optimistic, and fusion was not reached within five or ten years as expected. Today in 2008, it is still an ongoing field of research. However, large improvements have been made over the last decades. The fusion product $nT_i\tau_E$ (where n is the electron density, T_i the ion temperature and τ_E the energy confinement time), an indicator for the progress made in fusion research, has increased by more than 5 orders of magnitude since the first serious attempts to create a fusion plasma.
In summer 2005, during my period as a PhD student, the decision was taken to build the International Thermonuclear Experimental Reactor ITER in Cadarache, France. This experiment aims to increase the fusion product by another factor of about five and to provide the final proof that energy can be gained from fusion.
In order to operate a fusion experiment clean plasma conditions are required. An important improvement was achieved in the 1980s by the application of a so called divertor. This is a magnetic configuration where the outermost

layer of the plasma (the so called scrape-off layer, SOL) is guided towards neutralizer plates located remotely from the bulk plasma, thus removing the impurities continuously. In order to make this removal most efficient and, at the same time, to limit the high power fluxes to the walls, it is essential to understand this plasma-wall transition.
Due to the limited accessibility, direct measurements in a fusion experiment are difficult to perform and one has to rely on numerical simulations (*e.g.* by means of the SOLPS code package) to optimize the divertor. All these calculations assume the so called Bohm criterion as an important boundary condition, which states that the streaming velocity u_i of the plasma has to reach at least the speed of sound c_s in the immediate vicinity of any solid obstacle exposed to the plasma.
This theorem, found by David Bohm [3] as early as 1949, is furthermore important for diagnostic purposes. Electrical probes, such as Langmuir or Mach probes, have to rely on theories and in particular on the Bohm criterion, to deduce plasma parameters from the measured currents and voltages. For all these reasons this so called plasma-wall interaction has become an important branch of plasma physics. In this dissertation I investigate different aspects of this field of research from an experimental approach.
Different authors have investigated the plasma-wall transition experimentally in the past. Goeckner *et al.* [20] were probably the first who found the Bohm criterion fulfilled in a multi-dipole filament discharge (although they did not point this out explicitly). Recently, several others followed [57, 48, 71, 11, 39] using the same type of device, partly with an interest in investigating a plasma composed of different ion species.
One should note, however, that the plasmas created in such multi-dipole discharges are remarkably different from the edge plasmas in fusion devices. In particular the density is three to four orders of magnitude smaller (cf. Fig. 1.1). Furthermore, strongly non-Maxwellian electron distributions were found in those plasmas [57, 11]. The only work carried out at higher plasma densities ($n_e = 10^{18}$ m^{-3}) by Gulick *et al.* [23] finds a velocity of only half the speed of sound in a distance of 5 mm to the surface[1]. As the authors did not believe in a 'sudden acceleration' over these last 5 mm they inferred that the Bohm criterion was violated.

[1] Actually this result is also confirmed by Albrecht Stark, who, in his PhD thesis [63] found a streaming velocity of about half the speed of sound in 10 mm distance to the target.

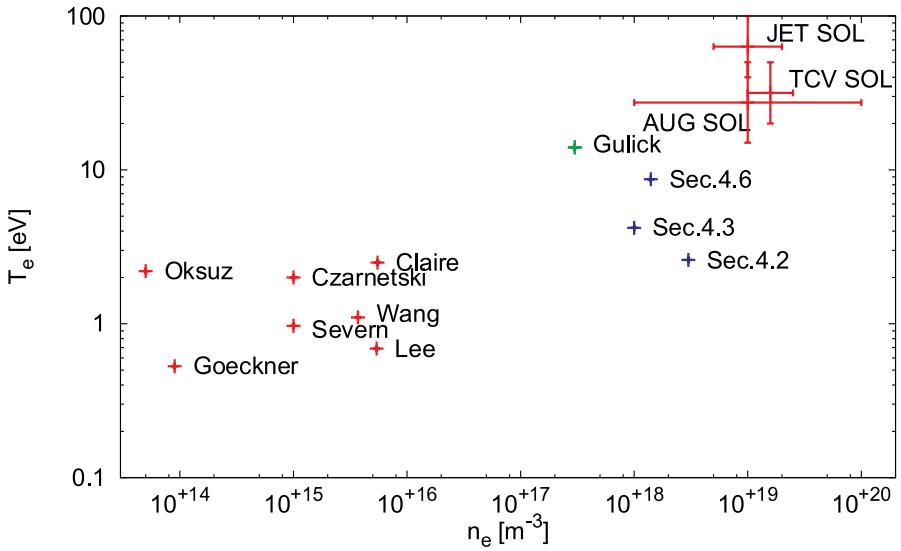

Figure 1.1: Electron density n_e and temperature T_e prevailing in the cited experiments. For low densities and temperatures the plasma wall transition was studied by several authors [20, 57, 48, 71, 11, 39] (small red crosses). The plasma conditions investigated in this thesis (Sections 4.2, 4.3 and 4.6, blue crosses) are much closer to those in a fusion device. Here the parameters in the scrape off layer (SOL) in Asdex Upgrade, JET and TCV [72] (large red crosses) are shown. The only authors who studied similar conditions were Gulick *et al.* [23] (green cross). They imply from their findings that the Bohm criterion is violated.

In the linear plasma generator PSI-2, plasma densities are also in the range $n_e = 10^{18}$ m^{-3}. Measurements performed by Fussmann [18] *et al.* in 2002 and within the framework of my master thesis [42, 44] in 2003 also revealed subsonic streaming velocities in front of the target. Due to the particular magnetic field configuration the streaming velocity was expected to be clearly supersonic there, provided that the Bohm criterion is fulfilled. This raises the question of whether the Bohm criterion might be violated at high densities. Since the density (or the pressure) drives plasma instabilities in many other situations the high density might in fact be the reason for such an effect.
For my master thesis, I performed measurements with Laser Induced Fluorescence (LIF). Since it is completely non-invasive, this diagnostics constitutes the ideal technique to investigate the plasma-wall transition. Due to the type of laser used[2], however, the spatial resolution was limited to about 50

[2]In [42, 44] a pulsed Nd:YAG laser (pulse length 10 ns) pumping a tunable OPO-OPA

mm. The principle goal of this PhD thesis is to investigate the plasma-wall transition at a substantially enhanced spatial resolution.
Whether the Bohm criterion is fulfilled or not is not the only important question when studying plasmas in contact with a solid obstacle. It is also important to understand which forces accelerate the ions and on which spatial scale this acceleration takes place. What is the influence of the target size? Does it make a difference whether the whole plasma is in contact with the target or the obstacle constitutes only a small perturbation? Is there a material dependence? How does the situation change if the incidence angle of the magnetic field lines on the target plate is non-normal? Do non-Maxwellian velocity distributions affect the situation?
The plasma-wall transition in general, as well as the particular questions addressed above, were treated from a theoretical point of view in a large number of articles. Riemann gives a good overview and refers to many articles related to the topic in [54]. Experimental works, however, are far more rare. This is one reason why this PhD thesis is focused on the experiment.
Apart from the measurements with LIF a different approach to measure the streaming velocity at the sheath edge was pursued. A combined current-force probe was used to simultaneously measure particle and momentum fluxes. As the particle flux is proportional to $nu_i|_{se}$ and the momentum flux proportional to $nu_i^2|_{se}$, the streaming velocity at the sheath edge $u_i|_{se}$ can be obtained from the ratio of the two. As explained in more detail in Sec. 4.7 the investigation of this special probe was also motivated by the possibility of measuring the ion temperature.

This PhD thesis is structured as follows: Chapter 2 starts with an introduction to the PSI-2 facility, where all the experiments were carried out. As many technical details were described in former PhD theses [33, 31, 47, 36], this section is kept rather short. The arrangement and the working principle of the LIF diagnostics are then explained. Design and calibration of the current-force probe are also addressed.
In Chapter 3 a simple collisional-radiative model of the Ar^+ ion is set up. Important questions like the time scales involved in populating/depopulating the levels and the interaction with the laser radiation are addressed. Finally an estimation of the different line broadening mechanisms is given there.
The main results of this thesis are then presented in Chapter 4. It starts with a short derivation of the basic equations needed for the modeling and introduces some relations used later. The reader familiar with the physics of plasma-wall interaction might skip this first section. Since the aim of this

system with high power ($P = 1$ MW), but low repetition rate ($R = 10$ Hz) was used.

thesis is to compare the models to the experimental data, these are presented close together in the rest of the chapter. The questions mentioned above are also discussed there.
Finally, the results are summarized and discussed in Chapter 5. The chapter closes with an outlook (Sec. 5.1) and a proposal for further improvements.
Appendix B refers to those investigators that aim to set-up a LIF diagnostics. Some useful hints are given there regarding how to adjust and operate such an arrangement.

Chapter 2

The Experiment

2.1 The PSI-2 facility

Fig. (2.1) shows the schematic arrangement of plasma generator PSI-2 with the LIF-diagnostic installed. In PSI-2, magnetized plasmas with direct wall contact, similar to those in a divertor of a fusion device, can be studied. In contrast to a fusion device, however, PSI-2 constitutes a linear arrangement so that the magnetic topology is much more simple. In particular for the experiments presented in this PhD thesis, which required stable plasma conditions over many hours, another important advantage of PSI-2 is that it can be operated stationarily. In addition accessibility and flexibility are much higher than in a fusion device.
The PSI-2 plasma generator is thus very suitable for the study of all kind of basic plasma physical phenomena, like turbulence and transport [69, 70, 2], waves [32, 31], as well as the sheath and presheath physics ([44], Chapter 4). It supports also the development and testing of diagnostics, for example electrical probes [34, 35, 67, 43], passive and active spectroscopy (Sec. 3), mass spectrometry [2, 68], Thomson scattering or atomic Helium beam diagnostics [36]. Furthermore, studies on fusion relevant materials [5, 6, 4, 38, 37, 17] are carried out in PSI-2.
Besides hydrogen, noble gases are also used as working gases, in particular here argon. Between the heated ($T \approx 1700°\mathrm{C}$) cathode made from lanthanum-hexaboride and the molybdenum anode a stationary high current ($I_D \approx 200$ A) arc discharge, fed by the gas from a gas inlet ($\Phi_n = 100$ sccm), is sustained. The plasma is heated ohmically in this region. Confined by the axial magnetic field ($|\vec{B}| \approx 100$ mT) and driven by the pressure gradient it streams through the pumping stage (where large amounts of the neutral gas are removed) and the target chamber (the region, where most of the experi-

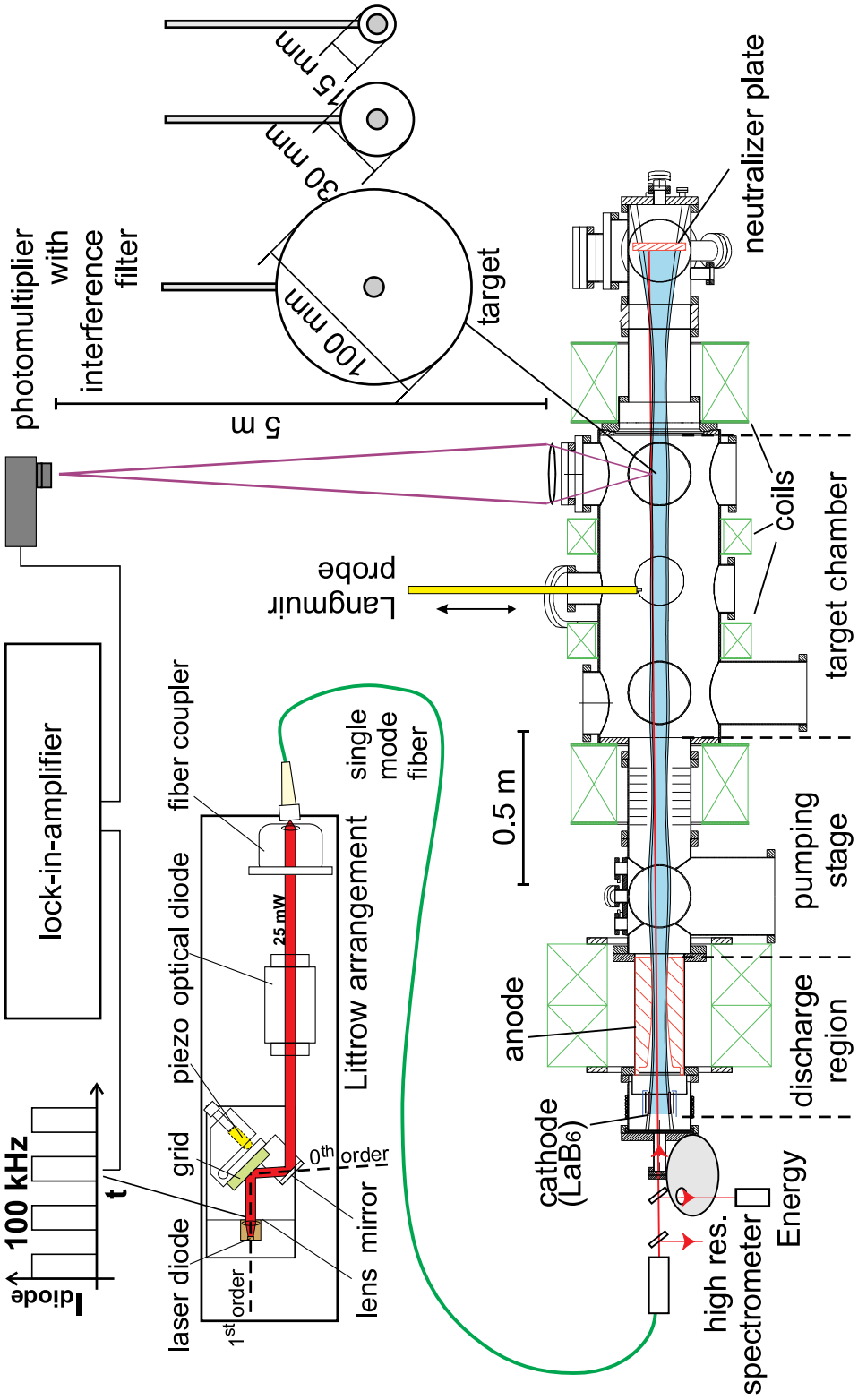

Figure 2.1: Plasma generator PSI-2 and the LIF diagnostic system

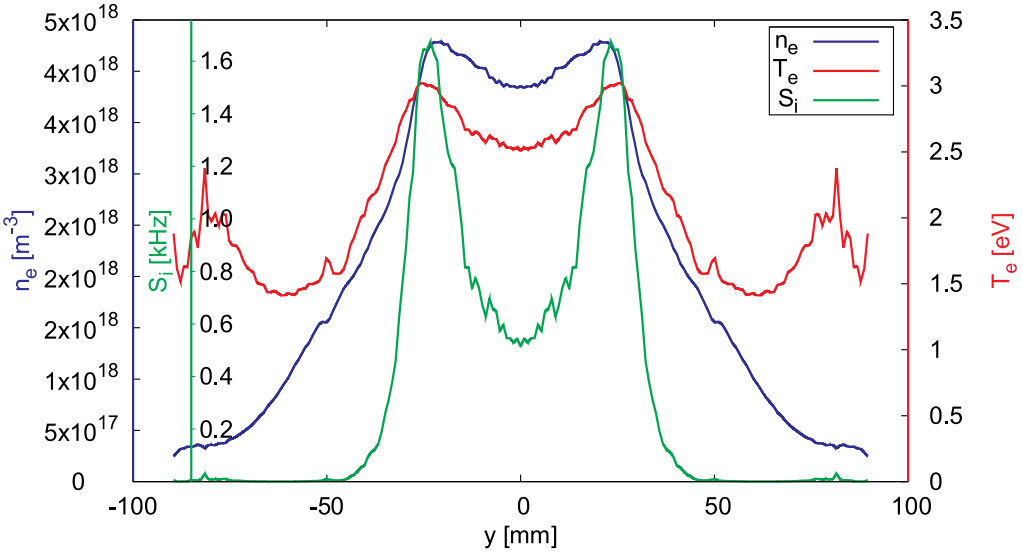

Figure 2.2: Radial profile of electron density n_e and temperature T_e and of the ionization rate coefficient S_i

ments are carried out) towards the neutralizer plate at the end of the device. A great portion of the primary plasma is lost at the hollow anode, but the fraction that leaves this region is amplified due to ionization in a thin cylindrical zone extending over the whole remaining part of the discharge. Due to the shape of cathode and anode the plasma is primarily maintained within a hollow column about 10 cm in diameter. The radial profile of electron density n_e and temperature T_e, shown in Fig. (2.2), is measured by means of a Langmuir probe positioned in the center of the target chamber. The ionization profile S, computed from the local n_e and T_e values and from the rate coefficient for ionization Eq. 3.4 is also shown in the figure. As both, T_e and n_e, are peaked at a radial position of $r = 25$ mm, ionization takes place primarily in a region between $r_1 = 15$ mm and $r_2 = 30$ mm. A finite plasma density outside this source region can only be maintained by means of cross field diffusion.

Further technical details of PSI-2 have been described extensively in several doctoral theses in the past and can be found in [31, 47, 33, 36]. In [31] a list of typical frequencies, lengths, velocities and transport coefficients is given. The computation of the magnetic field, the discharge characteristics, and several diagnostics are also described there. Details about the electric wiring and the gas balance of the plasma generator are addressed in [47]. Before 1998 the plasma generator was operated with two magnetic coils less, a shorter vacuum chamber and a copper anode. At that time it was named

PSI-1. Although many features of the experiment remained the same the reader may refer to [33], which was carried out after these changes.
As we will need to determine orientation and strength of the magnetic field at an arbitrary point in space in Sec. 2.3.1 and Sec. 3.5, here we want to recall how to compute the magnetic field. The magnetic field strength $\vec{B}(\vec{r}')$ at an arbitrary point $\vec{r}'$ in space can be computed involving the Biot-Savart law

$$\vec{B}(\vec{r}) = \sum_{i=1}^{6} \int \frac{\mu_0}{4\pi} \frac{\vec{j}_i \times (\vec{r} - \vec{r}')}{|\vec{r} - \vec{r}'|^3} d^3 r_i' \ . \tag{2.1}$$

A reasonable approximation (error $< 5\%$ on the axis) for many applications is to assume the current densities in the coils to be given by

$$\vec{j}_i(r, \phi, z) = \vec{e_\phi} \frac{N_i I_i}{A_{c,i}} \delta\left(z - z_{mean,i}\right) \delta\left(r - R_{mean,i}\right) \ , \tag{2.2}$$

where $z_{mean,i} = 0.5(z_{min,i} + z_{max,i})$, $R_{mean,i} = 0.3R_{min,i} + 0.7R_{max,i}$ and $A_{c,i} = (z_{max,i} - z_{min,i})(R_{max,i} - R_{min,i})$. The integrations in Eq. 2.1 then become trivial. For a more accurate computation of the fields the reader is referred to [31, 33]. As shown there the field at the axis ($r = 0$) can be solved analytically

$$B(0,z) = \frac{\mu_0}{2} \vec{e}_z \sum_{i=1}^{6} j_i \left[(z - z_{max,i}) \ln \left(\frac{R_{min,i} + \sqrt{R_{min,i}^2 + (z - z_{max,i})^2}}{R_{max,i} + \sqrt{R_{max,i}^2 + (z - z_{max,i})^2}} \right) - (z - z_{min,i}) \ln \left(\frac{R_{min,i} + \sqrt{R_{min,i}^2 + (z - z_{min,i})^2}}{R_{max,i} + \sqrt{R_{max,i}^2 + (z - z_{min,i})^2}} \right) \right] . \tag{2.3}$$

which is a good approximation for the magnetic field in the whole plasma region ($0 \leq r \leq 5\,\mathrm{cm}$). With the coil data and the currents for the standard magnetic field given in Tab. 2.1 we can then compute the field. During the measurements presented in Chapter 4 the last coil was shifted by about 6 cm with respect to the nominal position. As shown in Fig. 2.3 we must take into account this circumstance.
Since the magnetic pressure $p_B = B^2/(2\mu_0)$ is about three orders of magnitude higher than the (kinetic) plasma pressure $p = n(T_e + T_i)$, *i.e.* since the plasma beta $\beta = p/p_B$ is small, the diamagnetism of the plasma can be neglected (cf. [33]).

Coil	1	2	3	4	5	6
R_{min} [m]	0.178	0.178	0.140	0.230	0.230	0.140
R_{max} [m]	0.322	0.322	0.288	0.295	0.295	0.288
$N^{(j)}$	600	600	335	81	81	335
$I^{(j)}$ [A]	90	30	310	300	300	310
nominal						
z_{min} [m]	0.098	0.306	0.848	1.388	1.735	2.167
z_{max} [m]	0.289	0.498	1.094	1.498	1.845	2.413
real						
z_{min} [m]	0.129	0.337	0.848	1.420	1.754	2.241
z_{max} [m]	0.320	0.527	1.105	1.537	1.871	2.498

Table 2.1: Geometry and standard currents of the magnetic coils. Coils 4 and 5 are connected in series.

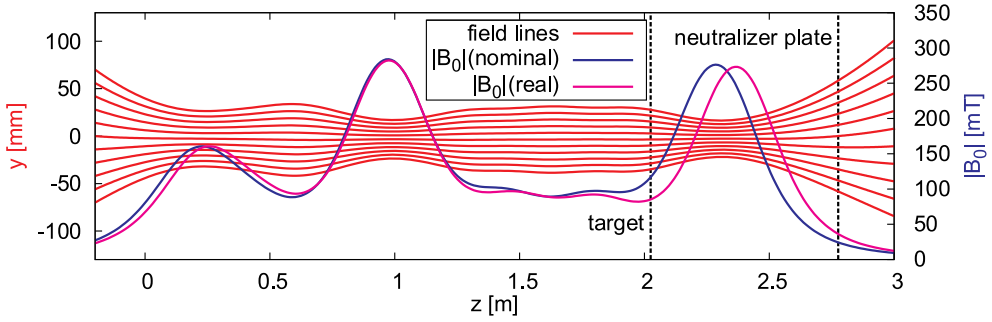

Figure 2.3: Field lines and axial field strength in PSI-2.

2.2 Laser induced fluorescence diagnostics

Laser Induced Fluorescence (LIF) is a very powerful tool to investigate the kinetics of a plasma or of any other fluid medium. Here it is applied to argon, exciting the ions in the metastable level $3d\ ^4F_{9/2}$to the $4p\ ^4D_{7/2}$level (at $\lambda_0 = 664.3698$ nm) and causing fluorescence due to the subsequent spontaneous decay to $4s\ ^4P_{5/2}$ at 435 nm. We will also refer to these levels as the 'metastable' $|m\rangle$, the 'excited' $|e\rangle$ and the 'final' $|f\rangle$ LIF states. The momenta of the photons involved are orders of magnitude smaller than that of the ion, so that we can say that this diagnostics is non-invasive. As the band width of the laser radiation is much smaller than the Doppler width of the transition, only those ions are excited that are in the velocity interval $v_z \ldots v_z + \Delta v_z$, where $v_z = c(\lambda_0 - \lambda_L)/\lambda_0$ is the velocity component corresponding to the Doppler shift $\lambda_L - \lambda_0$. Scanning the laser wavelength λ_L

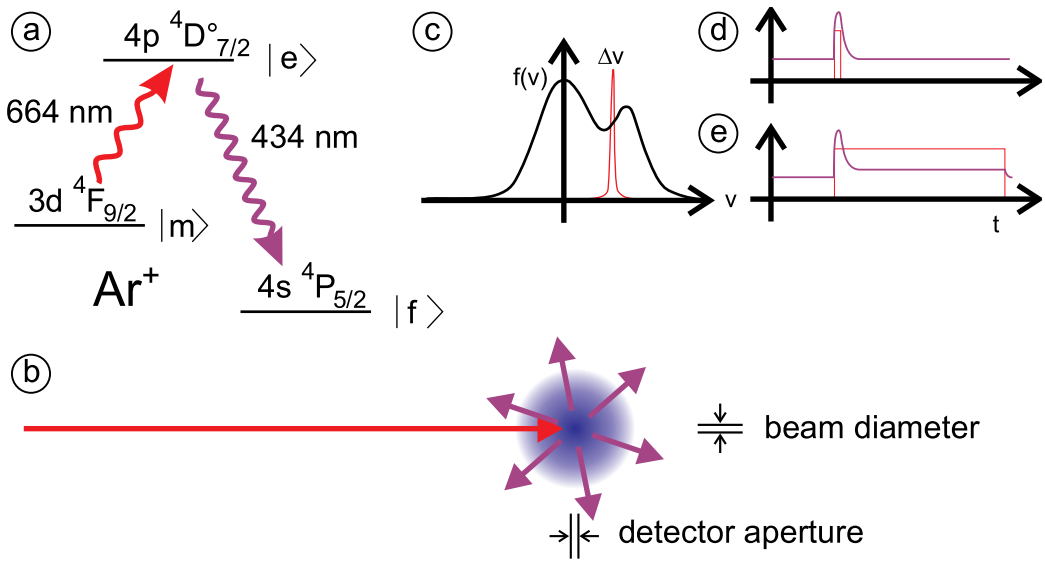

Figure 2.4: Illustration of the laser induced fluorescence (LIF) working principle. a) LIF is a non-invasive diagnostics. The argon ion is excited from a metastable level $|m\rangle$ to the $|e\rangle$ state. The spontaneous transmission to $|f\rangle$ causes fluorescence. b) A high spatial resolution is achieved by detecting the fluorescence under 90°. The measuring volume is given by the intersection of the detection and excitation volumes, which is limited in all three spatial directions. c) Since the small band width laser excites only those ions that are in the small velocity interval Δv_z, the velocity distribution can be measured at a high resolution in velocity space. d) The fluorescence follows the laser radiation instantaneously ($\tau = 10$ ns) so that a high temporal resolution can be achieved in general (short laser pulses required). e) However, due to the small signal-to-background ratio a modulated CW laser is applied, measuring a single value point of the velocity distribution during about $\Delta t = 30$ s.

while detecting the fluorescence enables us to measure the ion velocity distribution (ivdf) $f(v_z)$ in the direction of the laser beam.
The detection optics observes the laser beam under 90° so that the volume where the ivdf is measured is limited in three spatial directions, in two directions by the laser beam and in the third by the detector's aperture. We can therefore say that LIF provides a high spatial resolution, one of the goals of this thesis. We address the detection volume in a more detailed way in Sec. 2.2.2.
In principle it is also possible to achieve a high temporal resolution, the atomic transitions taking place on a temporal scale of some tens of nanoseconds. As we will see, however, in Sec. 2.2.3 the number of photons that are

produced by LIF is very small in comparison to those that are emitted by the plasma itself such that in practice, due to the bad photon statistics, it is impossible to achieve a high temporal, spatial and a high resolution in velocity space at the same time. If a temporally periodic process is studied, however, a good photon statistic can be obtained by integrating over many cycles. A. Stark applied such a technique in his PhD thesis to study kinetic Alfén waves by means of LIF[63].

2.2.1 Laser

Fig. 2.1 shows a schematic of the grating stabilized tunable diode laser (manufacturer TOPTICA, model DL 100) which constitutes a so called Littrow arrangement. The radiation originates from the electrons in the semi-conductor material of the laser diode when they recombine with holes during the transition from a n-doped to a p-doped region. The total laser power is proportional to the number of these recombination processes and therefore is strongly dependent on the diode current. In order to ensure a stable temperature, a requirement for an operation at a stable wavelength, the whole laser head is mounted on a Peltier cooler/heater regulated by a PID-temperature controller. The temperature is measured by means of a thermocouple. A general introduction to diode lasers is also given in [14].

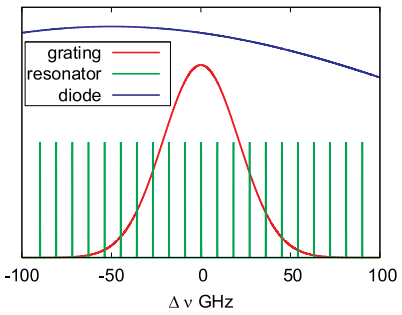

Figure 2.5: Modes of the diode laser.

The light at a wavelength of $\lambda = 664$ nm, collimated with an aspheric lens, impinges on an optical grating with $1/a$ =2000 grooves per mm at a distance of about $L = 15$ mm under an angle of about α =41°. According to the diffraction grating equation

$$m\lambda = a(\sin\alpha + \sin\beta) \tag{2.4}$$

the first order ($m = 1$) of the impinging light is reflected back ($\beta = \alpha$) to the laser diode. While the back side of the diode is highly reflective, the front side is coated by an anti-reflex layer. Diode and grating thus constitute an 'external' resonator (in contrast to an 'internal' resonator which is formed when both interface layers of the diode are highly reflective) whose free spectral range is $\Delta\nu = c/(2L) = 9$ GHz. In order to tune the laser the grating

is tilted slightly. The tilt shifts the spectral maximum of the grating and, simultaneously, the length of the resonator. Fig. 2.5 illustrates the situation: The amplification curve (blue) of the laser diode is very broad (FWHM $\approx$ 5000 GHz). For the given wavelength the reflectivity of the grating is shown by the red curve (FWHM $\approx$ 50 GHz). The resonator modes (green spikes) have a very narrow band width of around 10 MHz. The mode with the highest amplification (the convolution of the three curves) is the only one that survives. Due to the small free spectral range of 9 GHz it is obvious that the simultaneous detuning of the resonator and the grating has to be very accurate otherwise mode hoping may occur during a wavelength scan. The mode hop free spectral scan range of the present laser was specified by the manufacturer to be about $\nu = 15$ GHz or $\Delta\lambda = 22$ pm.
The zeroth order of diffraction is coupled out of the resonator and is guided via a mirror, an optical diode, and a fiber coupler to an optical single mode fiber. The optical diode prevents radiation from being reflected back into the laser diode as this could influence the wavelength or even cause damage to the laser.
The power of the radiation at the fiber coupler is about 25 mW. Due to its small diameter (about 3 μm) it is only possible to couple about 8 mW into the fiber. In order to avoid this high loss of power some of the measurements were carried out without the fiber (Fig. 4.6(a) and Fig. 4.18). However, in these cases the beam quality worsens. The extension of the rectangular laser spot in vertical direction is about 10 mm while in horizontal direction it is between 1 and 2 mm. We will see in the following section, that the extension of the detection volume is larger in horizontal direction and so the laser was guided to the plasma via two mirrors, which rotates the beam by 90°. The use of mirrors is also beneficial for a simple adjustability.

2.2.2 Detection

Fig. 2.6 shows the optical system for the LIF-detection. In order to collect as much light as possible a large space angle must be covered by the lens, *i.e.* a large lens must be arranged as close as possible to the plasma. As a sharp image is accomplished only if the object distance is longer than the focal length, a large lens with a short focal length is required. This is a condition that is difficult to fulfill, since the experiment also demands a small aberration. First attempts to find the LIF signal with a single lens ($\varnothing = 10$ cm and $f = 16$ cm) failed since the image quality was poor. A significant improvement was achieved by applying two aberration corrected lenses (APO Tessar 9:900, manufacturer Carl Zeiss, Jena) with a focal length of 900 mm and

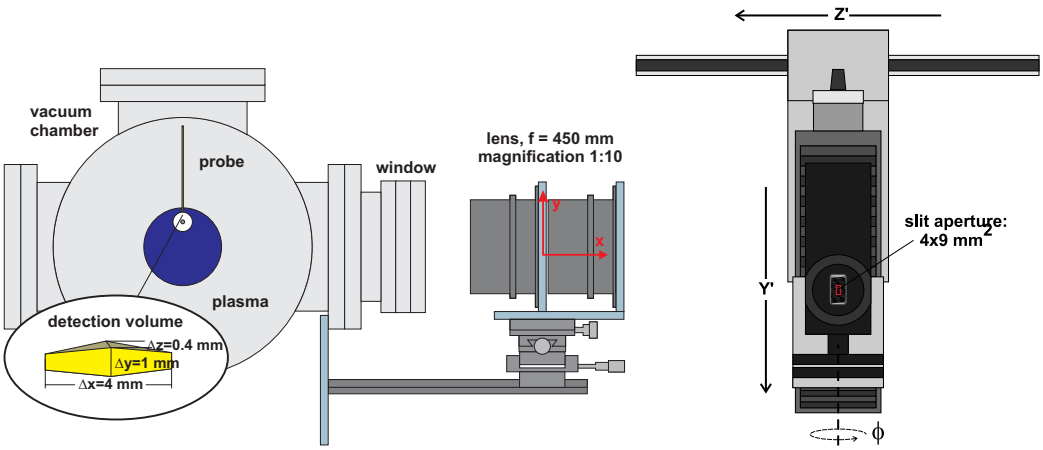

Figure 2.6: Left: lenses mapping the detection volume to the detector. Right: photomultiplier mounted on a manipulator

a diameter of $2r_l = 10$ cm. These may be regarded as a single aberration-corrected lens with a focal length of $f = 450$ mm. As the distance to the image (avoiding the use of mirrors) is limited to $d_i = 5$ m by the laboratory extensions, the lens was placed at a distance of $d_o = (1/f - 1/d_i)^{-1} = 49.5$ cm to the detection volume. The magnification was then $S_i/S_o = d_i/d_o = 10.1$.
A photomultiplier (manufacturer Hamamatsu, model 1P28) combined with a narrow band-width interference filter is located in the image plane (where the coordinates are labeled with a prime) as shown in Fig. 2.6, right. The photomultiplier is mounted on a manipulator movable in z' and y' directions. As the maximum transition of the interference filter is very sensitive to the incidence angle of the light, it is necessary to adapt the turning angle ϕ' during a z' scan. This is done by a third manipulator. In front of the filter an adjustable slit is mounted. This is used to adapt the detection volume to the excitation volume.
The high magnification of the optical system benefits the goal of measuring the LIF-signal with a high spatial resolution. When the detector is moved on a coarse scale, the detection volume moves ten times less within the plasma. At the same time the light is almost parallel when it reaches the interference filter so the losses due to the angular distribution of the light are minimal. The manufacturer (LOT) specifies a wavelength shift of 1.3 nm when the filter is tilted by 6°. Its full width at half of maximum is 1.5 nm, the wavelength of maximum transition (about 45%) being located at 435 nm. The

angular dependent transmission can then be given by

$$T(\alpha) = 45\% \exp\left(-4 \ln 2 \left(\frac{\alpha}{6^\circ} \frac{1.3 \text{ nm}}{1.5 \text{ nm}}\right)^2\right) \ . \tag{2.5}$$

So, for example, if the filter was placed in a distance of 50 cm from the lens (where the magnification would be about 1:1) the average transmission of the filter would be reduced to approximately

$$\frac{1}{\pi r_L^2} \int_0^{r_l} T(\arctan(r/50\text{cm})) 2\pi r dr = 20\% \ , \tag{2.6}$$

i.e. less than half of the transmission at normal incidence.
The magnifying optical system has another feature that shall be discussed in the following, a small depth of field: Let the coordinate origin be located in the center of the lens, as indicated in Fig. 2.6, with the z-axis pointing towards the neutralizer plate[1]. A point (x,y,z) is then mapped to a point (x',y',z') according to

$$x' = \left(\frac{1}{f} - \frac{1}{-x}\right)^{-1} \qquad y' = y\frac{x'}{x} \qquad z' = z\frac{x'}{x} \ . \tag{2.7}$$

If x' lies ahead or behind the plane where the detector is placed (at a distance d_i), the light originating from (x,y,z) is not mapped as a point, but becomes a circular spot with the diameter

$$r' = \left| r_l \left(1 - \frac{d_i}{x'}\right) \right| \ . \tag{2.8}$$

The slit aperture for most of the measurements is $A_{y'} = 9$ mm and $A_{z'} = 4$ mm. For the moment let the aperture of the slit be located at (x',y',z')=(d_i,0,0). From a volume defined by the points (x,y,z) where $|z'| + |r'| \leq A_{z'}/2$ and $|y'| + |r'| \leq A_{y'}/2$ all photons that are emitted towards the lens reach the detector (for the moment neglecting the finite transmission of the optical components itself). This volume which we also refer to in the following as the detection volume V_d has a rectangular cross-section in the y-z-plane, a rhombic shape in the x-z-plane, and the shape of a trimmed rhombus in the x-y-plane (cf. Fig. 2.6 and Fig. 2.7 red bordered area). The extensions of the volume

$$\Delta x = \frac{d_i A_{z'}}{r_l \left(\frac{d_i}{f} - 1\right)^2 - \frac{A_z^2}{4 r_l}} \ , \ \Delta y = A_{y'} \frac{d_o}{d_i} \ , \ \Delta z = A_{z'} \frac{d_o}{d_i} \tag{2.9}$$

[1]Note that in order to provide a right handed coordinate system the x-coordinate of the detection volume is negative.

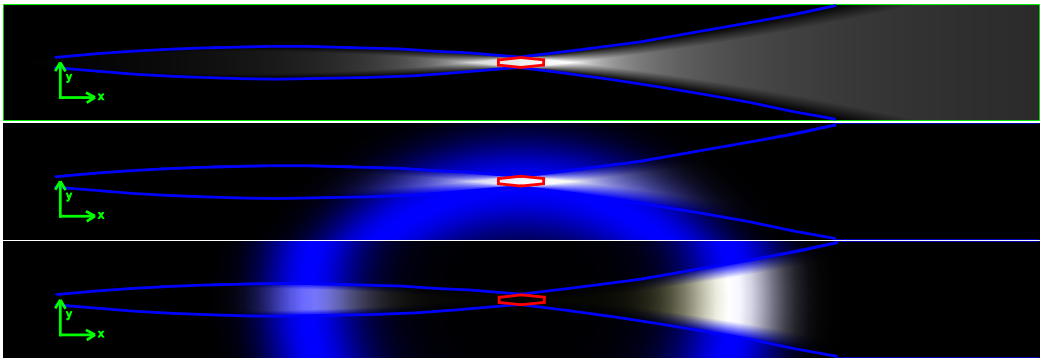

Figure 2.7: Light collection by the optical system. The red areas indicate the detection volume *i.e.* the region where all photons emitted in the space angle defined by the lens reach the detector. Photons that originate from the region beyond the blue lines are not able to hit the detector. The percentage of photons that reach the detector for all other regions is indicated by the brightness of the pixel. Top: the emission of photons is assumed to be homogeneous. Middle: the detection volume is situated in the region of maximum density and temperature. Bottom: the detection region is placed in the central region of the plasma column. Most of the photons then originate from the region outside the detection volume

are $\Delta x = 3.2$ mm, $\Delta y = 0.9$ mm,$\Delta z = 0.4$ mm. It is then easy to verify that the volume V_d is in good approximation

$$V_d \approx \Delta x \Delta y \Delta z \left(\frac{1}{2} - \frac{1}{6} \frac{A_{z'}}{A_{y'}} \right) \ . \tag{2.10}$$

On the other hand, photons emitted from points (x,y,z) with $|z'|-|r'| > A_{z'}/2$ and $|y'| - |r'| > A_{y'}/2$ (areas beyond the blue lines in Fig. 2.7) are not able to reach the detector at all. For all other regions the ratio of the number of photons N_D that reach the detector to the total number of emitted photons N is determined by comparing the intersection $A_{\circ\cap\square}$ of the light spot $A_\circ = \pi r'^2$ and the aperture of the slit $A_\square = A'_y \times A'_z$:

$$I(x,y,z) := \frac{\Omega}{4\pi} N_D/N = A_{\circ\cap\square}/A_\circ \ , \tag{2.11}$$

where $\Omega = \frac{\pi r_l^2}{x^2}$. Fig. 2.7 (top) shows $I(x,y,z)$ averaged over a z-interval of 20 mm, the contribution of the different volumes to the total amount of photons received by the detector. Regions from which a high fraction of photons reach the detector are marked brightly. It is then possible to

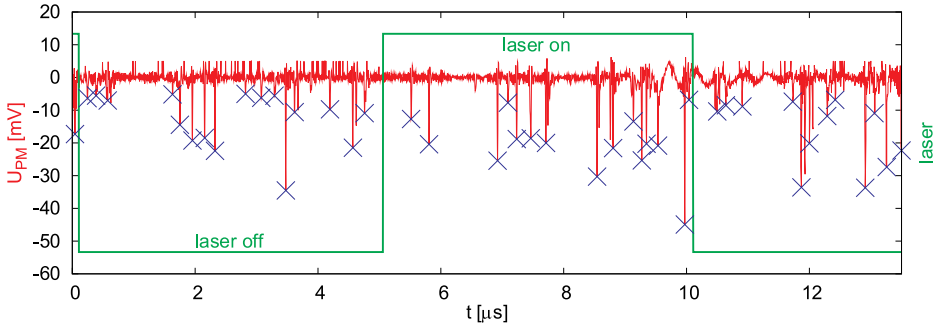

Figure 2.8: Signal of the photomultiplier determined with 50 Ω. The blue crosses are the counted peaks.

quantitatively compute the ratio of photons that originate from the detection volume to the total number of photos that reach the detector:

$$S = \int_{V_D} I(x,y,z) / \int_V I(x,y,z) = \frac{\Omega}{4\pi} \times 4.3\% \ . \tag{2.12}$$

In other words, only a 20^{th} of all the photons received by the detector originate from the detection volume, when assuming a constant emission density. However, since the plasma has a pronounced hollow profile (cf. Fig. 2.2) the assumption of a constant emission profile is not justified. Emission profiles of the plasma were computed in Sec. 3.1 and are superposed with the detection profile. Here it becomes clear how important it is to place the detection volume in a region of high emissivity: Evaluating S with the detection at $y = 20$ mm gives a value of almost $S4\pi/\Omega = 20\%$, while in the case where the detecion volume is in the center of the plasma column $S4\pi/\Omega = 0.15\%$. Note that this high contribution of (constant) false light to the background signal does *not* affect the spatial resolution, which is given by the intersection of excitation and detection volume.

2.2.3 Lock-in-technique

The greatest challenge for applying laser induced fluorescence is to find the signal within the orders of magnitude higher background. This background is so high for two reasons: firstly, as was shown in Sec. 3.1 the $4p^4D_{7/2}$ level is not only populated due to the influence of the laser radiation, but also by the permanent electron collisions inside the plasma. Secondly, in the previous paragraph we saw that the photons are not only collected from the excitation volume but also from other extended regions in the plasma.

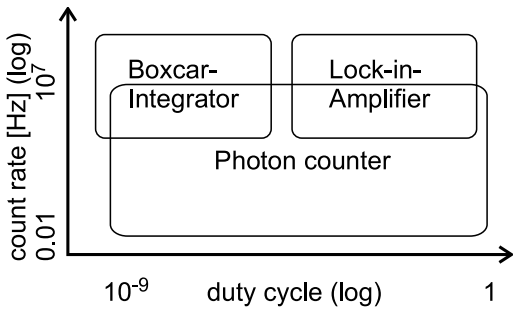

Figure 2.9: Favorable conditions for the application of different signal recovery techniques.

The general approach for detecting fluorescence photons is to compare the emission signal from the plasma when the laser is turned on and off. Besides the possibility of permanently recording the signal from the photomultiplier there are three other techniques of signal recovery: (1) Boxcar integration, (2) photon counting and (3) the lock-in-technique. Boxcar integrators are optimized for short duty cycles, *i.e.* when the pulse lengths of the laser are short. Photons can only be counted if the probability is low that two photons hit the multiplier during a time interval that is short compared to the characteristic duration of an electron cascade in the photomultiplier (typically $\tau_{cas} = 10$ ns). For this reason photon counters can only be applied for counting rates lower than about $\nu = 10$ MHz. Lock-in-amplifiers are the most appropriate devices when the on-and-off periods of the modulated signal are equally long (cf. Fig. 2.9) even if the counting rates are greater than 10 MHz. This is why lock-in-technique was applied.
Besides the input signal U_{in} these devices also require a reference signal U_{ref} from a signal generator which modulates the source (in our case the laser). The output signal of the LIA is (proportional to)

$$U_{outX}(t) = \frac{1}{\tau}\int_{t-\tau}^{t} \sin(\omega_{ref}t' + \phi_{ref})U_{in}(t')dt' \ , \tag{2.13}$$

where τ is a time constant, which can be chosen according to the application. ω_{ref} and ϕ_{ref} are (angular) frequency and phase of the modulation signal. All components of the input signal with a non-constant frequency *and* phase relation to this modulation signal have a vanishing contribution to the integral and are thus suppressed. This makes a LIA much more efficient than for example a band pass amplifier (which is only sensitive to the frequency). Fig. 2.10[2] shows a simplified functional block diagram of the lock-in-amplifier

[2]Both figures 2.9 and 2.10 originate from the documentation provided by the manufacturer (Stanford Research).

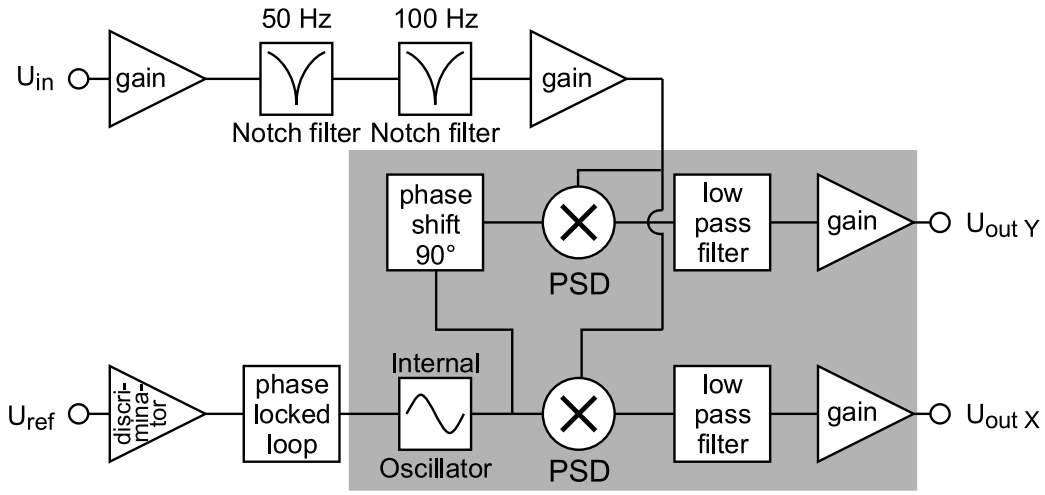

Figure 2.10: Simplified block diagram of the lock-in-amplifier (LIA) SR 850 DSP, Standford research. The signals in the gray area are processed digitally.

used (SR 850 DSP, Stanford Research). After preprocessing the signals in a pre-amplifier stage the signals are digitized and processed by the the phase sensitive detector (PSD), which is the main component of the device. A second channel U_{outY} computes the same integral as Eq. 2.13 but with ϕ_{ref} shifted by 90°. However, as the time delay between the absorption and the fluorescence of the argon ion is orders of magnitude smaller than the modulation period, U_{outY} is practically 0. As an initial test of the device it was verified that signals attenuated to a few nanovolts can indeed be measured by the LIA as specified by the manufacturer.
Fig. 2.8 shows the signal from the photomultiplier, when the wavelength is in resonance and the arrangement is aligned well. During the period of about 14 μs, 45 photons were counted, the mean photon impact frequency is thus 3.3 MHz. Averaging the signal and dividing by the value of the terminating resistor $R = 50\ \Omega$, the mean current is $I_{PM} = -18.5\ \mu$A. Each primary electron produced is therefore multiplied by a factor

$$f = \frac{-I_{PM}}{\nu e} = 3.5 \times 10^7\ , \tag{2.14}$$

which is approximately the value specified by the manufacturer ($f = 10^7$). The same signal was measured by the lock-in-amplifier, which indicated an amplitude of about 10 μV. The corresponding current in the terminating resistor -0.5 μA=$-ef\nu_{LIF}$ then yields the frequency that fluorescence photons hit the detector:

$$\nu_{LIF} = 35\ \text{kHz}\ . \tag{2.15}$$

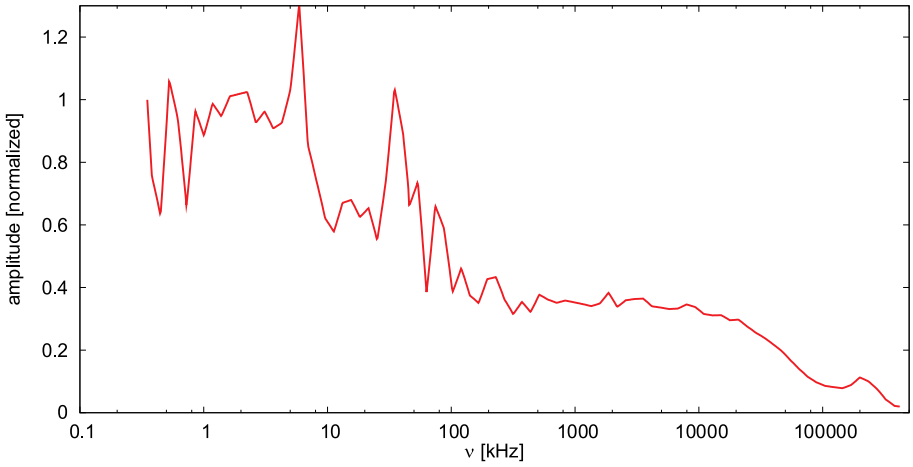

Figure 2.11: Frequency analysis of the photomultiplier signal when detecting the background light emission from a typical argon discharge. For frequencies above 100 kHz the noise level is much smaller than in the lower frequency range. For this reason it is preferable to modulate the laser at a high frequency (cf. also Fig. 2.12).

This means that only every 100^{th} photon is a LIF photon (and this means that to a high probability not even one photon in Fig. 2.8 is a LIF photon!). In order to measure a clear signal we have to demand that the number of LIF photons N_{LIF} stands out from the statistical fluctuations $\Delta N_{bg} = \sqrt{N_{bg}}$ of the number of background photons, even in the wings of the distribution function. The time required to measure a ratio $N_{LIF}/\Delta N_{bg} = 100$ is then

$$\frac{\nu_{bg}}{\nu_{LIF}^2} 100^2 = 30 \text{ s} \,, \tag{2.16}$$

which is the integration time typically used.
In practice, however, it is not only important to choose a long integration time but also to adapt the modulation frequency to the frequency spectrum of the signal. Fig. 2.11 shows a Fourier analysis of typical photomultiplier signals. The spectrum (and in particular the peaks at around 6 and 50 kHz) are not very well understood up to now, however, a clear decay of the amplitude is observed when exceeding frequencies around 100 kHz. This is why the fluctuations of the signal measured at the lock-in amplifier are much smaller when modulating the laser at 100 kHz rather than at 10 kHz (cf. Fig. 2.12).

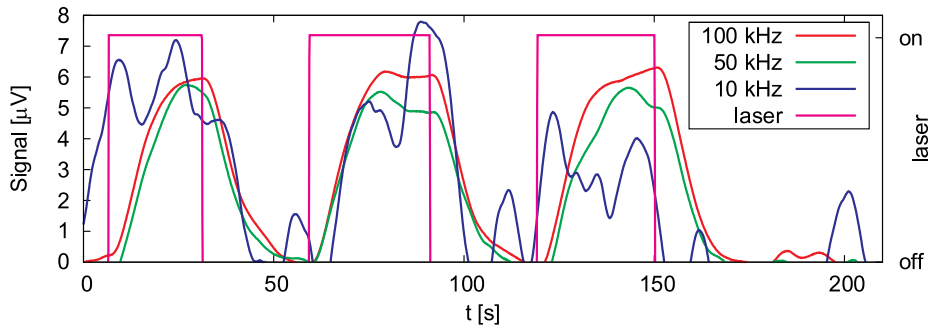

Figure 2.12: Signal of the lock-in-amplifier at different modulation frequencies when the laser is turned on and off.

2.2.4 Monitoring laser power and wavelength

In order to evaluate the LIF-signal quantitatively it is necessary to know the laser power and the wavelength accurately. For this reason a small fraction of the laser radiation was guided to an energy meter and to a high resolution spectrometer by means of two beam splitters before coupling the beam into the plasma chamber. Since the energy meter can only work properly when the impinging light is modulated, but the 100 kHz is too fast to be detected, the beam is chopped by a mechanical chopper wheel. A typical signal is shown in Fig. 2.13. As the energy meter has a high impedance ($\approx$ 1 MΩ), an impedance converter is connected at the output. Although the output voltage is reduced to 90% by the converter, there is no further attenuation by the long co-axial cables used. The sensitivity of the energy meter is specified as 970 V/J. With this information and with the reflectivity of the beam splitters of 8% (4% for each surface) the measured voltage can be converted into an energy E_{las} that is deposited on the energy meter per opening cycle $t_{open} \approx$ 6 ms of the chopper. The laser power is then $P_{las} = E_{las}/t_{open}$.
An important question to consider here is how the LIF-signal behaves with varying laser power. In order to investigate this the plasma conditions were kept constant and the signal was maximized by adjusting the wavelength. Then different gray filters were placed at the exit of the laser and the change of both the laser power and the LIF-signal was recorded. The relationship is mostly linear as seen in Fig. 2.14. This is why the signal was normalized to the laser power when the ion velocity distribution functions were evaluated in Chapter 4.
The laser wavelength was measured by means of a high resolution Fastie-

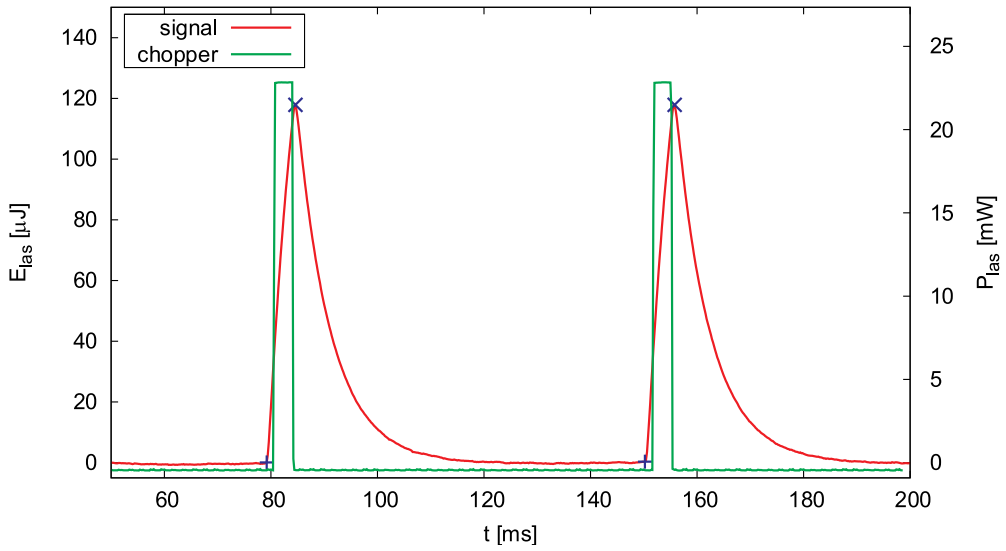

Figure 2.13: Measurement of the laser power. Immediately before coupling the laser into the plasma chamber a small fraction ($\approx$ 8 %) is guided to a pyro-electric power meter. This light is chopped by a mechanical chopper wheel (cf. also Fig. 2.1). The height of the peak is proportional to the laser energy E_{las} during one opening cycle t_{open} of the chopper. Dividing E_{las} by t_{open} yields the laser power P_{las}.

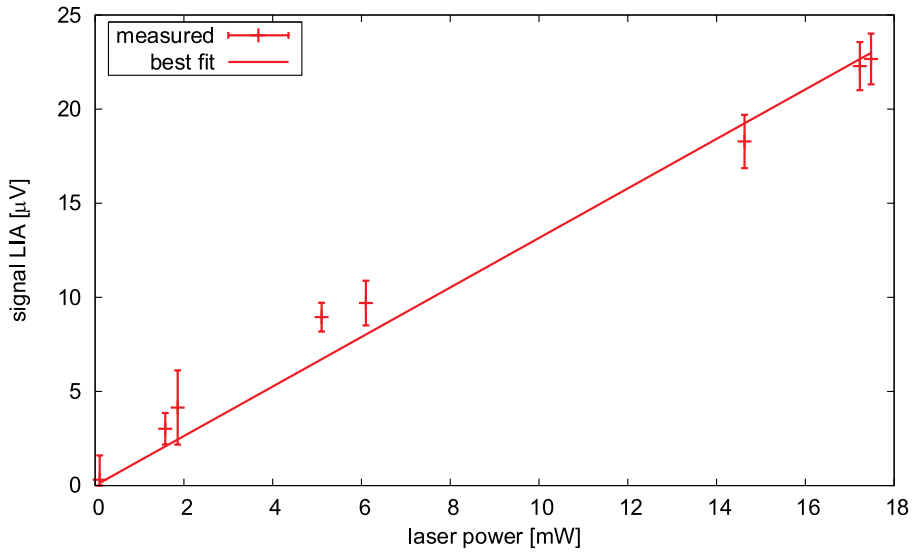

Figure 2.14: Linearity of the LIF-Signal with the laser power.

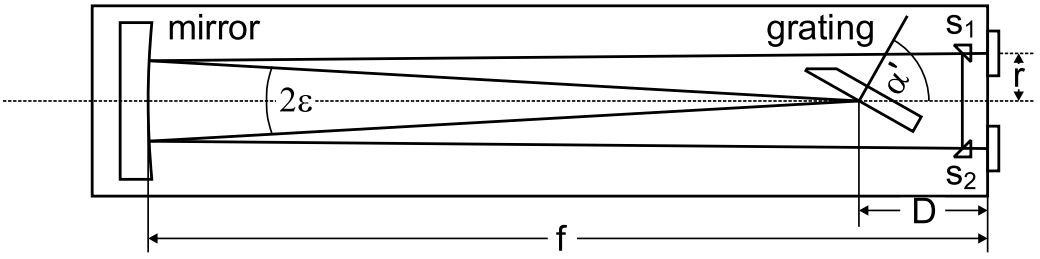

Figure 2.15: Arrangement of the Fastie-Ebert-spectrograph. $f = 1500$ mm, $D = 230$ mm, $r = 85$ mm and $\epsilon = 3.24°$ are specified by the manufacturer.

Ebert[3] spectrometer (manufacturer Sopra, model UHRS F1500DP). A schematic of the spectrometer is shown in Fig. 2.15. The high resolution is obtained due to the large size of the grating ($G_x = 220$ mm$\times G_y = 110$ mm) and the high order of diffraction. The double pass of the light, which is accomplished by means of the tilted mirrors s_1 and s_2, doubles the resolution again (this is possible since the mirrors are not on the same height as the entrance slit). The grating itself then requires only a relatively low number of rulings of $1/a = 316$ mm^{-1}. For the 8^{th} order of diffraction a theoretical resolution of

$$R \equiv \frac{\lambda}{\Delta\lambda} = mG_x\frac{1}{a}2 = 1.1 \times 10^6 \tag{2.17}$$

can be given, although this value was never achieved in practice. Unfortunately the piezo driven slit controller was not calibrated so that the absolute aperture was unknown. However, when the aperture of the slit was optimized (by closing the slit further the resolution decreases again due to diffraction effects) the narrowest spectral line measured in the red spectral range was 3.4 pm (cf. Fig. 2.17). This corresponds to a resolution of $\frac{\lambda}{\Delta\lambda} = 200{,}000$, *i.e.* a factor of 5 less[4]. If the width of this line is determined mainly by the finite slit aperture we can estimate an aperture width of about 200 μm. However, it is more likely than any other mechanism broadens the line.
For several reasons the angle between the incident and the diffracted light $|\alpha - \beta| = 2\epsilon$ is chosen to be small. Applying trigonometric sum relations

[3]Ebert spectrometers were applied historically before Czerny-Turner spectographs came in use and are in contrast to these equipped with only one concave mirror. Originally the Czerny-Turner constituted an improvement with respect to the Ebert spectrograph. However, since Fastie [16] proposed the use of curved entrance and exit slits in 1952 to avoid the apparatus' astigmatism the so called Fastie-Ebert spectrograph found new application.

[4]Note that the spectrometer was not operated at its maximum resolution; first because the slit was not closed as much as possible and second because fiber coupler at the entrance slit was not perfectly aligned.

Eq. 2.4 can be written as

$$m\lambda = 2a\sin(\alpha')\cos(\epsilon) \ , \tag{2.18}$$

where $\alpha' = \alpha - \epsilon$ is the tilt angle of the grating. When measuring the laser line ($\lambda_{las} = 664$ nm) in the 8^{th} order this angle is $\alpha' = 57.21°$. Besides the resolution, the angular dispersion is an important parameter of a grating. The angular dispersion is obtained by deriving Eq. 2.4 with respect to β

$$\frac{\partial\beta}{\partial\lambda} = \left[\left.\frac{\partial\lambda}{\partial\beta}\right|_{\alpha=\text{const.}}\right]^{-1} = \frac{m}{a\cos\beta} \approx \frac{2\tan\alpha'}{\lambda} \ , \tag{2.19}$$

where in the last step Eq. 2.4 was used. The relation $\frac{dx}{d\lambda} = f\frac{d\beta}{d\lambda}$ then yields the linear dispersion

$$D \equiv \frac{d\lambda}{dx} = \frac{\lambda}{2f\tan\alpha'} \ . \tag{2.20}$$

Taking into account the double pass of the light through the spectrometer ($f = 2 \cdot 1.5$ m) this value is $D = 71.23$ pm/mm. A more accurate calculation by the manufacturer, taking into account the exact optical paths, is 1.294 times larger.
Before the light hits the CCD chip of the camera it passes through a telescope with a magnification of 6. A wavelength interval of 230 pm then fits to the CCD chip, which is sized 15×15 mm^2. As the chip constitutes of an array of 1024×1024 pixel^2 the calibration constant can be given as

$$c_\lambda = 0.23\frac{\text{pm}}{\text{pixel}} \tag{2.21}$$

or for the direct conversion into velocity units

$$c_v = \frac{c_\lambda}{\lambda}c = 104\frac{\text{m}}{\text{s pixel}} \tag{2.22}$$

for a wavelength around $\lambda = 664$ nm.
In order to verify these specifications a calibration spectrum was recorded (see Fig. 2.16). The lines $\lambda_1 = 663.8221$ nm (corresponding to the transition $4p^4D_{3/2} \rightarrow 3d^4F_{5/2}$) and $\lambda_2 = 663.9740$ nm (corresponding to the transition $4p^4D_{1/2} \rightarrow 3d^4F_{3/2}$) were identified in a typical argon discharge in PSI-2. On the CCD chip these lines were separated by 658 pixels which confirms the previous value: 658 pixel/$(\lambda_2 - \lambda_1)$=0.23 pm/pixel.
At this point it should be noted that the radiation passes a low resolution prism pre-monochromator before it enters the spectrometer in order to

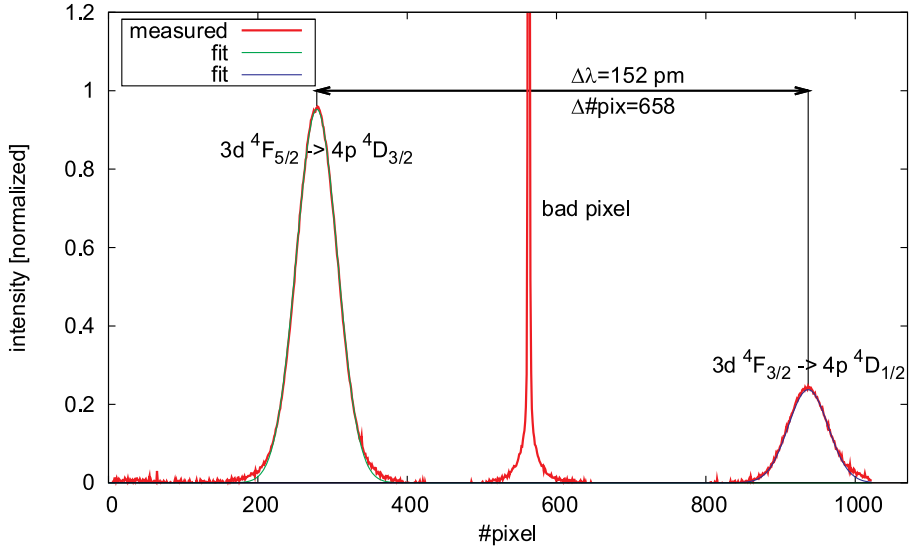

Figure 2.16: Calibration spectrum. The lines 663.8221 nm ($4p^4D_{3/2} \rightarrow 3d^4F_{5/2}$) and 663.9740 nm ($4p^4D_{1/2} \rightarrow 3d^4F_{3/2}$) were identified in a typical argon discharge in PSI-2. The calibration constant is found to be 0.23 pm/pixel for a wavelength of about 664 nm.

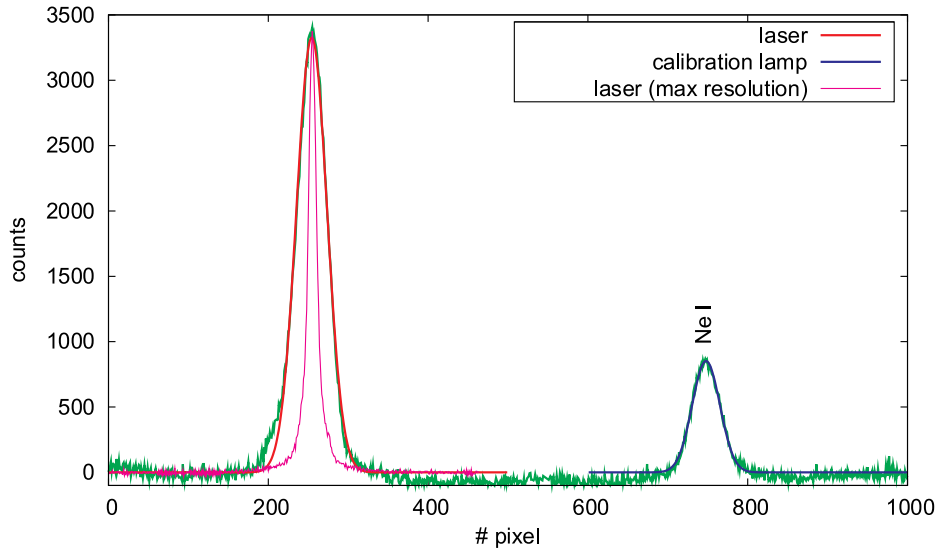

Figure 2.17: Spectrogram of the laser and the spectral lamp under standard conditions. For comparison the laser line is also shown when the spectrometer is operated under optimum conditions. The band width of the laser is at least as small as 14 pixel $\times$ 0.23 pm/pixel = 3.5 pm. According to the specification by the manufacturer it should even be three orders of magnitude less.

avoid an overlap of the different orders of diffraction. For unknown reasons the monochromator did not work properly and lines of the 9^{th} order were found within the spectra of the 8^{th} order. This circumstance, however, turned out to be useful since a line from a neon calibration lamp ($\lambda_{NeI} = 590.64294$ nm, cf. [56]) could be measured simultaneously to the laser wavelength (cf. Fig. 2.17). Since the changes in wavelength to be measured are in the sub picometer range and as the spectrometer is filled with atmospheric air it was very important to measure this reference line. Although the air temperature inside the spectrometer could be stabilized by means of a temperature controller, the gas density n_{air} and therefore the refractive index $N_{air}(n_{air}) = 1 + 2.76 \times 10^{-4} n_{air}/n_{norm}$ drift when the air pressure changes. A difference of 15 hPa, which may happen easily between two experimental days, would cause the line to drift by $\Delta\lambda = 2.7$ pm. This corresponds to a Doppler shift of more than 1000 m/s.
The reader might wonder whether the laser line and the line of the spectral lamp are affected in the same way when N_{air} drifts. As Fig. 2.18 shows, the neon lines $\lambda_{Ne1} = 665.20925$ nm and $\lambda_{Ne2} = 591.3633$ nm, observed at $9/8\lambda_{Ne2} = 665.2837$ nm, drift by exactly the same amount when the temperature regulator is set from 23°C to 40°C. This result is not surprising since N_{air} affects the wavelength linearly. In the following any dependency of the refractive index on the spectral range is neglected and the laser wavelength is always determined relative to that of the spectral lamp.
Finally the central wavelength of the Ar^+ $3d^4F_{9/2} \rightarrow 4p^4D_{7/2}$ transition has to be found. A simple way of approximating this wavelength is to make use of the light emission of the discharge itself. However, it has been observed (cf. [46]) that the plasma rotates at angular frequencies in the kHz range. It is then difficult to adjust the light collecting optics such that the mean azimuthal velocity in the observed volume is exactly zero.
A more accurate method is to measure an ion velocity distribution function at a fixed position when the laser is launched once in the axial direction and once in the counter-axial direction into the device. Due to the finite streaming velocity the wavelength is shifted to the blue in the first case[5] and to the red in the latter. Such a measurement is shown in Fig. 2.19. The wavelength of the transition when the ion is at rest is located in the center of the two maxima.

[5]Note that the ion 'sees' the laser radiation shifted to the red when moving in the same direction. In order to excite the transition the laser has to be tuned to the blue in order to compensate this shift.

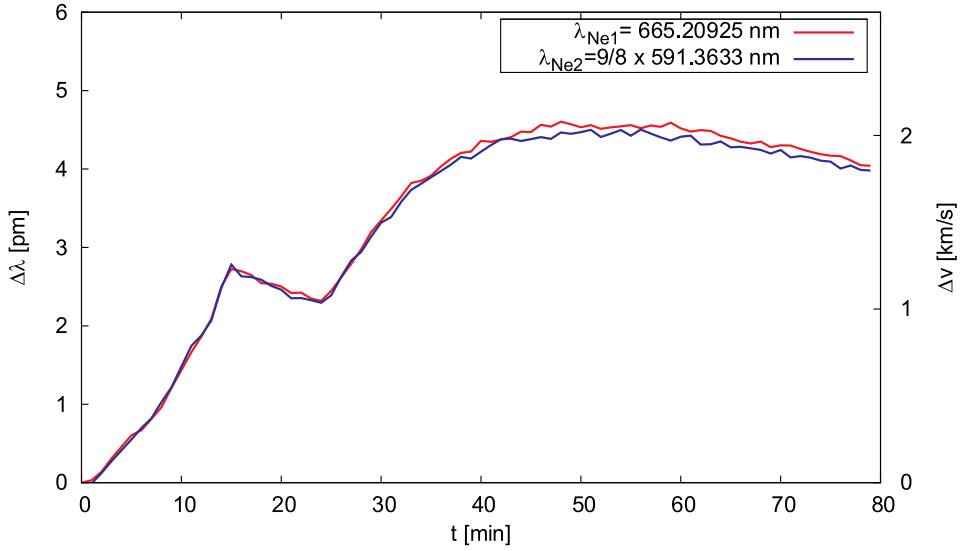

Figure 2.18: Drift of the spectral lines when the temperature inside the spectrometer is increased from 23°C to 40°C.

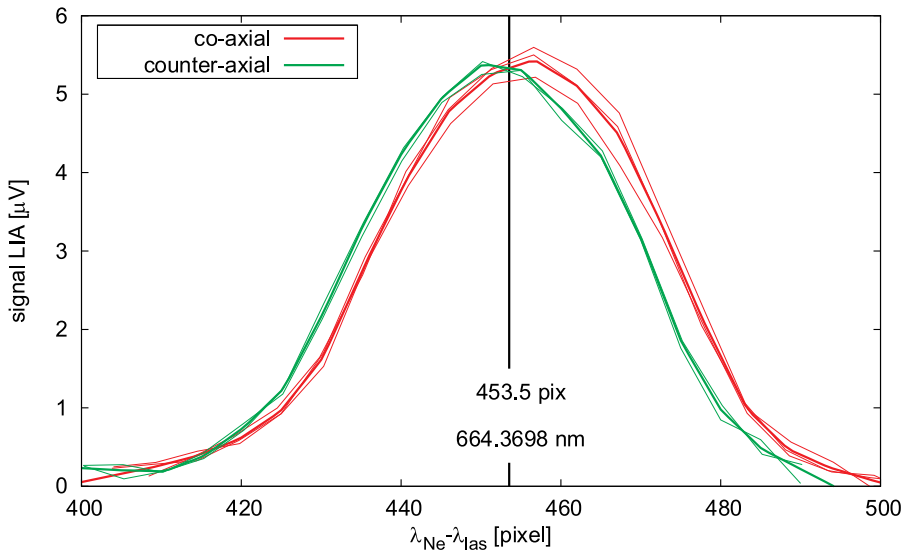

Figure 2.19: Determination of the central wavelength. The same ivdf is measured twice, launching the laser first in the co-axial and then in the counter-axial direction. The non-shifted wavelength is located in the middle of the two maxima.

2.2.5 Corrections of vignetting effects

If the LIF signal is measured close to the target surface, the space angle can be reduced due to vignetting effects. As the correction factor depends sensitively on the exact angle between the target surface normal and the axis of the target chamber, an experimental method was used to estimate this effect: A lamp is located at the position of the sensitive area of the photomultiplier. Its light is mapped by the optical lenses to the detection volume. If the manipulator is moved to a position, where the detection volume gets close to the surface, a light spot from the lamp becomes visible on the lateral surface of the target head. As indicated in Fig. 2.20 we can determine vignetted area A_v and to the total area of the spot A_{spot}. The ratio of the two yields the correction factor.

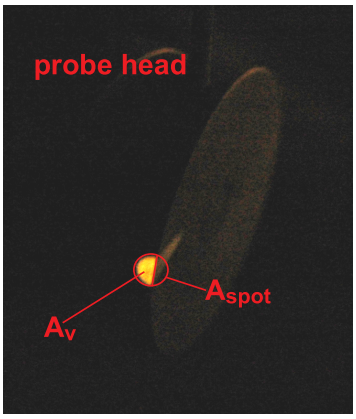

Figure 2.20: Vignetting by the target surface.

2.3 The current-force probe

Modern plasma physics and fusion research is inconceivable without a variety of diagnostics that measure essential plasma parameters like electron density and temperature, streaming velocity, etc. Historically one of the first and nowadays one of the most widespread diagnostics in plasma physics is the Langmuir probe. This device, constituting simply an electrode immersed in a plasma, determines electron density and temperature from the particle flux measured in the form of an electric current (cf. Sec. 4.1). Particle fluxes, however, are not the only quantity measurable by a probe. For example Bernd Koch [33, 34, 35] successfully measured energy fluxes onto a target making use of the thermoelectric effect. In this section a current-force probe is presented which is capable of measuring the momentum flux onto a surface. Such a measurement is not trivial since the force caused by the particles impinging a surface is quite small (of the order 1 mN) and at the same time the device is required to withstand the demanding conditions of plasma exposure. Thin membranes or any other filigree structures (such as those used in modern pressure gauges, which are orders of magnitude more sensitive) would be damaged by the high heat fluxes, often of the order 10 MW/m^2 in a fusion device.

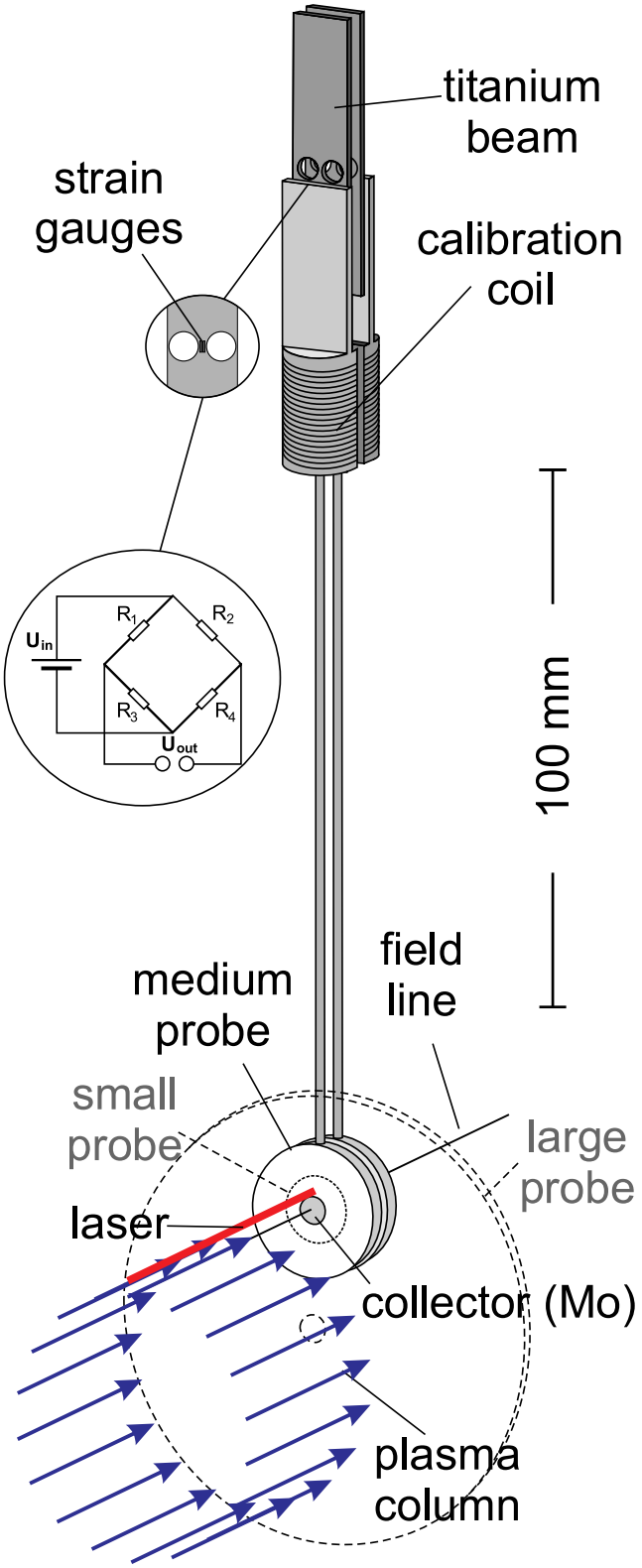

Figure 2.21: Schematic assembly of the current-force probe

The delicate elements of the probe shown in Fig. 2.21, the highly sensitive semi-conductor strain gauges, are located outside the plasma where they are protected from the high heat fluxes. These strain gauges are made from p-doped silicon which changes its resistivity strongly under deflection. The force is mediated by a Al_3O_2 rod, which is connected to the probe head, a circular disk made from boron nitride[6] immersed in the plasma. This arrangement constitutes a pendulum that is most significantly deflected at the position of minimum stiffness, *i.e.* at the position where two holes are drilled into the titanium beam connected to the rod. The semi-conductor strain gauges (manufacturer Micron Instruments) are glued to a small bridge left between the holes, two on each side of the beam. They are connected in the form of a Wheatstone bridge giving an output voltage U_{out} when an input voltage U_{in} is applied and the pendulum is deflected. The arrangement goes back to Chavers *et al.* [9] who applied a very similar device to measure the momentum flux in a plasma thruster. Although mechanical probes are not very common in plasma physics, first attempts to measure the deflection of a pendulum in a plasma were successful as early as 1962. At that time Waelbroeck *et al.* [66] tested such a device in an 'electrodeless plasma gun'. As the density was as high as 10^{21} m^{-3} the forces were relatively easy to measure. In the following years, however, no indications are found in the literature that similar probes have been used.
The novelty of the device shown in Fig. 2.21, with respect to that developed by Chavers *et al.* , is that two pendulums are placed close together so that the rear sides of the heads are screened from plasma exposure. Positioned in this way, the individual forces on both sides are measured and not only the net force on a single head. In general, the signals are also much larger.
An electrical collector is located in the center of each head, which measures the current-voltage characteristics. The probe then also constitutes a Mach probe[27].

2.3.1 Calibration

For the calibration the same arrangement was used as in [9]. Using thin, almost weightless strings, the weight forces of different known test masses were exposed to the pendulum while recording[7] U_{out} (Fig. 2.22). Doing the same procedure with different masses, a linear dependence between U_{out} and

[6]Boron nitride (BN) is an insulating material with a high melting point (2700°C) and a low vapor pressure, which is often used in plasma physics.

[7]The signal is amplified by the pre-amplifier SR560 (Stanford Research) and recorded using the Nicolet 'Vision' data acquisition system.

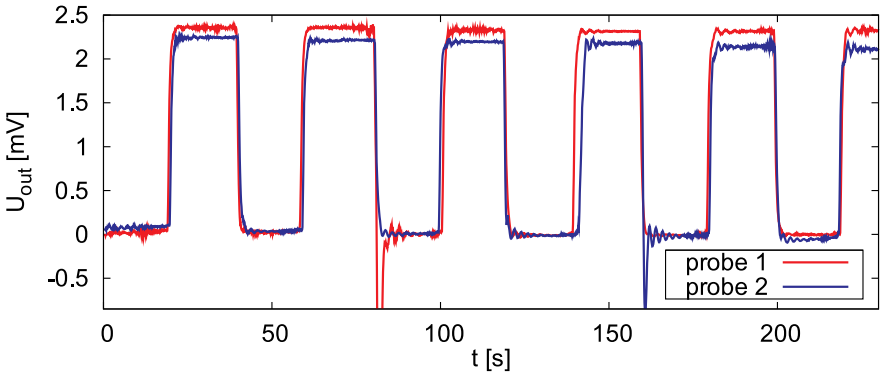

Figure 2.22: Output signal U_{out} at the Wheatstone bridge when applying an input voltage of $U_{in} = 5$ V and when exposing six times a weight force of $F = m_t g$ to the pendulum. The test mass was $m_t = 49.45$ mg. Note that the string was not fixed in the center of the probe head, but $\Delta l_1 = 55$ mm above in the case of the first pendulum, and $\Delta l_2 = 70$ mm in case of the second.

the force F

$$U_{out} = \alpha \cdot F \cdot U_{in} + U_{offs} \tag{2.23}$$

is found, where U_{offs} is an offset voltage that drifts on a time scale of several minutes in the range of some μV and cannot be suppressed. Here, however, it was subtracted from the original signal. The calibration constants for the two pendulums are found to be

$$\alpha_1 = 0.299 \pm 0.003\mathrm{N}^{-1} \text{ and } \alpha_2 = 0.302 \pm 0.008\mathrm{N}^{-1} \ . \tag{2.24}$$

An alternative method to calibrate the probe is through the use of the calibration coils shown in Fig. 2.22. A current I driven through these coils interacts with the vacuum magnetic field $\vec{B}$ and causes the torque

$$\tau = \vec{B} \cdot \vec{n} A I N_w \tag{2.25}$$

in the pendulum. A is the coil area, $\vec{n}$ the surface normal (vertical unit vector), and N_w the number of windings. If l is the length of the pendulum, this torque is equivalent to a force $F = \tau / l$ acting on the surface of the probe head. As the coil area is afflicted by a large error the first calibration method is preferred. However, the calibration coils were used to test whether the calibration remains constant during the measurements. In view of the large heat loads the probe heads are exposed to and the fact that the small

bridge in the titanium beam is the only mechanical connection with the rest of the machine, this constancy could not necessarily be assumed from the beginning. However, the calibration was found to be constant during all the measurements presented in Sec. 4.7.

Chapter 3

Passive and active spectroscopy on the Ar^+ ion

The emission spectra of a plasma contain plenty of information about the actual plasma state. The intensities of the spectral lines depend on the electron energy distribution (*i.e.* on the temperature, if the electrons are thermalized) and on the electron density. Collisional radiative models, which take into account the relevant atomic processes (electron impact excitation/de-excitation, spontaneous emission, absorption for all atomic levels) for the large number of energy levels, are used to compute these intensities.
In fusion research atomic beams are often applied as a diagnostic. With the help of collisional radiative models, particularly for elements with a relatively simple atomic structure like helium or lithium, the electron density and temperature can be deduced from the spectra measured on such atomic beams. Detailed information about the helium beam diagnostics applied at the edge plasma of a Tokamak can be found, for example, in the PhD thesis of Mathias Brix [8]. A thermal helium beam was also applied in PSI-2 by Petra Kornejew [36].
In addition to the intensities, the line shapes carry information about the particles in the plasma. Magnetic and electric (micro-) fields cause a splitting and/or broadening of the lines. In high density plasmas n_e is often deduced from the Stark effect (cf. [64]). For the moderate densities and the relatively high ion temperatures in PSI-2 the Doppler broadening is much more pronounced than the Stark (and the Zeeman) broadening which can be neglected. By measuring the exact shape of the line we will be able to determine the velocity distribution of the ions.
Active and passive methods have to be distinguished. We talk about 'passive' spectroscopy when observing the radiation from the plasma by a spectrograph without exciting the atoms externally. Passive spectroscopy is com-

pletely non-invasive but has the disadvantage of being line-integrating. Making symmetry assumptions a higher spatial resolution might be achieved by performing Abel inversions, but often the uncertainties remain quite high.
We are concerned with active spectroscopy, when a laser or any other light source is used to excite the plasma atoms/ions. One example is the Laser Induced Fluorescence diagnostic, which is described more in detail in Sec. 2.2. The detection volume on one hand side is limited by the diameter of the laser beam and on the other hand by the detector aperture, and so a high spatial resolution can be achieved.
As almost all measurements shown in the present work were carried out in argon plasmas, here we setup a simple collisional radiative model for Ar^+. To do so a list of all the atomic levels is first required. Some of these levels (and transitions) were computed from first principles by Saha and Fritzsche [55] but a more comprehensive set can be found in the spectral database from the National Institute of Standards and Technology (NIST), Gaithersburg [53]. This data was used to plot the Grotrian diagram shown in Fig. 3.1 and is reproduced in the appendix Tab. A. For all the levels inside the boxed region the last shell has the configuration $3s^2 3p^4[x]nl\,^{2S+1}L_J$. We use the common abbreviation $nl'\,^{2S+1}L_J$, where a single prime stands for $[x]=[^1D]$, a double prime for $[x]=[^1S]$, and where the case $[x]=[^3P]$ is unprimed. From the 418 levels (black) tabulated for Ar^+ in the NIST[53] atomic database, there are rate coefficients available for 84 levels (blue).

3.1 Collisional radiative model

Due to the large number of processes involved collisional radiative models are often quite complex and generally difficult to set up. Furthermore the model can only be as good as the atomic data fed into it. Rather than trying to make accurate quantitative predictions on the intensity of certain spectral lines in this chapter we want to make an estimation of the population densities – in particular of those atomic levels relevant for LIF. A very important question also concerns the time scale on which these population densities change as an ion moves from one region at certain plasma condition to another region with different plasma parameters or when the population is perturbated due to the interaction with the laser. This question will be addressed in sections 3.3 and 3.4.
The only atomic data fed into the model presented here are the 84 energy levels E_i given in Tab. A.1, together with their statistical weights g_i and the Einstein-coefficients A_{ij} for spontaneous emission (Tab. A.3). These were also taken from [53] and are reproduced in the appendix A. For some meta-stable

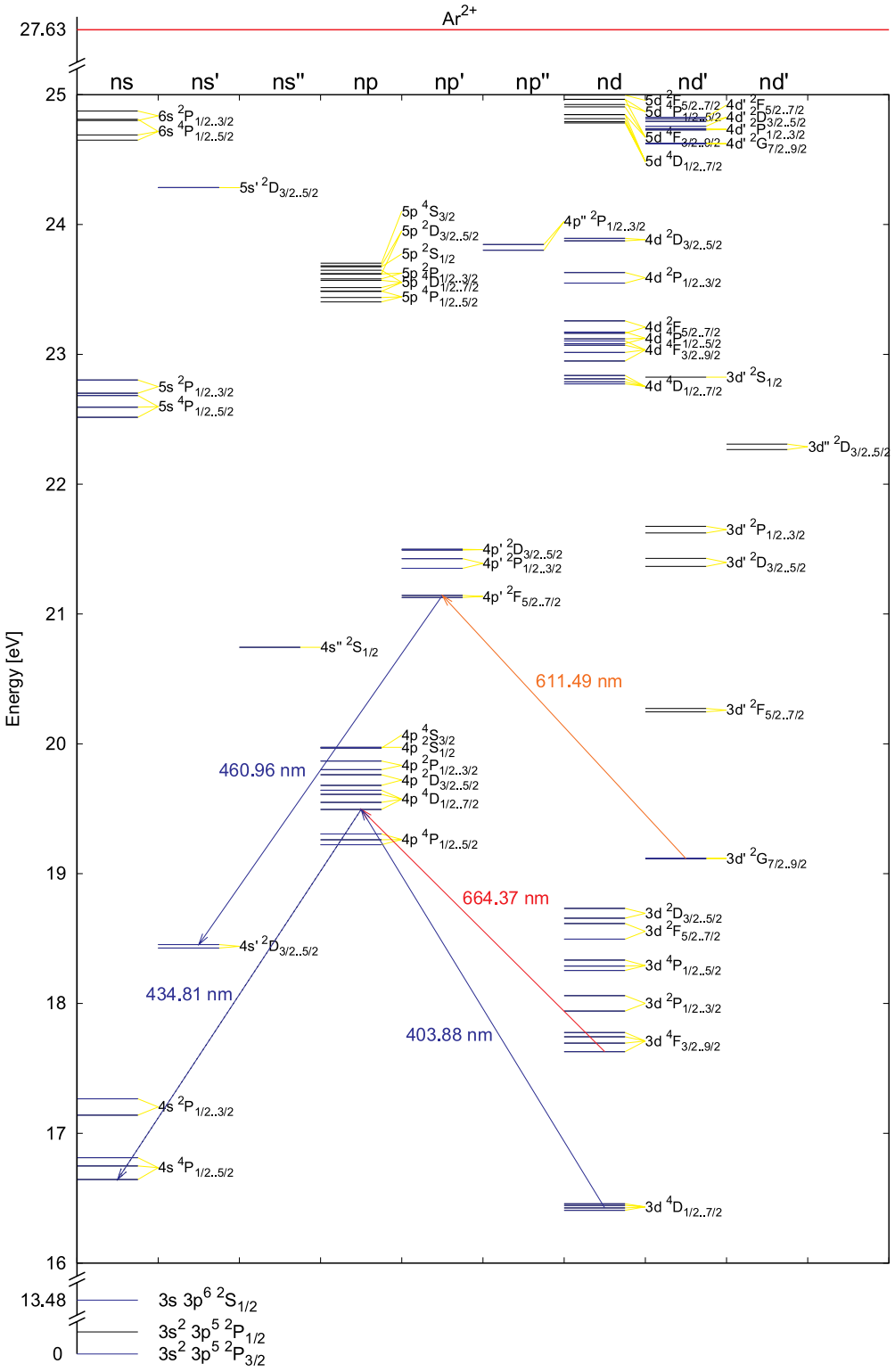

Figure 3.1: Grotrian diagram of the Ar^+ ion. Three selected three-level processes in the visible range are shown.

levels life times are provided by Schef *et al.* [51] (cf. Tab. A.5).
According to Seaton and Regemorter (cf. [28]) the electron-impact-excitation rate coefficients for optically allowed transitions are approximated by:

$$X_{ji} = \left\langle \sigma_{ji}^{X} v \right\rangle = 3.15 \cdot 10^{-13} f_{ji} \frac{R_y}{E_{ij}} \sqrt{\frac{R_y}{T_e}} \exp\left(-\frac{E_{ij}}{T_e}\right) \overline{g}_X \frac{m^3}{s} \ , \tag{3.1}$$

where the oscillator strengths f_{ji} are related to the Einstein coefficients for spontaneous emission A_{ij} and the statistical weights g_i [53] via

$$f_{ji} = \frac{2a_0}{\alpha^4 c} \left(\frac{R_y}{E_{ij}}\right)^2 \frac{g_i}{g_j} A_{ij} \ . \tag{3.2}$$

$E_{ij} = E_i - E_j$ is the energy difference between the upper level E_i to the lower level E_j, $R_y = 13.6$ eV the Rydberg constant, $a_0 = 0.529 \times 10^{-10}$ m the Bohr radius and $\alpha = 1/137.036$ the fine-structure constant. The gaunt factor $\overline{g}_X$ in Eq. 3.1 is assumed to be 0.2 for transitions with $\Delta n \geq 1$ and 1 otherwise. Optically forbidden transitions are neglected completely.
The corresponding coefficients for de-excitation can be obtained from the detailed balance

$$Y_{ji} = \frac{g_j}{g_i} \exp\left(\frac{E_{ij}}{T_e}\right) X_{ij} \ . \tag{3.3}$$

The highest energy level labeled by $i_{ion} = 83$ constitutes the ground state of doubly ionized argon. It is connected to the rest of the levels by ionization and recombination. Formulae for these processes are also found in [28]:

$$S_{ii_{ion}} = \left\langle \sigma_i^S v \right\rangle = 1.7 \cdot 10^{-14} \left[\frac{R_y}{\chi_i}\right]^2 \sqrt{\frac{T_e}{R_y}} \exp\left(-\frac{\chi_i}{T_e}\right) \left[1 - \exp\left(-\frac{5\chi_i}{T_e}\right)\right] \overline{g}_S \frac{m^3}{s} \tag{3.4}$$

and

$$R_{i_{ion}j} = \left\langle \sigma_n^R v \right\rangle = 5.2 \cdot 10^{-20} Z \left(\frac{\chi_j}{T_e}\right)^{3/2} \exp\left(\frac{\chi_j}{T_e}\right) \mathrm{Ei}\left(\frac{\chi_j}{T_e}\right) \overline{g}_R \frac{m^3}{s} \ , \tag{3.5}$$

where $\mathrm{Ei}(x) = \int_x^\infty e^{-x'}/x' dx'$ is the exponential integral function. $Z = 18$ is the atomic number and $\chi_i = E_{i_{ion}} - E_i$ the energy difference from E_i to the second ionization level $E_{i_{ion}} = 27.63$ eV. The gaunt factors in Eqs. 3.4-3.5 are assumed to be

$$\overline{g}_S = 1 + \frac{\sqrt{3}}{\pi} \ln\left(1 + \frac{T_e}{\chi_i}\right) \quad \text{and} \quad \overline{g}_R = 1 \ . \tag{3.6}$$

Finally, the argon ion may interact with electromagnetic radiation produced either by the plasma itself or originating from an external source, *e.g.* a laser. While we neglect the first (*i.e.* we assume the plasma to be optically thin) the latter is addressed in Sec. 3.4.
It is well known that the Einstein coefficients B_{ij} for absorption (or induced emission B_{ji}) are related to the ones of spontaneous decay A_{ij} by

$$B_{ij} = \frac{c^3 h^2}{8\pi E_{ij}^3} A_{ij} \quad \text{and} \quad B_{ji} = \frac{g_i}{g_j} B_{ij} \ . \tag{3.7}$$

The time development of the population densities N_i of the ion can be written in matrix notation as a single differential equation

$$\frac{d}{dt}\vec{N} = \mathbf{CR}' \cdot \vec{N} \ , \tag{3.8}$$

where all the collisional radiative processes mentioned above are combined in a single matrix

$$\mathbf{CR}' = \left[\mathbf{A} + n_e \left(\mathbf{X} + \mathbf{Y} + \mathbf{S} + \mathbf{R}\right) + \mathbf{u} \cdot \mathbf{B}\right]^T{}' \ . \tag{3.9}$$

Note that, due to its dependence on the wavelength $u_{ij} = u(\lambda_{ij})$, the radiation energy density is also a (symmetric) matrix here. We have to apply the $'$ operator defined by

$$A'_{ij} = A_{ij} - \delta_{ij} \sum_k A_{kj} \tag{3.10}$$

to account for the fact that a particle which makes a transition from i to j not only increases the population of N_j but also decreases N_i. This operator is linear and assures particle conservation (the sum over a column of any primed matrix is 0).
Since by convention the Einstein coefficient A_{if} describes the transition from an initial state i to a final state f we have to take the transposed matrix to define Eq. 3.8.
Eq. 3.8 is now solved by

$$\vec{N}(t) = \sum_i a_i \vec{v}_i \exp(w_i t) \tag{3.11}$$

where $\vec{v}_i$ are the eigenvectors and w_i are the eigenvalues of the CR' matrix. These can be determined numerically by standard methods which are implemented in almost any commercial mathematics software. The pre-factors a_i are selected such that $N(t)$ is in accordance with the initial condition $\vec{N}(t=0) = \vec{N}_0$. We can for example calculate the mean occupation at the time τ of a test particle exposed to the plasma assuming that the particle is initially in the ground state $\vec{N} = \vec{e}_0$. For different plasma conditions this occupation is computed in Tab. A.1.
Finally, the mean (theoretical) number of photons emitted by such an ensemble of test particles per second at the wavelength $\lambda_{ij} = hc/\left(n_{air}(E_i - E_j)\right)$ is given by

$$I_{ij,th} = A_{ij} N_i \ . \tag{3.12}$$

3.2 Passive spectroscopy

The quality of this simple collisional radiative model shall now be evaluated by comparing theoretical spectra with spectra measured in PSI-2. The light emission of an argon plasma produced under two different discharge conditions is coupled into an Échelle spectrometer (manufacturer GWU, model Spectrell) by means of an optical fiber and a collimation optics. As in the case of the LIF experiments, the last viewport of the target chamber was used (cf. Fig. 2.1). The line of sight is parallel to the x-axis (a coordinate system was introduced in Sec. 2.2.2) but in contrast to the LIF-measurements the observation volume is centered on the axis of the plasma column. Since the plasma is axially symmetric we can measure the n_e and T_e profile along the line of sight by means of the Langmuir probe shown in Fig. 2.1.
Échelle spectrometers cover a large spectral range and at the same time measure at a relatively high resolution ($\Delta\lambda_{FWHM} = 25$ pm). Due to its working principle no movable parts are used in this type of spectrometer and the wavelength calibration is very stable. With the calibration provided by the manufacturer all spectral lines could be identified unambiguously. In order to calibrate the CCD chip sensitivity of the spectrometer the observation optics was directed towards an integrating sphere (labsphere, USS 1200) after performing the measurements in the plasma. As the distance was about the same we obtain the radiant flux density u_m directly by dividing the spectra S_{plasma} measured in the plasma by those from the integrating sphere S_{IS} and multiplying with the calibration spectrum u_{IS} provided by the manufacturer

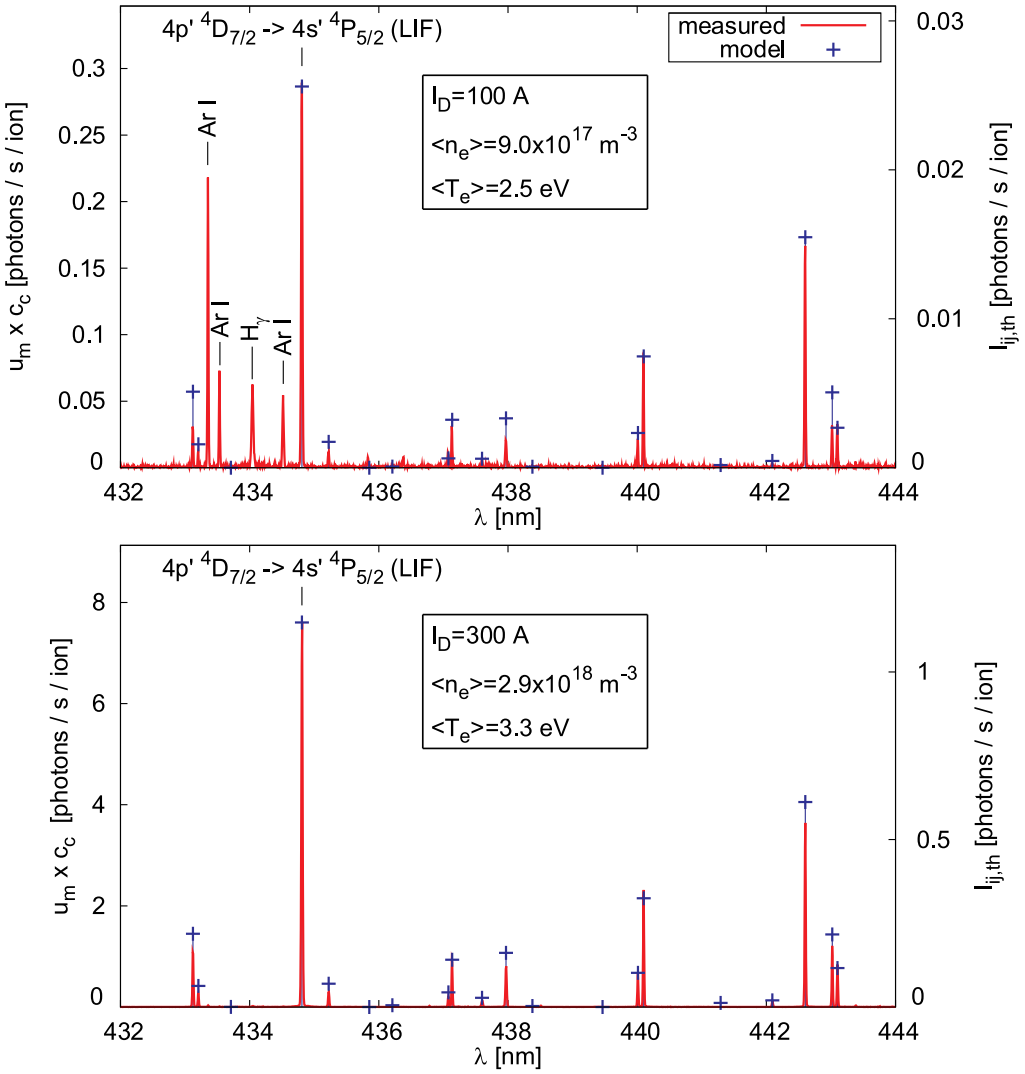

Figure 3.2: Measured and simulated spectra of an argon discharge at two different discharge conditions. For moderate densities and temperatures (top) some lines of the neutral argon are found in the spectrum. These lines become very weak at higher electron densities and temperatures (bottom).

of the sphere (cf. Tab. A.6)

$$u_m = \frac{S_{plasma}}{S_{IS}} u_{IS} \ . \tag{3.13}$$

In order to compare a measured spectrum to the simulations we have to multiply by

$$c_c(\lambda) = \frac{\lambda}{hc} \frac{\Delta\lambda_{FWHM} 4\pi}{\langle n_e \rangle \, \Delta x} \ , \tag{3.14}$$

where $\langle n_e \rangle$ is the mean density over the observation volume and Δx is its extension. The height of a spectral line then indicates the number of photons emitted per ion and per second into the full space angle 4π. Fig. 3.2 shows a section of the measured and computed spectra for the two different plasma conditions mentioned. Remembering that in our model we neglected the forbidden transitions completely and that the excitation coefficients depend *very* sensitively on electron temperature and density, the agreement between the experiment and the modeling is already surprisingly good. This is not only a coincidence for in the small wavelength range shown in the figure but holds for the whole measured spectrum (about 300 nm). The total intensity of the strongest argon ion line $4p'\,^4D_{7/2} \rightarrow 4s'\,^4P_{5/2}$, which is also used for the LIF detection, is predicted by the model to within a factor of 11 in the upper graphic and to within a factor of 7 in the lower one. The relative spectra are also predicted quite well. Some of the lines differ by a factor of 2 or more from the measured ones but in general the ratios are reproduced very well.

For this reason we may assume that the main populating /depopulating processes of the metastable level $3d'\,^4F_{9/2}$ are spontaneous decays and electron impact excitation / de-excitation of optically allowed transitions. One might argue that we cannot say anything about the population of our metastable level since no (electric dipole) radiation is emitted from this level. However, it can be shown easily that the strength of other lines (e.g. the strongest ion line at 435 nm) depends significantly on its occupation. If the electron impact excitation from the ground state was assumed as high as for an energetically neighboring level (*e.g.* $4s\,^2P_{1/2}$) the measured and the simulated spectra would disagree significantly.

As an additional result we are now able to compute the total power radiated by the argon ions in the discharge. Assuming a uniform density and temperature profile in axial direction, the total power radiated by the $I_D = 100$ A discharge is about 75 W and about 1.5 kW (about 10% of the total discharge power) in the case of the $I_D = 300$ A discharge (taking into account the factors 11 and 7 mentioned before).

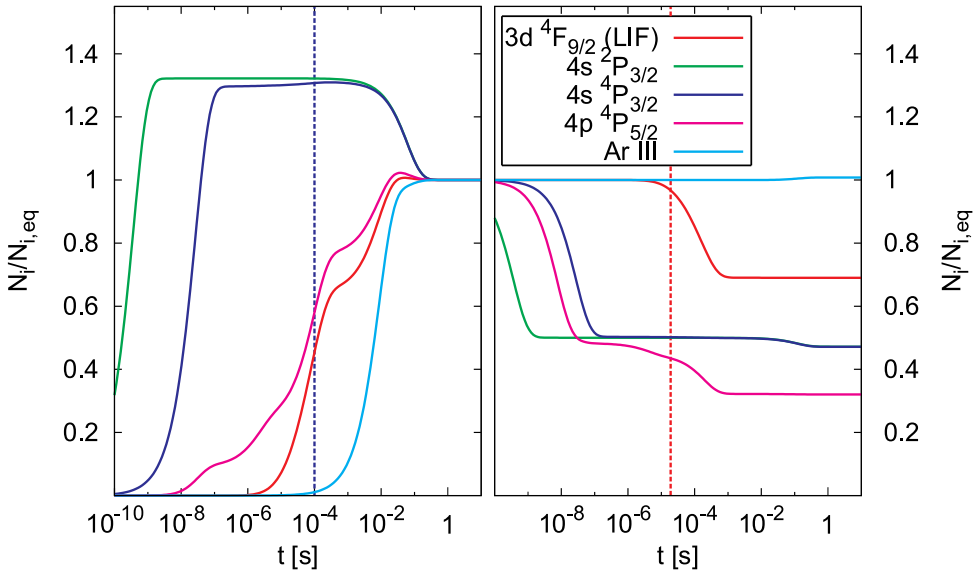

Figure 3.3: Temporal evolution of the population density (normalized to the equilibrium density) of the selected energy levels of the Ar^+ ion. Left: a stream of test particles initially in the ground state is exposed to a plasma with an electron density of $n_e = 2 \times 10^{18}$ m^{-3} and a temperature of $T_e = 2$ eV. Right: the same test particles are then exposed to a plasma at the same temperature but at half of the density.

3.3 Temporal evolution of the population densities

With Eq. 3.11 we are able to study the temporal evolution of the population of the different atomic levels. Fig. 3.3 shows the behavior of an ensemble of test particles initially in the ground state which are exposed to a plasma with an electron density of $n_e = 2 \times 10^{18}$ m^{-3} and a temperature of $T_e = 2$ eV. Very different time scales are involved. After about 1 ns the population of the $4s\,^2P_{3/2}$ state is almost at its equilibrium value. In contrast, a significant population of the metastable level $3d'\,^4F_{9/2}$ is found to require a time of about 10-100 μs. The ionization equilibrium would not be reached before 100 ms. However, even particles which move unperturbed through the discharge at the mean streaming velocity have a shorter life time of only $\tau = 3\,\mathrm{m}/(300\,\mathrm{m/s}) = 10$ ms and so the plasma is in a non-equilibrium state. Due to the frequent charge exchange and ionization processes we assume an even shorter characteristic dwell time in the plasma of $\tau = 100$ μs which is indicated by the dashed blue line in the figure.

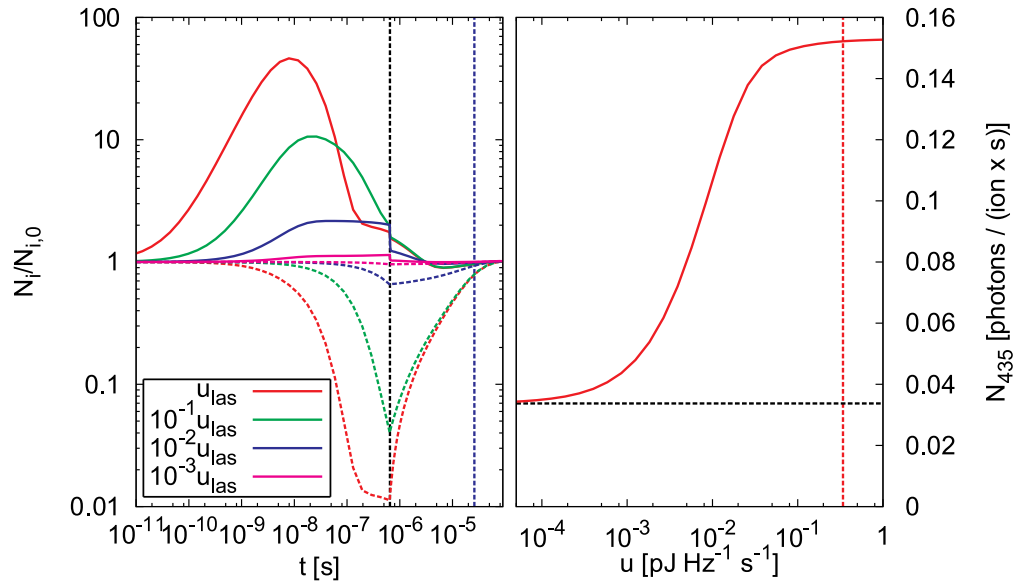

Figure 3.4: Left: temporal evolution of the upper and lower LIF levels during and after a laser pulse. Right: total number of LIF-photons emitted during laser pulses with different power densities per spectral interval if T_i was 0.

An important question that arises with respect to the measurements in Chapter 4 is how fast the population density changes if an ion passes a region with a strong density gradient. The right graph of Fig. 3.3 shows the evolution of the population density when the plasma density is decreased to one half instantaneously. After the characteristic time of flight $\tau = 20$ μs of a thermal ion over a distance of 5 cm the population of the metastable level is still practically constant.

3.4 Laser Induced Fluorescence / Saturation broadening

In this section we want to address the interaction of the ion with the laser radiation. The levels involved were introduced in the previous Chapter 2. A scheme was also shown in Fig. 2.4 there. The energy density per spectral interval u in Eq. 3.8 and Eq. 3.9 then has to be taken into account. The total power of the laser beam is $P_{las} = 8$ mW and the radius about $r_{las} = 1$ mm.

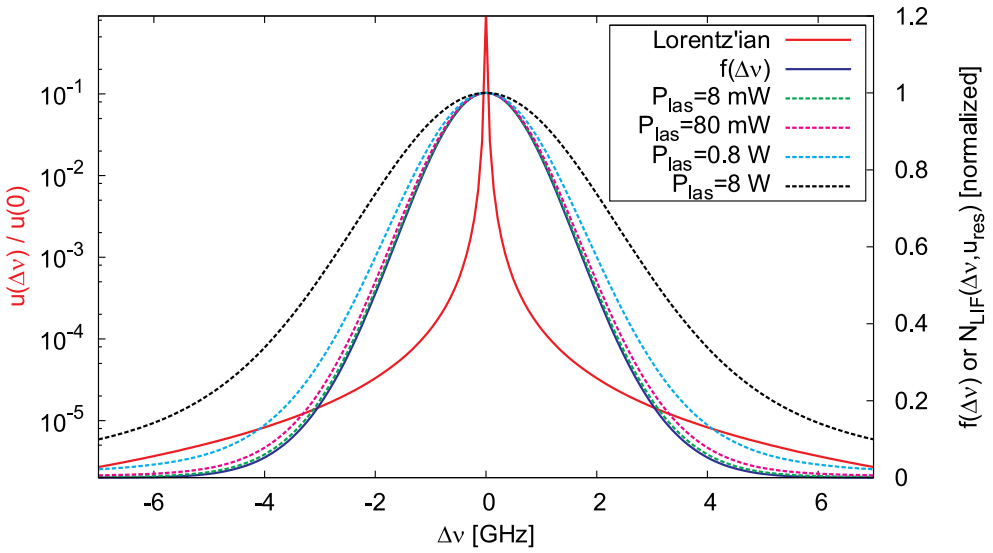

Figure 3.5: Saturation broadening of the resonance line of ions at $T_i = 0.5$ eV.

Therefore

$$\int u(\nu)d\nu = \frac{P_{las}}{\pi r_{las}^2 c} \ . \tag{3.15}$$

According to the manufacturer the spectral width of the laser is in the range of a few MHz. This is smaller than the natural line width of the transition which is given by

$$\Delta\nu = \frac{\sum_j A_{ej}^T + \sum_j A_{mj}^T}{2\pi} = 23 \text{ MHz} \ , \tag{3.16}$$

where only the transitions from the excited level (m) contribute to the sum since for the metastable (e) we have $\sum_j A_{mj}^T \approx 0$. As the line has a Lorentzian shape we can introduce an effective u as

$$u(\nu') = u_{res} \frac{1}{1 + \left[\frac{2(\nu' - \nu_{me})}{\Delta\nu}\right]^2} \ , \text{ where } u_{res} = \frac{P_{cw}}{\pi r_{las}^2 c} \frac{2}{\pi \Delta\nu} \tag{3.17}$$

which fulfills Eq. 3.15. $\nu_{me} = (E_e - E_m)/h$ is the frequency of the transition and

$$\nu'(\nu, v) = \nu(1 - v/c) \tag{3.18}$$

the Doppler shifted frequency in the frame of the ion moving at a velocity v. The laser is modulated at a frequency of $\nu_{mod} = 100$ kHz. As the gyro radius of a thermal particle $\rho_i = 13$ mm is larger than the diameter of the laser $2r_{las} = 2$ mm, the ions are exposed to the laser light for only about the $2r_{las}/(2\pi\rho_i)$ th part of one gyration period $t_{gyr} = 2\pi/\omega_i$, *i.e.* about $t_{exp} = 0.6$ μs. Instead of assuming 5 μs lasting on and off periods we have to assume a laser 'pulse' length of t_{exp} and an off period of $t_{gyr} - t_{exp}$ in our simulation.
Fig. 3.4 (left) shows the temporal evolution of the population of the LIF levels (solid lines = excited level, dashed lines = metastable level) normalized to their unperturbed values during the exposure of a laser pulse at different intensities. Note the double logarithmic representation of the graph. The pulse starts at $t = 0$ s and ends at t_{exp} (black dashed vertical line). A gyration period is completed after t_{gyr} (blue dashed vertical line). It is found that the lower (metastable) level is re-occupied when the ion gyrates into the laser beam and so we may neglect the interaction of the ion with the laser during the previous gyration period. We determine the total number of photons emitted at $\lambda = 435$ nm during a laser pulse by integrating Eq. 3.8 from 0 to t_{exp} and multiplying by A_{ef}

$$N_{435}(u) = A_{ef} \int_0^{t_{exp}} \vec{N}_e(t)dt = A_{ef} \sum_i \frac{a_i}{w_i} \vec{v}_e \left[\exp\left(w_i t_{exp}\right) - 1\right] \ , \qquad (3.19)$$

where again the $\vec{v}_i$ and w_i are the eigenvectors and eigenvalues of the matrix $\mathbf{CR}' = \mathbf{CR}'(u)$ and where the coefficients a_i are determined from the initial condition. This function normalized to 1 s/t_{exp} is shown in Fig. 3.4 (right).
So far we have assumed that the ions were cold and that the laser is exactly in resonance with the transition. If we want to determine the number of photons during a real laser pulse we have to integrate over the (normalized) ivdf $\widehat{f}(v)$. With Eq. 3.18 the number of LIF photons is given by

$$N_{LIF}(\nu, u_{res}) = \int_{-\infty}^{\infty} \widehat{f}(v') N_l\left(u\left(\nu'(\nu, v')\right)\right) dv' \ , \text{ where} \qquad (3.20)$$

$$N_l(u) = N_{435}\left(u\right) - N_{435}(0) \ . \qquad (3.21)$$

Taking into account that the optical system collects approximately 5 times more background light than originates from the detection volume (cf. Sec. 2.2.2) a signal to background ratio of

$$\frac{N_{LIF}(\nu_{me}, u_{res})}{5N_{435}(0)} = 1.6\% \qquad (3.22)$$

is in reasonable agreement with the result found in Sec. 2.2.3 that only 1% of the photons originates from a LIF process.

Another question we want to address here is the apparent broadening of the spectral line with increasing laser power. Goeckner and Goree treated this problem in [19]. Their results, however, cannot be adapted directly to the present situation since the broadening was computed for a laser with a spectral width of 1 GHz.
Evaluating Eq. 3.20 for different values of u we can compute this broadening effect (cf.Fig. 3.5). If the laser power is in the range $P_{las} = 8$ mW, as in our case, $N_{LIF}(\nu_{ul} v/c, u_{res})$ has practically the same width as $\widehat{f}$, even if the temperature is as small as $T_i = 0.5$ eV. If the power were 1000 times higher, however, a significant broadening (black dashed curve) would be observed. The temperature deduced from a LIF measurement with such a powerful laser would be about three times too high. We can compute the mean frequency interval in which the LIF process is excited as

$$\delta\nu_{sat} = \left[\frac{\int_{-\infty}^{\infty} \widehat{f}(v') \left(\nu_{me} \frac{v'}{c}\right)^2 N_l \left(u\left(\nu'(\nu, v')\right)\right) dv'}{N_{LIF}(\nu, u_{res})} \right]^{1/2} = 0.26\,\mathrm{GHz}\ . \quad (3.23)$$

The corresponding velocity interval is $\delta v_{sat} = c\delta\nu/\nu_{me} = 170$ m/s. In summary this means that (due to the extremely narrow band width of the laser) saturation is actually occurring but that the broadening can clearly be neglected.

3.5 Zeeman effect

According to the Zeeman effect, the energy levels of atoms/ions lose their degeneration with respect to the magnetic quantum number M_J under the influence of a magnetic field. In a magnetic field B this energy shift is given by

$$\Delta E = \mu_B B M_J g_J \text{ , where } \mu_B = \frac{e\hbar}{2m_e}\ . \quad (3.24)$$

For the lower LIF-level ($3d^4F_{9/2}$) the Landé factor

$$g_J = 1 + \frac{J(J+1) + S(S+1) - L(L+1)}{2J(J+1)} \quad (3.25)$$

is $g_J = 4/3$, and for the upper level ($4p^4D_{7/2}$) it is $g_J = 10/7$. According to the selection rules only transitions with $\Delta M_J = 0, \pm 1$ are allowed. We distinguish between π-transitions ($\Delta M_J = 0$) and σ-transitions($\Delta M_J = \pm 1$).

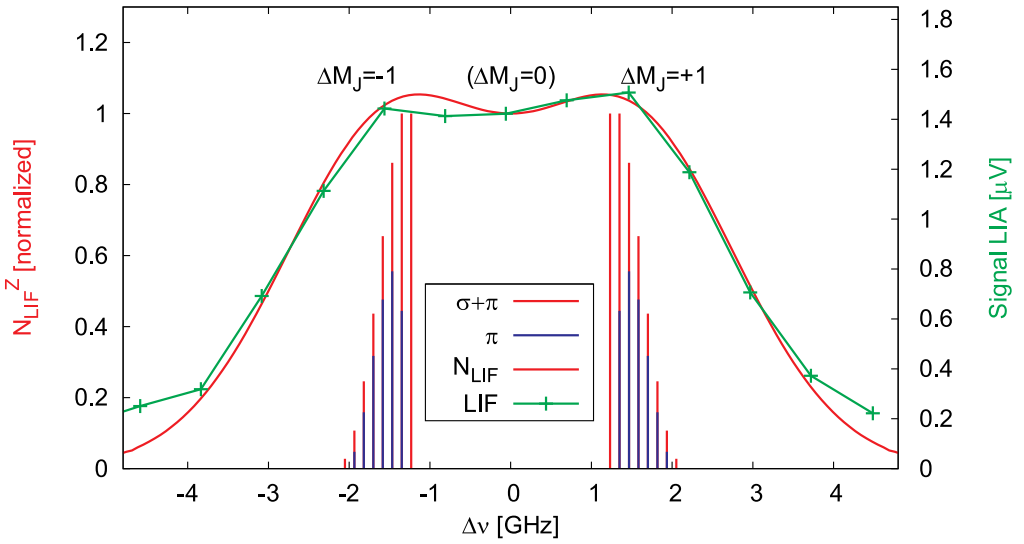

Figure 3.6: Vertical Lines: Intensities of the Zeeman components of the LIF process $3d\ ^4F_{9/2} \rightarrow 4p\ ^4D_{7/2} \rightarrow 4s\ ^4P_{5/2}$according to Eqs. 3.26-3.27. Red curve: simulated LIF signal for an ion temperature of $T_i = 0.25$ eV. Green curve: measured LIF signal at a low discharge current ($I_D = 100$ A), *i.e.* at a low density and temperature.

When observing the emission from the plasma perpendicular to the magnetic field lines (transverse observation), the lines from π-transitions are (linearly) polarized parallel to the magnetic field, while σ components are perpendicularly polarized. In the case where we observe the lines parallel to the magnetic field, the π-component is suppressed and the σ-components are circularly polarized. Due to the symmetry between absorption and emission, π-components are also suppressed when exciting the LIF-process with the laser.
We not only have to take into account whether a transition is allowed or not but also the actual strength of the lines. Sobelman [60] gives the relative intensities as follows:

$$I_{||,J\rightarrow J-1} = \begin{cases} 0 & \text{for} \quad \Delta M_J = 0 \quad (\pi) \\ \frac{1}{2}(J+M_J)(J-1+M_J) & \text{for} \quad M_J \rightarrow M_J - 1 \quad (\sigma) \\ \frac{1}{2}(J-M_J)(J-1-M_J) & \text{for} \quad M_J \rightarrow M_J + 1 \quad (\sigma) \end{cases} \tag{3.26}$$

and

$$I_{\perp,J\rightarrow J-1} = \begin{cases} J^2 - M_J^2 & \text{for} \quad \Delta M_J = 0 \quad (\pi) \\ \frac{1}{4}(J+M_J)(J-1+M_J) & \text{for} \quad M_J \rightarrow M_J - 1 \quad (\sigma) \\ \frac{1}{4}(J-M_J)(J-1-M_J) & \text{for} \quad M_J \rightarrow M_J + 1 \quad (\sigma) \end{cases} \tag{3.27}$$

The contribution of the different absorption lines to the LIF signal, *i.e.* the product of Eq. 3.26 and Eq. 3.27, is computed in Fig. 3.6 for a field strength of $B = 0.085$ T. The blue lines indicate the *emitted* contribution of π components.
We can now generalize Eq. 3.20 in order to study the convolution with the ivdf

$$N^Z_{LIF}(\nu, u_{res}) = \int_{-\infty}^{\infty} \widehat{f}(v') \sum_j \frac{I^j_\perp}{I^0_\perp} N_l \left(\frac{I^j_{||}}{I^0_{||}} u\left(\nu'(\nu_j, v')\right) \right) dv' \ , \tag{3.28}$$

where $\nu_j = \nu_{me} + \frac{B\mu_B}{h} \left(g_{J,m} M^j_{J,m} - g_{J,e} M^j_{J,e} \right)$ are the shifted frequencies of the 16 transitions ($j = 1 \ldots 16$) shown in Fig. 3.6. The normalization constants $I^0_{||}$ and $I^0_\perp$ have to be chosen in an appropriate way. Note that Eq. 3.28 can only be an approximation, since $\lim_{B\to 0} N^Z_{LIF} = N_{LIF}$ is not strictly satisfied. For a more refined treatment the splitting of the levels, together with the detailed transition rates between the different M_J states have to be taken into account in the collisional radiative model.
For low ion temperatures indications for the Zeeman splitting were found in the LIF-signal. The green curve in Fig. 3.6 shows the measured LIF signal in discharge with the relatively small current of $I_D = 100$ A. Assuming a Maxwellian distribution with an ion temperature as small as $T_i = 0.25$ eV N^Z_{LIF} fits the LIF signal very well for a magnetic field of $B = 0.085$ T. This is exactly the field we compute by Eq. 2.1. As with Eq. 3.23 we determine the frequency interval that contributes to the LIF-signal

$$\delta\nu_{Zee} = \left[\frac{\int_{-\infty}^{\infty} \widehat{f}(v') \left(\nu_{ik} \frac{v'}{c} \right)^2 \sum_j \frac{I^j_\perp}{I^0_\perp} N_l \left(\frac{I^j_{||}}{I^0_{||}} u\left(\nu'(\nu, v')\right) \right) dv'}{N^Z_{LIF}(\nu, u_{res})} \right]^{1/2} = 1.5\,\mathrm{GHz} \ . \tag{3.29}$$

In velocity units this corresponds to $\delta v_{Zee} = 960$ m/s.
The Zeeman effect is the strongest broadening mechanism (but less than the Doppler broadening of course). When evaluating the ion temperature we cannot neglect it. All the values for T_i evaluated in Chapter 4 are thus corrected by 0.5 eV. However, due to the symmetry of the effect the mean streaming velocity is not affected.

3.6 Stark broadening

The electric fields also cause a splitting/broadening of the levels due to the Stark effect. On a microscopic scale fluctuating electric fields are permanently present in the plasma because of the charged particles in the neighborhood of the atom/ion. The non-trivial quantitative study of this effect, *i.e.* the broadening of spectral lines is addressed by Griem [21, 22]. According to him a (non-hydrogen like) Stark broadened line has a Lorentz profile with a full width at half maximum of (cf. also [1, 47])

$$\Delta\lambda^S_{fwhm} \approx \left[1 + 1.75\alpha \left(\frac{n_e}{10^{22}\mathrm{m}^{-3}}\right)^{1/4} \left(1 - \kappa\frac{\overline{r}_i}{\lambda_D}\right)\right] 2\Delta\lambda_e \frac{n_e}{10^{22}\mathrm{m}^{-3}} \ , \quad (3.30)$$

where $\overline{r}_i = \sqrt[3]{3/(4\pi n_e)}$ is the mean distance between the particles and λ_D is the Debye length (Eq. 4.13). $\kappa = 0.75$ in the case of neutral atoms and 1.2 in the case of singly ionized atoms. The parameters α, and $\Delta\lambda_e$ are given in [21]. For typical densities in PSI-2 ($n_e = 10^{19}$ m^{-3}) the Stark broadening is in the range 0.01 pm ($\delta v_{Stark} \approx 5$ m/s) and thus can be neglected completely.

Chapter 4

The plasma-wall transition: measurements and modeling

4.1 Derivation of the basic equations

The particle velocities in most laboratory plasmas are moderate with respect to the speed of light. Furthermore the mean distance between neighboring particles is orders of magnitude larger than their de-Broglie wavelength. The dynamics of a plasma can thus be described with sufficient accuracy in terms of Newton's mechanics. The challenge, however, is due to the complexity of the interactions and the different temporal and spatial scales involved. As it is hopeless to resolve the equations of motion of all the particles ($10^{16} - 10^{21}$) simultaneously, velocity distribution functions $f_\alpha(\vec{x}, \vec{v}, t)$, *i.e.* densities in the phase space, are introduced. Along a trajectory (of a particle following the fields) this density can only change due to collisions:

$$\frac{df_\alpha}{dt} = \frac{\partial f_\alpha}{\partial t} + \frac{d\vec{x}}{dt}\frac{\partial f_\alpha}{\partial \vec{x}} + \frac{d\vec{v}}{dt}\frac{\partial f_\alpha}{\partial \vec{v}} = \left(\frac{\partial f_\alpha}{\partial t}\right)_{coll.} , \tag{4.1}$$

where $d\vec{x}/dt = \vec{v}$ and where $d\vec{v}/dt$ is given by the force on a particle $q_\alpha/m_\alpha \left(\vec{E} + \vec{v}_\alpha \times \vec{B}\right)$. α=(n,e,i) here stands for the particle species, *i.e.* neutral particles, electrons, and singly or multiply ionized atoms.
Although methods like LIF are capable of measuring the velocity distribution function (of atoms if they are not completely ionized) the solution of such a kinetic six-dimensional partial differential equation (particularly when aiming to treat the fields self-consistently and when taking into account the collision operator $(\partial f_\alpha/\partial t)_{coll.}$) is only possible in particular cases. It is thus useful to compute moments $\Psi_m(\vec{x})$ from the velocity distribution function

$$\Psi_m(\vec{x}) = \int_{-\infty}^{\infty} \vec{v}^m f_\alpha(\vec{x}, \vec{v}) d^3v \tag{4.2}$$

which depend only on the spatial coordinate $\vec{x}$. Integrating both sides of Eq. 4.1 over the velocity space after multiplying with increasing powers of $\vec{v}$ a set of hydrodynamic equations is deduced:
Particle balance (Continuity)

$$\frac{\partial n_\alpha}{\partial t} + \nabla \cdot (n_\alpha \vec{u}_\alpha) = S_\alpha \tag{4.3}$$

Momentum balance

$$m_\alpha n_\alpha \left[\frac{\partial \vec{u}_\alpha}{\partial t} + (\vec{u}_\alpha \cdot \nabla) \vec{u}_\alpha \right] = q_\alpha n_\alpha \left(\vec{E} + \vec{u}_\alpha \times \vec{B} \right) - \nabla \cdot \mathbf{p}_\alpha - m_\alpha \vec{u}_\alpha \left(S_\alpha + n_\alpha \nu_{c,\alpha} \right), \tag{4.4}$$

Energy balance

$$\frac{3}{2} n_\alpha \frac{dT_\alpha}{dt} + (\mathbf{p}_\alpha \cdot \nabla) \cdot \vec{u}_\alpha + \nabla \cdot \vec{q}_\alpha = Q_\alpha \ , \tag{4.5}$$

where the symbols have the following meaning:

n_α	:	particle density
$\vec{u}_\alpha$	:	streaming velocity
S_α	:	particle sources
m_α	:	particle mass
q_α	:	particle charge
$\vec{E}$	:	electric field
$\vec{B}$	:	magnetic flux density
$\mathbf{p}_\alpha = p_\alpha \mathbf{I} + \Pi_\alpha$	:	pressure tensor
$\nu_{c,\alpha}$	:	collision frequency
T_α	:	temperature (in energy units)[1]
$\vec{q}_\alpha$	:	heat flux
Q_α	:	heat transfer / energy exchange rate

In order to achieve a completely equivalent description of Eq. 4.1 the list of fluid equations would have to be infinite. Furthermore the m^{th} equation contains the $(m+1)^{th}$ momentum. For this reason we need to close the

[1]Note that it is very common in plasma physics to specify temperatures in eV. This is equivalent of redefining $k_B = 1$. However, this convention is not always useful and sometimes temperatures are given in Kelvin. As the unit indicates unambiguously which convention is chosen here as often in the literature we accept this formal incorrectness.

equations with an additional (*e.g.* thermodynamic) assumption. Instead of the energy equation 4.5 it is common to assume polytropic changes of state, so that

$$T_\alpha n_\alpha^{1-\gamma_\alpha} = \text{const. or equivalently } \nabla p_\alpha = \gamma_\alpha T_\alpha \nabla n_\alpha \ . \tag{4.6}$$

Due to the high heat conductivity the electrons are usually isothermal (γ_e=1). On the other hand for the ions the polytropic index might be in the range $\gamma_i = 1 \ldots 3$.
Besides these fluid equations, Maxwell's equations

$$\text{div}\vec{E} = -\Delta\Phi = \frac{\rho}{\epsilon_0} = \frac{1}{\epsilon_0}\sum_\alpha q_\alpha n_\alpha \qquad \text{(Poisson's equation)} \tag{4.7}$$

$$\text{rot}\vec{E} = -\frac{d\vec{B}}{dt} \qquad \text{(Faraday's law)} \tag{4.8}$$

$$\text{rot}\vec{B} = \mu_0\vec{j} + \mu_0\epsilon_0\frac{\partial\vec{E}}{\partial t} \qquad \text{(Ampère's law)} \tag{4.9}$$

$$\text{div}\vec{B} = 0 \tag{4.10}$$

certainly must hold.
The complete set of Eqs. 4.3-4.5 and Eqs. 4.7-4.10 can only be solved analytically if significant simplifications are made. However, these or similar are often solved by numerical codes like 'B2' developed by Bastiaan Braams in his PhD thesis [7]. Often Monte Carlo codes like 'Eirene' are added in order to simulate the distribution of neutral particles. Such a simulation was carried out by Kastelewicz and Fussmann for PSI-2 [29]. Most of these codes are optimized to the more complex geometry of a Tokamak, which is certainly of great interest for fusion research. More details can be found for example in the PhD thesis of David Coster [12].
A very common approximation is to neglect the electron's mass which is at least 1836 times smaller than that of the ions. For $\vec{B} = 0$ and with $\vec{E} = -\nabla\Phi$ Eq. 4.4 simplyfies to

$$0 = \nabla\left(\frac{e\Phi}{T_e} - \ln n_e\right) \tag{4.11}$$

which is equivalent to Boltzmann's relation

$$n_e(\Phi) = \overline{n}_e \exp\left(\frac{e\Phi}{T_e}\right) \ . \tag{4.12}$$

It is also a well known fact that, due to the high mobility of the electrons, a plasma is able to screen any perturbation in the electric potential within a

few Debye lengths

$$\lambda_D = \sqrt{\frac{\epsilon_0 T_e}{e^2 n_e}} \ . \tag{4.13}$$

This is verified immediately when writing Eq. 4.7 in spherical coordinates with a point charge Q being located at the point of origin

$$\Delta\Phi = \frac{1}{r}\frac{d}{dr}\left(r^2\frac{d\Phi}{dr}\right) = -\frac{1}{\epsilon_0}\left(Q\delta(r) - \sum_\alpha q_\alpha n_\alpha\right) \ . \tag{4.14}$$

Assuming quasi neutrality

$$0 = \sum_\alpha q_\alpha \overline{n}_\alpha \tag{4.15}$$

is satisfied in the average and that we can linearize Eq. 4.12 as $n_e(\Phi) \approx \overline{n_e}(1 + \frac{e\Phi}{T_e})$ Eq. 4.14 is solved by the Debye potential

$$\Phi(r) = \frac{Q}{4\pi\epsilon_0}\frac{e^{-r/\lambda_D}}{r} \ . \tag{4.16}$$

For typical plasmas in PSI-2 this quantity is of the order 10 μm. For volumes much larger than λ_D^3, quasi neutrality is fulfilled very well (for the sake of simplicity we will write n_α instead of $\overline{n}_\alpha$). It should be noted, however, that the assumption of quasi neutrality does *not* mean that the electric fields vanish. A tiny violation of Eq. 4.15 can already cause extreme fields. In particular, when there are gradients in the ion density electric fields are needed to attach the electrons to the ions.
In the presence of magnetic fields charged particles are constrained to a gyromotion around the field lines. If the gyro frequency is much larger than the collision frequency (*i.e.* if we are concerned with a 'magnetized plasma') the plasma can move freely along the field lines. Perpendicular to the field lines, however, the transport is strongly reduced and can only take place by means of diffusion. We write Eq. 4.3 in cylindrical coordinates and assume the cross field diffusion $\Gamma_\perp = -D_\perp \nabla_\perp$

$$D_\perp \frac{1}{rn}\frac{\partial}{\partial r} r \frac{\partial n}{\partial r} + \nu_i = \frac{1}{n}\frac{\partial}{\partial z}(nu) =: \mu \ , \tag{4.17}$$

where quasi-neutrality $n = n_e = n_i$ and ambipolarity $\Gamma_i = \Gamma_e$, *i.e.* equal streaming velocities $u = u_i = u_e$ were assumed. Defining

$$-k_\perp^2 \equiv \frac{1}{rn}\frac{\partial}{\partial r} r \frac{\partial n}{\partial r} \tag{4.18}$$

we are able to reduce Eqs. 4.3-4.4 to a set of one dimensional equations

$$\frac{\partial}{\partial z}(nu) = \mu n = (\nu_i - k_\perp^2 D_\perp)n \tag{4.19}$$

$$0 = -\frac{\partial p_e}{\partial z} - enE_z \tag{4.20}$$

$$m_i nu\frac{\partial u}{\partial z} = -\frac{\partial p_i}{\partial z} + enE_z - m_i nu(\nu_i + \nu_{cx} + \nu_{el}) \ , \tag{4.21}$$

where the electron mass is neglected with respect to that of the ions. $k_\perp$ can be computed from a given density profile $n_e(r)$. A common technique to measure these profiles in PSI-2 are Langmuir probes. The ionization frequency $\nu_i = n_n R_i(T_e)$ is computed from the neutral particle density and from the electron temperature. $\nu_{cx} = n_n R_{cx}(T_i) \approx \sigma_{cx} n_n \sqrt{2T_i/m_i}$ and $\nu_{el} = n_n R_{el}(T_i) \approx \sigma_{el} n_n \sqrt{2T_i/m_i}$ are the frequencies for charge exchange and elastic collisions, respectively. Fig. 4.1 shows the rate coefficients for ionization R_i and for charge exchange R_{cx} as given by different authors. In the range $T_e = 1 \ldots 10$ eV the values for R_i given in the literature agree very well. We choose that given by [40, 59]:

$$R_i(T_e) = \sqrt{\frac{8}{\pi m_e T_e^3}} \int_{E_{iz}}^{\infty} \sigma_i(E) E \exp\left(-\frac{E}{T_e}\right) dE \qquad \text{with} \tag{4.22}$$

$$\sigma_i(E) = \frac{\pi e^2}{4}\left(\frac{e}{4\pi\epsilon_0}\right)^2 \frac{1}{E}\left(\frac{5}{3E_{iz}} - \frac{1}{E} - \frac{2E_{iz}}{3E^2}\right) 6 \text{ and } E_{iz} = 15.76\,\text{eV}. \tag{4.23}$$

On the other hand the rate coefficients for charge exchange and elastic collisions are far less reliable, the given values differing by almost one order of magnitude. Since the cross sections found experimentally by Pullins *et al.* [52] are in good agreement with theoretically computed ones and as this reference is the most recent we adopt these values ($\sigma_{cx}(1\text{ eV}) = 62.8 \times 10^{-20}\ \text{m}^{-2}$). For elastic collisions we assume $\nu_{el} = 0.36\nu_{cx}$ as this was already done in [50].

We now consider the situation when a magnetized plasma hits the surface of a limiting wall or any solid obstacle with a size significantly larger than λ_D. At surfaces ions and electrons recombine very efficiently so that walls constitute a strong sink for the plasma. When electron and ion temperatures are similar, the electrons, due to their much smaller mass, have a much higher thermal speed $v_{th,e} = \sqrt{2T_e/m_e}$. If there were no further constraints, the electron flux to the surface would be significantly higher than that of the ions. As the plasma loses charge, electric fields soon build up, which slow down the electrons and accelerate the ions. In the stationary situation (which is usually attained on the sub-nanosecond timescale) an electrostatic

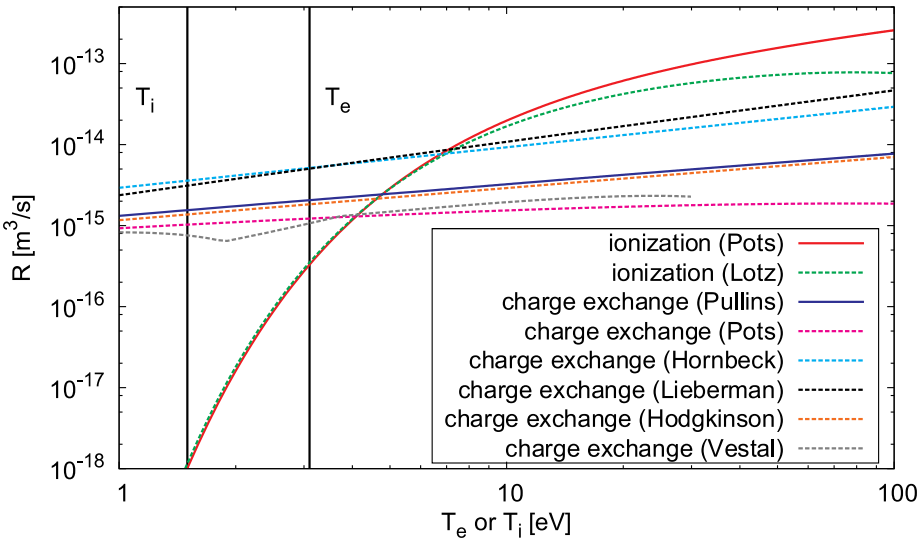

Figure 4.1: Rate coefficients for ionization and for charge exchange according to different authors: Pots[50], Lotz[41], Pullins[52], Hornbeck[26], Lieberman[40], Hodgkinson[25] and Vestal[65]

potential is formed close to the surface as illustrated in Fig. 4.2. Electron and ion fluxes must then be equal ($\Gamma_e = \Gamma_i$), so that no net current streams onto the target. The space charge region in front of the surface is called 'electrostatic sheath' or just 'sheath' and has an extension of a few Debye lenghts. Leaving the sheath at some point quasi neutrality will be fulfilled to a high extent (but as we will see below not accurately). Although the position of this point is not clearly defined, we will refer to this as the 'sheath edge' (s.e.) in the following. At the sheath edge we can expand the space charge density ρ in terms of the electric potential Φ:

$$\rho(\Phi) = \rho_{se} + (\Phi - \Phi_{se}) \left.\frac{d\rho}{d\Phi}\right|_{se} + \dots \,, \tag{4.24}$$

where $\rho_{se} = 0$ holds as presupposed. Inserting Eq. 4.24 into Poisson's Equation 4.7, multiplying with the field strength $E = -d\Phi/dz$, and integrating over z leads to

$$\epsilon_0 E^2 + (\Phi - \Phi_{se})^2 \left.\frac{d\rho}{d\Phi}\right|_{se} = 0. \tag{4.25}$$

As E^2 and $(\Phi - \Phi_{se})^2$ are positive,

$$\left.\frac{d\rho}{d\Phi}\right|_{se} = e \left.\frac{d(n_i - n_e)}{d\Phi}\right|_{se} \leq 0 \tag{4.26}$$

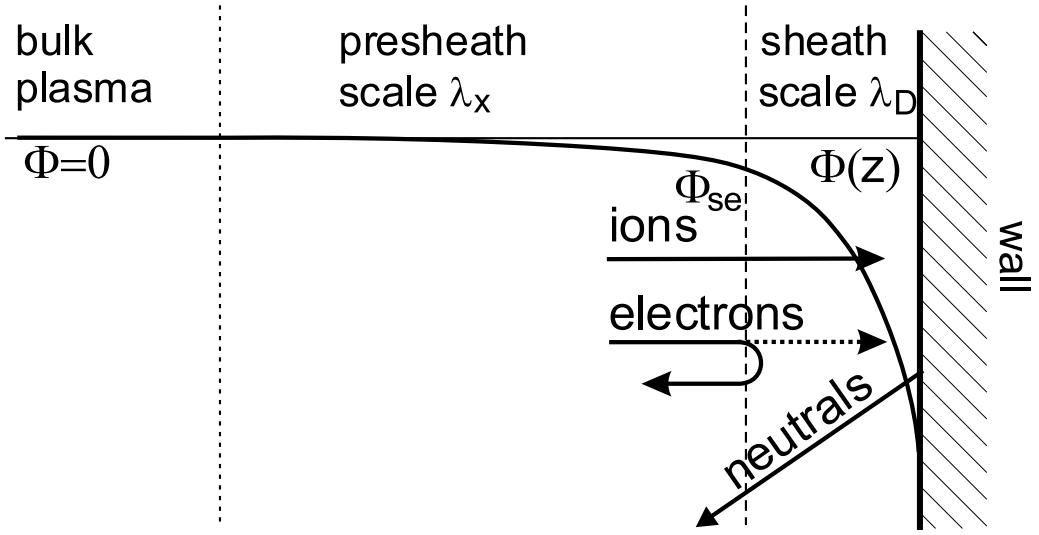

Figure 4.2: Illustration of sheath and presheath forming in front of a limiting wall or another solid obstacle in a plasma.

must hold (cf. [54]).
This condition confirms theoretically the intuitive expectation that the electron density decreases faster than the ion density when approaching the wall (*i.e.* with dropping electric potential, $d\Phi < 0$). If this was not the case n_i and n_e would not be monotonic. Such a potential could not be stable since particles would be trapped in a potential minimum.
Inserting Eq. 4.19, into Eq. 4.20 and Eq. 4.21, with $\nu_i = \nu_{cx} = \nu_{el} = \mu = 0$ and Eq. 4.6, and multiplying by $dz/d\Phi$ leads to

$$\frac{dn_e}{d\Phi} = \frac{en_e}{T_e} \quad \text{and} \quad \frac{dn_i}{d\Phi} = \frac{en_i}{m_i u_i^2 - \gamma_i T_i}. \tag{4.27}$$

This in turn is inserted in Eq. 4.26 so that we obtain the Bohm criterion Bohm [3] aforementioned

$$u_i|_{\text{s.e.}} \geq \sqrt{\frac{T_e + \gamma_i T_i}{m_i}}\Bigg|_{\text{s.e.}} . \tag{4.28}$$

Introducing the speed of sound

$$c_s = \sqrt{\frac{T_e + \gamma_i T_i}{m_i}} . \tag{4.29}$$

and defining the Mach number as the streaming velocity over the speed of sound $M = u_i/c_s$ this also reads

$$M|_{\text{s.e.}} \geq 1 . \tag{4.30}$$

A generalization for a plasma composed of multiple (positive) ion species was given by Riemann in [54]. With the general definition of quasi neutrality (Eq. 4.15) Eqs. 4.26-4.27 yield

$$\sum_i \frac{q_i n_i}{m_i u_i^2 - \gamma_i T_i} \leq \frac{e^2 n_e}{T_e} \tag{4.31}$$

at the sheath edge. The index i here refers to the different ion species.
We can understand the ion velocity distribution $f_i(v_i)$ as a number of groups of ions with the same velocity v_i and a vanishing temperature $T_i = 0$ but with the same charge $q_i = e$. Substituting the summation by an integral, we obtain the so called kinetic (or general) Bohm criterion (cf. [54])

$$\int_0^\infty \frac{f_i(v_i)}{v_i^2} dv_i \leq \frac{m_i}{T_e} \tag{4.32}$$

which was found originally by Harrison and Thompson [24].
However, in the following we will assume the fluid approach sufficiently accurate and refer to Eq. 4.30 as the Bohm criterion. It says that a stationary sheath can only exist if the ions arrive at the sheath edge at least with the speed of sound. According to Bohm this acceleration is accomplished within the so called 'presheath', a transition zone between the bulk plasma and the sheath, where quasi neutrality is fulfilled to a high degree (although a weak electric field persists). The extension of the presheath is much larger than that of the sheath.
It should be noted that the physics of the presheath is far more complex than that of the sheath since processes like ionization, collisions, and variations and orientation of the magnetic field have to be taken into account. The sheath in contrast is small enough that these processes can be neglected. With $\mu = k_\perp = \nu_i = \nu_i = \nu_i = \partial p_i / \partial z = 0$ we obtain Boltzmann's relation

$$n_e(\Phi) = n_{se} \exp\left(\frac{e(\Phi - \Phi_{se})}{T_e}\right) \tag{4.33}$$

for the electrons ($m_e \approx 0$) and we can describe the density of the ions by

$$n_i(\Phi) = n_{se}\left(1 - \frac{2e(\Phi - \Phi_{se})}{m_i c_s^2}\right)^{-1/2} , \tag{4.34}$$

which represents the conservation of energy. The Bohm criterion, Eq. 4.30, was assumed here. We can then compute the devolution of the densities and the potential in the sheath from Poisson's equation 4.7

$$\frac{d^2\Phi}{dz^2} = -\frac{e n_{se}}{\epsilon_0}\left[\left(1 - \frac{2e(\Phi - \Phi_{se})}{m_i c_s^2}\right)^{-1/2} - \exp\left(\frac{e(\Phi - \Phi_{se})}{T_e}\right)\right] . \tag{4.35}$$

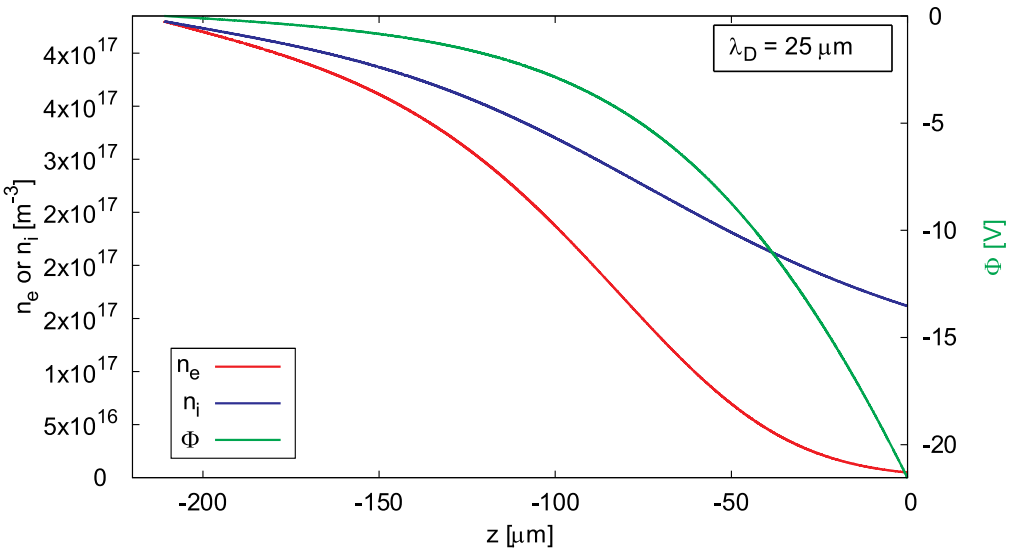

Figure 4.3: Potential drop in front of a solid surface for an exemplary density of $n_{se} = 4 \times 10^{17}$ m^{-3} and a temperature $T_e = 4.8$ eV.

An approximate analytic solution of this equation, good for ratios $|e\Phi_w/T_e| > 10$, was found by Sheridan and Goree [58]. However, as the numerical solution of a one-dimensional differential equation is trivial, Fig. 4.3 shows the numerical integration of Eq. 4.35.
It is then also possible to give the current density at any position $z(\Phi)$ in the sheath

$$j(\Phi) = en_{se}c_s - en_{se} \exp\left(\frac{e(\Phi - \Phi_{se})}{T_e}\right) \frac{\overline{c}_e}{4} \tag{4.36}$$

The first term of this equation is the ion flux, which is conserved within the whole sheath and therefore equal to that at the sheath edge. $\overline{c}_e = \sqrt{8T_e/(\pi m_e)}$ is the mean velocity of the electrons (cf. [62]) of the electrons, which are assumed to be in thermal equilibrium within the whole sheath.
When introducing an electrode with a variable biasing to the plasma (*e.g.* the tip of a Langmuir probe), the electrons in its vicinity screen this potential perturbation from the rest of the plasma. Varying the biasing then changes the size of the sheath but not the potential at the sheath edge. The current drawn from the collector (in agreement with the convention the current flowing into a Langmuir probe is counted negative $I_L(U) = -A_{tip}j(U)$, where A_{tip} is the tip area) is then given by Eq. 4.36. When the electrode is at the floating potential

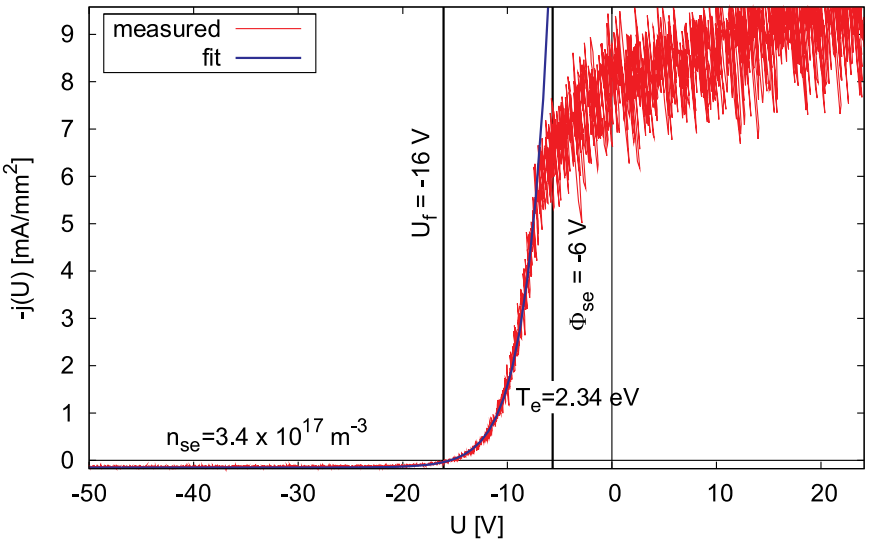

Figure 4.4: Typical current-voltage characteristics measured in a PSI-2 discharge. The electron temperature is obtained from the slope of the curve around the floating potential U_f. n_{se} can be derived from the ion saturation current at the left wing of the curve. The sheath edge potential Φ_{se} is determined by means of Eq. 4.37.

$$U_f = \frac{T_e}{2e} \ln\left[2\pi \frac{m_e}{m_i}\left(1 + \frac{\gamma_i T_i}{T_e}\right)\right] + \Phi_{se} \ , \tag{4.37}$$

no net current $j(U_f) = 0$ is drawn from the plasma.
Since U_f depends only weakly on the temperature ratio T_i/T_e, one might think that this relation would enable us to determine the electron temperature from the voltage measured at any electrically floating object exposed to the plasma. Since the potential at the sheath edge plasma Φ_{se} with respect to ground, is not known from this measurement, it is necessary to acquire an entire current voltage characteristics (Eq. 4.36) by means of a Langmuir probe. When biasing with a high negative voltage the second term in Eq. 4.36 vanishes and we can furthermore determine the electron density from the ion saturation current

$$I_{sat} = -A_{tip} n_{se} e c_s \ , \tag{4.38}$$

an important plasma parameter. Fig. 4.4 shows such a typical characteristics measured with the probe described in Sec. 2.3.
So far we have only treated the case where the biasing voltage is (significantly) smaller than the sheath edge potential. Exceeding this voltage high

currents can be drawn from the plasma, however, saturation also occurs the ions this time being the particle species that screen the electrode.
The theory of Langmuir probes is an open field of research and the theoretical description can become far more complex, when treating kinetic effects, when taking into account the finite gyro radius of the ions, when being concerned with particular probe head geometries or with non-Maxwellian electron velocity distributions. For further details the reader is referred for example to the review article written by Demidov [13] and the references therein.

4.2 The presheath of a large target

4.2.1 Modeling

In order to find analytical functions that describe the plasma in the presheath of a large target we want to simplify Eqs. 4.19-4.21 further. First, we assume electrons and ions to be isothermal so that $\partial p_{e,i}/\partial z = T_{e,i}\partial n_{e,i}/\partial z$. We then add Eq. 4.20 and Eq. 4.21, assume $n = n_e = n_i$, replace $\partial n/\partial z$ by means of Eq. 4.19, multiply by $u/(nm_ic_s^3)$, with definition 4.29, and the definition of the Mach number $M = u/c_s$ to obtain the relation

$$\frac{\partial M}{\partial z} = \frac{\mu}{c_s}\frac{1+\alpha M^2}{1-M^2} \text{ , where } \alpha = \frac{\nu_t}{\mu} \ . \tag{4.39}$$

$\nu_t = \nu_i + \nu_{cx} + \nu_{el}$ is the total collision frequency.
The density $n(M)$ as a function of the Mach number can be obtained from Eq. 4.19, determining $\partial n/\partial z$ and then dividing this expression by $n\partial M/\partial z$. Both sides of the equation obtained can be expressed by logarithmic derivatives, so that we find

$$n(M) = n_0 \left(1+\alpha M^2\right)^{-\frac{\alpha+1}{2\alpha}} \ , \tag{4.40}$$

where n_0 is the density in the bulk plasma. Knowing the density as a function of M we can directly determine $\Phi(M)$ from Eq. 4.20, which is a different way of writing the Boltzmann relation,

$$\Phi(M) = -\frac{T_e}{2e}\frac{\alpha+1}{\alpha}\ln(1+\alpha M^2) \ . \tag{4.41}$$

Note that the ions are accelerated by both, the electric field (enE_z) and the pressure gradient $\partial p_i/\partial z$ in Eq. 4.21; the ratio of these forces is simply given by the temperature ratio $T_e/T_i \approx 2$.
Assuming a constant neutral gas density n_n, *i.e.* constant values α and μ, we can integrate Eq. 4.39 in order to obtain an expression for $z(M)$

$$z(M) = \frac{c_s}{\nu_t}\left(\frac{1+\alpha}{\sqrt{\alpha}}\arctan\left(\sqrt{\alpha}M\right) - M\right) - z_0 \ . \tag{4.42}$$

z_0 is chosen such that the Bohm criterion (Eq. 4.28) $z(M=1) = 0$ is satisfied at the target surface. We will also refer to this equation as the 'collisional-diffusive model'.
We have so far disregarded the fact that the target surface, a sink for electrons and ions, is a strong source of neutral particles. A treatment of the

problem taking into account all the mechanisms involved is only possible by resolving the equations numerically. Another analytic solution of Eq. 4.39 can be found, however, if we neglect radial diffusion, charge exchange, and elastic collisions (so that $\mu = \nu_i$ and $\alpha = 1$). If the target was infinitely extended in y and x directions no particles could escape from the plasma and that the total flux density

$$n_n u_n + n c_s M = 0 \tag{4.43}$$

vanishes. Assuming furthermore a constant neutral particle velocity u_n, we can then express n_n by nM and using $\mu = \nu_i = R_i n M c_s / u_n$, Eq. 4.40, and the definition of the mean free path length for ionization

$$\lambda_i = u_n / (R_i n_0) \tag{4.44}$$

we can solve Eq. 4.39

$$z(M) = -\frac{\lambda_i}{2}\left(M^2 - 1 - 2\ln(M)\right) \ . \tag{4.45}$$

Note that the Mach number falls to a value of $1/e$ at a distance of $|z(1/e)| = 0.57\lambda_n$ to the target. The validity of this approach can be justified if λ_n is much smaller than the target (and λ_{cx} and λ_{el}). This solution will also be referred to as the 'recycling model'.

4.2.2 Measurements

Measured ivdfs at different z positions to a large target are shown in Fig. 4.5. The spatial resolution in z-Direction was $\Delta z = 0.4$ mm. (This is an improvement by a factor of 100 with respect to [42, 44]!) In order to compensate vignetting effects some of the curves were multiplied by the factors shown in parenthesis in the legend. For the sake of comparability the ivdf measured when the target was removed from the plasma is shown reduced by a factor of 5. Two different target materials were used, boron nitride (Fig. 4.5(a)) and tungsten (Fig. 4.5(b)).
The black vertical lines indicate the speed of sound evaluated from the current-voltage-characteristics measured by the collector in the center of the target and from the ion temperature obtained from the LIF measurement without target. Different values for the polytropic index were assumed: $\gamma = 1$ (isothermal ions) and $\gamma = 3$ (adiabatic ions). Formally setting $\gamma = 0$ corresponds to the case, where the ions are cold. In contrast to Sec. 4.6 the ivdfs found can be fitted very well by shifted Maxwellian distributions, their

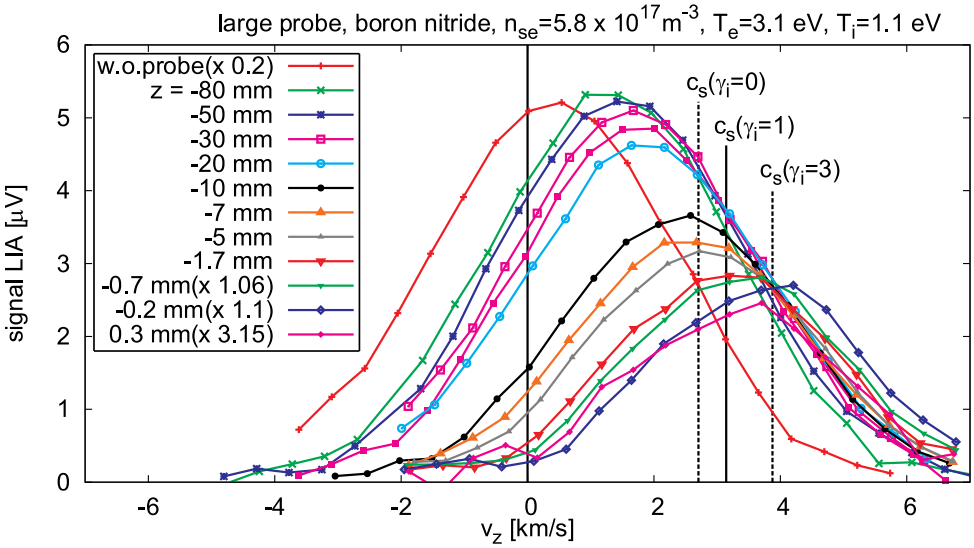

(a) Target material: boron nitride

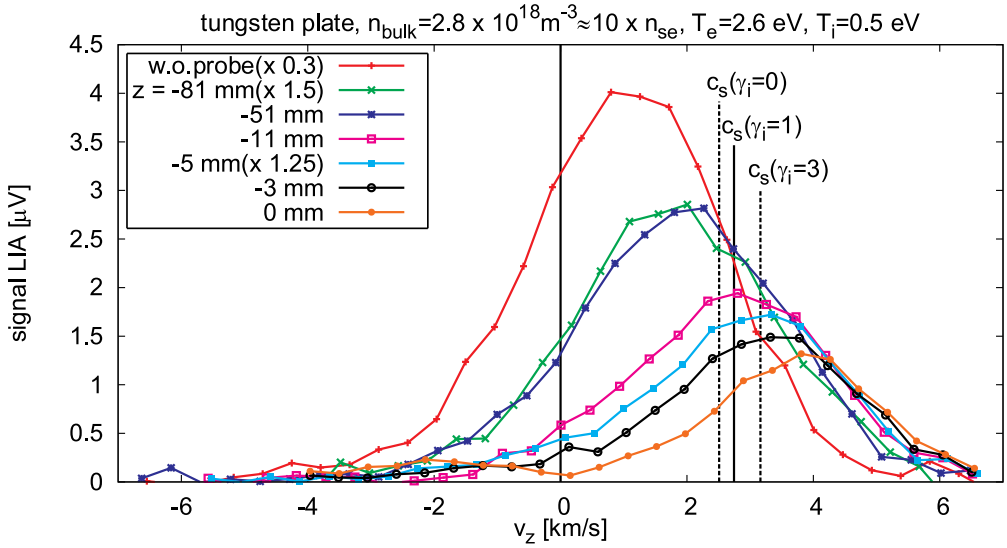

(b) Target material: tungsten

Figure 4.5: Ion velocity distributions measured at different distances $|z|$ to a target made of (a) boron nitride or (b) tungsten. The spatial resolution was $\Delta z = 0.4$ mm. In (b) the density could not be measured directly at the target surface; here the value measured by the Langmuir probe is given instead.

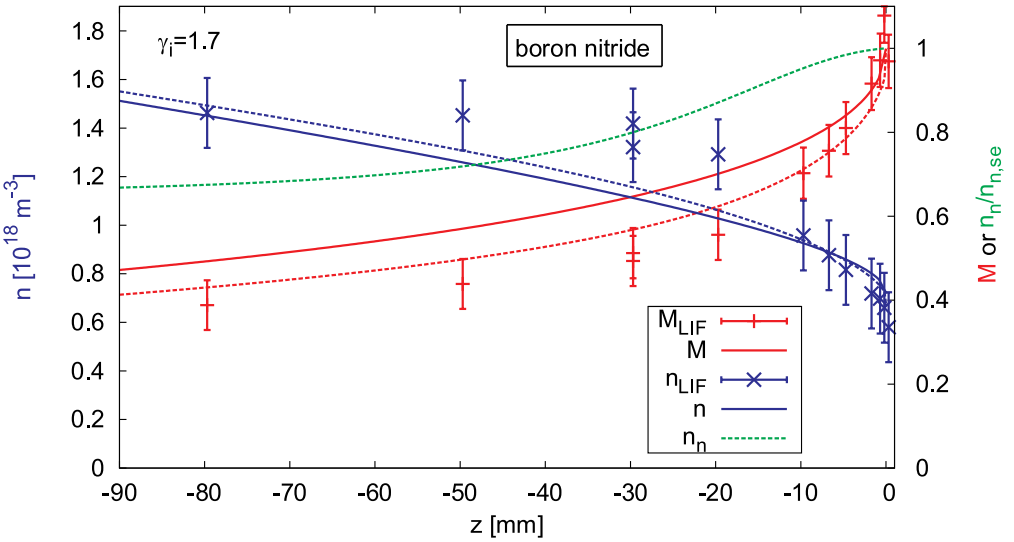

(a) Axial profiles of Mach number and density evaluated from the ivdfs shown in Fig. 4.5(a). The boron nitride target is located at $z = 0$. The solid lines show the modeling according to Eq. 4.42 and Eq. 4.40 with the parameters given in Tab. 4.1. A small improvement is achieved applying a numerical modeling (dashed lines).

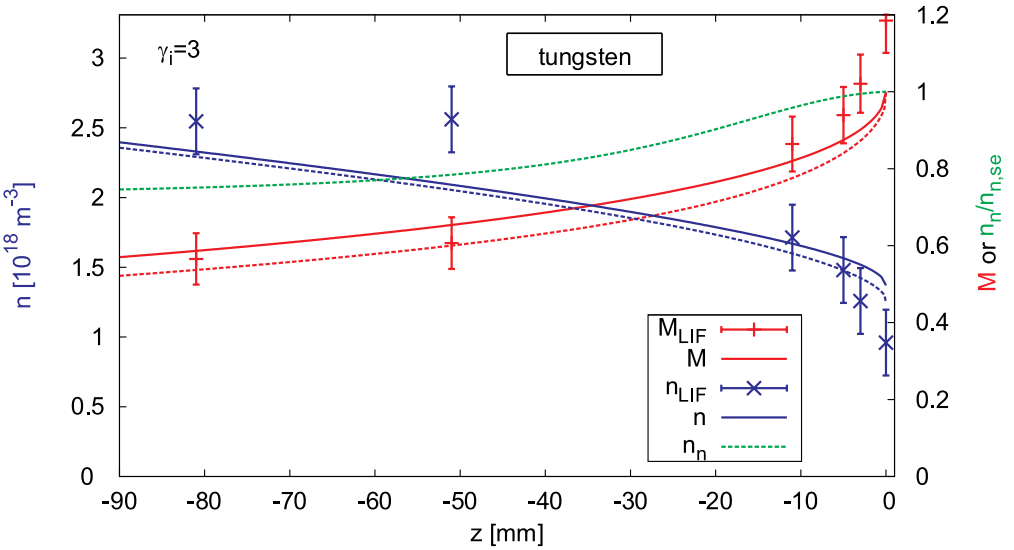

(b) As Fig. 4.6(a) but for the ivdfs measured in front of a tungsten target (Fig. 4.5(b)).

Figure 4.6: Evaluated Mach numbers and densities in front of a large target.

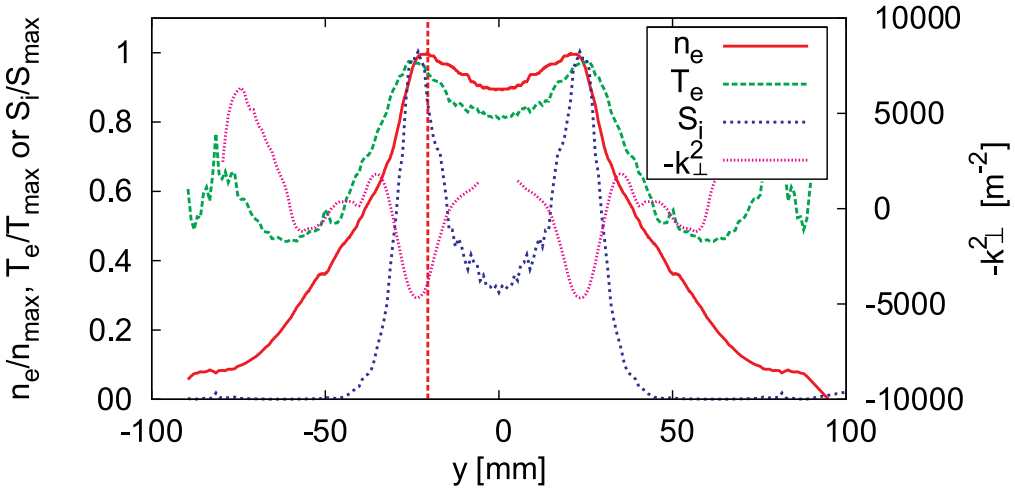

(a) n_e and T_e profiles in front of the boron nitride target. The quantities are normalized to their peak values $n_{max} = 4.3 \times 10^{18}$ m^{-3}, $T_{max} = 3.1$ eV and $S_{max} = 1.7 \times 10^{22}$ m^{-3} s^{-1}.

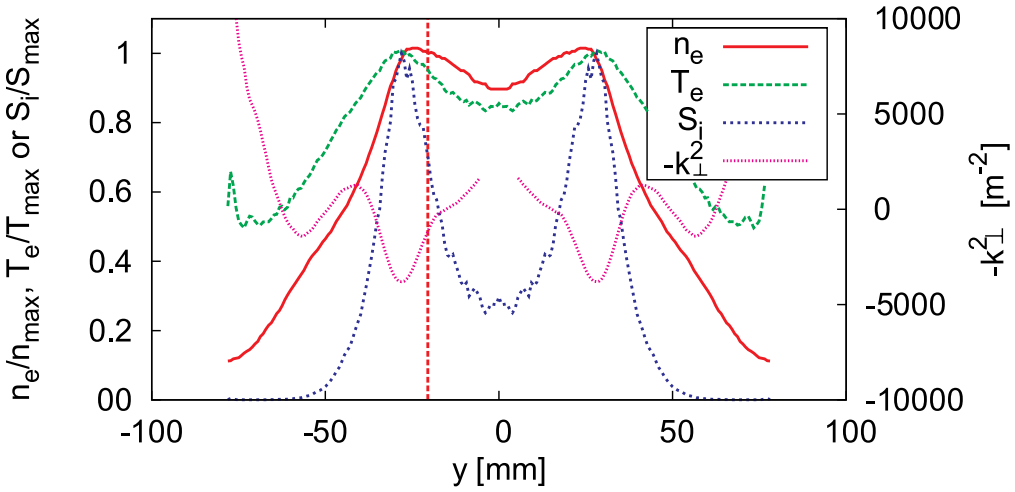

(b) n_e and T_e profiles in front of the tungsten target. The quantities are normalized to their peak values $n_{max} = 3.4 \times 10^{18}$ m^{-3}, $T_{max} = 2.6$ eV and $S_{max} = 3.7 \times 10^{21}$ m^{-3} s^{-1}.

Figure 4.7: Radial profiles. S_i represents source strength due to electron-impact ionization. $k_\perp$, a measure for the curvature of the radial density profile, is defined by Eq. 4.18)

shift increasing up to at least the speed of sound when approaching the target surface. A first important result is this experimental proof of the Bohm criterion [3].
By fitting Maxwellian distributions to ion velocity distribution functions (ivdfs) in Fig. 4.5 we obtain the data points for n and M shown in Fig. 4.6. For both, boron nitride and tungsten, the typical length λ_M, where the final acceleration from Mach numbers around 0.5 to $M = 1$ takes place, is as short as $\lambda_M = 30$ mm.
Computing λ_i for neutral atoms being released at thermal velocity according to Eq. 4.44, we obtain values at least as large as $\lambda_i = 63$ cm (for $T_n = 300$ K). For this reason we expect the collisional-diffusive model (Eq. 4.42) to describe the n and M profiles much better than the recycling model (Eq. 4.45). In order to compare these profiles to the model we have to analyze the radial n_e and T_e profiles shown in Fig. 4.7. Applying the differential operator on the right hand side of Eq. 4.18 we can determine the value for $k_\perp$. The T_e and n_e values are evaluated from the collector in the center of the probe. With the parameters listed in Tab. 4.1 the solid curves in Fig. 4.6 are drawn. The agreement with the experimental data is already quite good.

measured quantities					
target material	n_{se} [m^{-3}]	T_e [eV]	T_i [eV]	p_n [mPa]	$k_\perp$ [m^{-1}]
boron nitride	5.8×10^{17}	3.1	1.1	50	63.2
tungsten	9.7×10^{17}	2.63	0.5	59	35.1
adapted quantities					
target material	T_n [K]	D [m^2/s]			
boron nitride	380	1			
tungsten	600	1			
related quantities					
target material	n_n [m^{-3}]	ν_i [kHz]	ν_{cx} [kHz]	ν_{el} [kHz]	α
boron nitride	9.5×10^{18}	4.1	13	4.7	83
tungsten	7.2×10^{18}	1.3	7.3	2.6	207

Table 4.1: Modeling parameters for the collisional-diffusive model (Eq. 4.42).

For reasons that are not quite clear up to now the radial density profile changes when immersing the tungsten target in the plasma. For this reason the $k_\perp$ values for the two different targets differ significantly at the laser position (indicated by the red vertical lines in Fig. 4.7(a) and Fig. 4.7(b)).
Since the LIF diagnostic system is optimized for a high resolution and since the view into the target chamber is limited, the z-interval covered by the LIF measurements is relatively small (-80 mm $< z < 0$). However, we can

obtain an approximate experimental value for the density in a distance of about $z = -800$ mm simply by removing the target from the plasma. In this case the plasma streams onto the neutralizer plate, which is as if the target was shifted by +800 cm. The strong density increase by a factor of more than 6 over this interval is even more pronounced in the experiment.

4.2.3 Numerical modeling

So far we have been unable to find an analytic solution for Eq. 4.39, which takes into account all the processes involved: ionization, friction, diffusion and recycling of neutral particles. It is not a trivial matter to find such a solution, since we cannot make use of a conservation law like 4.43 and we must compute the neutral particle density at a certain position z taking into account the plasma conditions between z and the wall. However, Eq. 4.39 can be solved numerically by dividing the neutral particles into two fractions $n_n = n_n^{(bg)} + n_n^{(r)}$, those that collided with the walls of the vessel several times and that constitute a constant background density $n_n^{(bg)}$ and those that originate directly from the target plate $n_n^{(r)}$. In the stationary case as many neutrals are released from the target as ions move onto it, and so we have $\Phi_n = -\Phi_i$. As a simplification we assume all the neutrals to start at $z = r = 0$ and that their velocity u_n is constant. Their angular distribution is furthermore assumed to be given by a cosine law

$$\frac{d\Phi_n}{d\Omega} = -\Phi_i \frac{\cos\theta}{\pi} \ , \tag{4.46}$$

where we define the angle θ as illustrated in Fig. 4.8. If no collisions or ionization take place we can compute the flux through the circular cross-sectional area at the position z by

$$\Phi_n(z) = -\Phi_i \int_0^{2\pi} d\phi \int_0^{\theta(z)} d\theta' \sin(\theta') \frac{\cos(\theta')}{\pi} = -\Phi_i \sin^2\theta(z) \ . \tag{4.47}$$

Note that with the target plate placed at $z = 0$, all three quantities z, dz and u_n are negative. Furthermore a negative flux Φ_n means that a (positive) number of particles $dN = \Phi dt = -u_n n \pi a^2 dt$ passes from the right to the left through the surface, where a is the radius of the plasma column. With the angle θ given by $\theta(z) = \arctan\left(a/(-z)\right)$,

$$d\Phi = \frac{d}{dz}\left[\sin^2\left(\arctan\left[a/(-z)\right]\right)\right] dz = -\frac{2z}{a^2 + z^2} dz \tag{4.48}$$

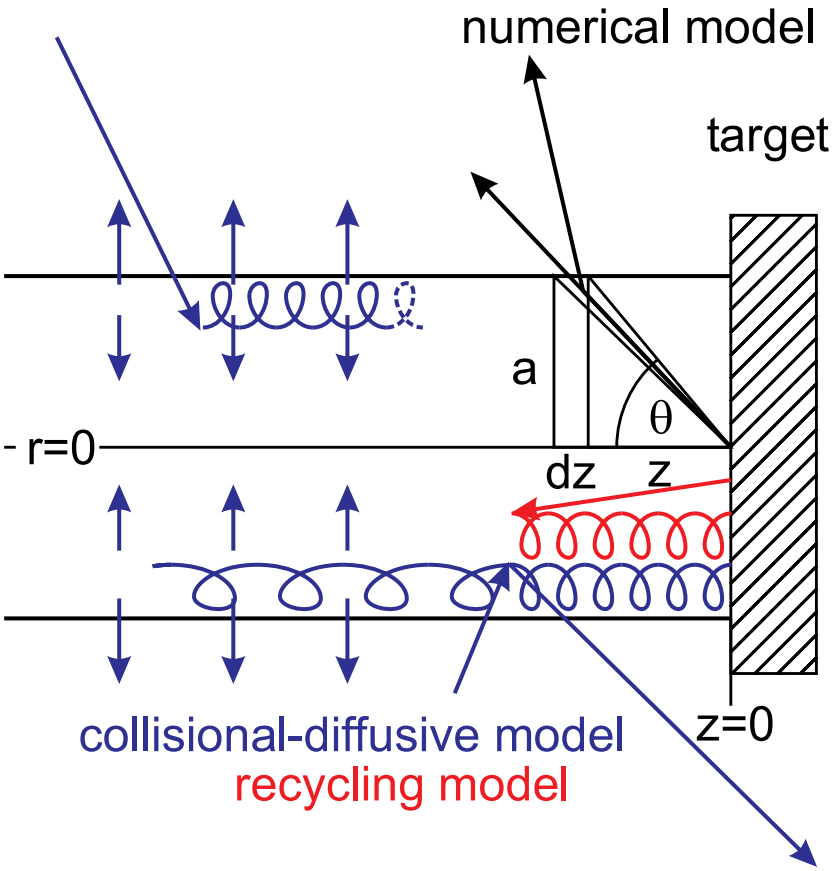

Figure 4.8: Illustration of the different presheath models. The collisional-diffusive model takes into account ionization and charge exchange processes with the background neutral particles and cross-field diffusion of plasma from the high density regions (blue). The recycling model assumes only ionization of the particles originating from the target. The numerical model takes into account all these processes and additionally radial losses of recycled neutrals from the plasma.

particles escape from the plasma column per unit time from the interval $z \ldots z + dz$.
Taking also into account ionization and collision processes[2], the density of

[2]Although a charge exchange reaction does not change the number of neutral particles in first place, here it effectively does since the neutral particle after the reaction has a very high velocity and escapes from the plasma volume almost immediately.

$n_n^{(r)}$ can be described by

$$dn_n^{(r)} = -\left(\frac{R_t}{u_n} n(z) + \frac{2z}{a^2 + z^2}\right) n_n^{(r)}(z) dz \ , \tag{4.49}$$

with the total rate coefficient $R_t = R_i + R_{cx} + R_{el}$. Since $n(z)$ depends itself on $n_n^{(r)}$ we cannot simply integrate this equation but have to solve it (numerically) simultaneously to Eq. 4.39.
As shown by the dashed curves in Fig. 4.6 the numerically computed profiles of Mach number and density are only slightly better than the analytical formula (4.42). However, for increasing electron temperatures this correction will become more and more important up to the point where Eq. 4.45 is expected to describe the profiles well (cf. also Sec. 4.6).

4.2.4 Neutral gas temperature

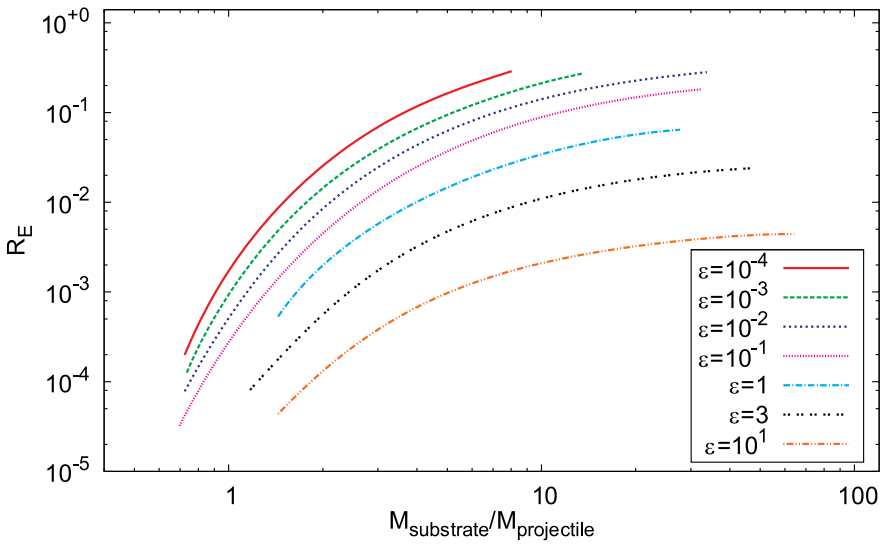

Figure 4.9: Energy reflection coefficient according to Stangeby [62]. The 'reduced energy' ϵ, which for the conditions in PSI-2 is in the range 10^{-4}, is determined by formula 4.50

In view of the high frequency of charge exchange (and elastic collision) processes, which produce neutral particles at energies in the range of some eV, the assumed neutral gas temperatures in Tab. 4.1 seem to be very low. These values can be justified assuming the energy reflection coefficients given by Stangeby [62], which are reproduced in Fig. 4.9. The parameter ϵ stands for

the 'reduced energy'

$$\epsilon \equiv \frac{0.032534 E_0[eV] m_2}{(m_1+m_2) Z_1 Z_2 \sqrt{Z_1^{2/3}+Z_2^{2/3}}} \ , \tag{4.50}$$

where the index 1 refers to the projectile atoms and the index 2 to those of the substrate. m_α determines the atomic masses and Z_α the atomic number. For an atom originating from a charge exchange reaction at the energy $E_{cx} = 1.5$ eV colliding with the vessel made from stainless steel this value is $\epsilon = 1.5 \times 10^{-5}$. Unfortunately, the smallest reduced energy for which energy reflection coefficients are available is $\epsilon = 10^{-4}$ (red curve) and we have to assume a quite large uncertainty for these coefficients. For this ϵ value for argon on stainless steel R_E is as small as $R_E = 1$ %. An atom has to collide $N_{cw} = \ln(E_{cx}/E_{cold}) / \ln R_E \approx 1$ times with the walls in order to be at an energy of $E_{cold} = 1/40$ eV. With a vessel diameter of $d_v = 40$ cm the characteristic time this atom is at that energy is then estimated by

$$\tau_{cx} = N_{cw} d_v / v_{th,i} = 130 \ \mu\text{s} \ . \tag{4.51}$$

The mean period of time an atom remains at a low energy until it participates in a charge exchange reaction on the other hand is

$$\tau_{cold} = \frac{1}{\sigma_{cx} n' v_{th,n}} = 100 \text{ ms} \ , \tag{4.52}$$

i.e. almost three orders of magnitude longer. Here the density averaged over the whole target chamber $n' = n V_{plasma}/V_{vessel}$ was used. As a rough estimation we can give a neutral gas temperature of

$$\frac{\tau_{cx} T_i + \tau_{cold} 300 \text{ K}}{\tau_{cx} + \tau_{cold}} \approx 350 \text{ K} \ . \tag{4.53}$$

For an energy reflection coefficient in the range of ten times larger (10%) this value is a little higher but still remains below 400 K. However, this simple estimation does not take into account the neutrals emitted from the surface. The energy coefficient there depends significantly on the material. While for argon on boron nitride it is significantly smaller than 1%, for argon on tungsten it becomes approximately 15%. This might explain, why we had to assume a significantly larger neutral gas temperature ($T_n = 600$ K) for the modeling with the tungsten target.

4.3 The presheath of a small target

4.3.1 Modeling

The case of a small target immersed in a magnetized plasma was addressed by Hutchinson [27] in 1988 in order to deduce the Mach number from the ratio of ion saturation currents measured on the two sides of a Mach probe. Hutchinson assumes a set of equations similar to Eqs. 4.19-4.21. These are applied to a geometry that corresponds to the present arrangement, *i.e.* a cylindrical target immersed in a magnetized plasma. According to Hutchinson two regions can be distinguished (cf. Fig. 4.14(a)): (I) the region in front of the target where the plasma is accelerated towards the target surface, and (II) a zone beyond the field lines that touch the target edge where the plasma streams unperturbed at a constant Mach number with a constant density. The Mach number and density in region (II) are assumed to be equal to M_∞ and n_∞ in (I), sufficiently far away from the surface. In contrast to Eqs. 4.19-4.21 and in contrast to an alternative model set up by Stangeby [61], Hutchinson also takes into account radial momentum transport by means of the pressure tensor element $p_{z,r} = -\eta \partial u_z/\partial r$, where the viscosity coefficient is taken as

$$\eta = \alpha m_i n_i D \ . \tag{4.54}$$

The parameter $\alpha \in]0,1]$ is left open for the beginning. Neither sources nor collisional friction are considered, processes that were found important in PSI-2 in Sec. 4.2. As the fluid equations are solved numerically anyway, no principle difficulty occurs when we also take these forces into account. We add the terms $\nu_i n_i$ and $(\nu_{cx}+\nu_{el}) m_i n_i v_{||}$ to the first two Eqs. in [27], following in all other respects the author. The equations that have to be integrated then read

$$\frac{d\widetilde{n}}{d\widetilde{z}} = \frac{(1-\widetilde{n})M - (M_\infty - M)[1-\widetilde{n}(1-\alpha)] + (\widetilde{\nu}_i + \widetilde{\nu}_t)\widetilde{n}M}{M^2-1} \tag{4.55}$$

$$\frac{dM}{d\widetilde{z}} = \frac{(M_\infty - M)[1-\widetilde{n}(1-\alpha)]M - (1-\widetilde{n}) - \widetilde{n}\,(\widetilde{\nu}_i + \widetilde{\nu}_t M^2)}{\widetilde{n}(M^2-1)} \tag{4.56}$$

where $\widetilde{n} = n_i/n_\infty$, $\widetilde{\nu}_i = \nu_i a^2/D$ and $\widetilde{\nu}_t = \nu_t a^2/D$ are dimensionless quantities. In order to pass from the dimensionless parameter $\widetilde{z}$ to the real space coordinate we have to multiply the former by $c_s a^2/D$.
By integrating these equations and assuming $\widetilde{\nu}_i = \widetilde{\nu}_t = 0$ for the moment the density at the sheath edge as a function of the unperturbed Mach number is found to be $\widetilde{n}_{se}(M_\infty) = 0.3\exp(1.27 M_\infty)$. As the temperatures and

therefore the speed of sound are constant everywhere the ratio of ion saturation currents on the front and backsides is equal to the densities $I_{s1}/I_{s2} = n_{se}(M_\infty)/n_{se}(-M_\infty)$ and therefore the unperturbed Mach number can be obtained from

$$M_\infty = 0.4 \ln(I_{s1}/I_{s2}) \ . \tag{4.57}$$

4.3.2 Measurements

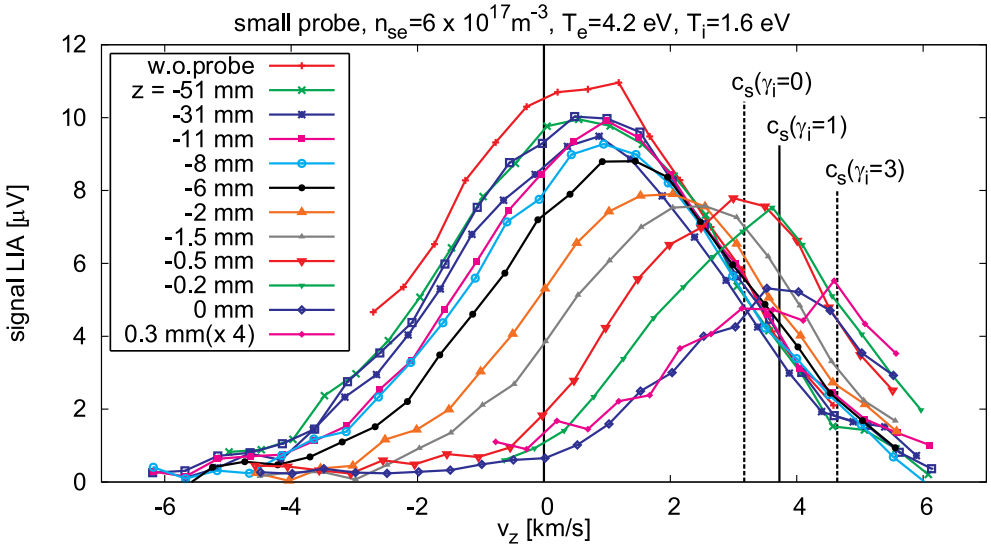

Figure 4.10: Ion velocity distributions measured by means of LIF at several positions in front of the small target. The spatial resolution was $\Delta z = 0.4$ mm.

With the measured ivdfs shown in Fig. 4.10 and the ion saturation currents on both sides of the target $I_{s1} = -10.1$ mA and $I_{s2} = -7.3$ mA, we are now able to compare this model with the experiment. The measured values for M and n (obtained by fitting Maxwellian distribution functions in Fig. 4.10) are plotted in Fig. 4.11 together with their computed values neglecting for the moment collisions ($\tilde{\nu}_i = \tilde{\nu}_t = 0$). For a diffusion coefficient as high as $D = 20$ m^2/s an excellent agreement with the LIF-measurements is obtained. Furthermore, the ratio of the ion saturation currents predicts perfectly the unperturbed Mach number $M_\infty = 0.13$ assumed in Eqs. 4.55 and 4.56. More moderate values around $D = 7$ m^2/s are not incompatible with the error bars, but values around $D = 1.4$ m^2/s (Bohm diffusion) or $D = 1$ m^2/s (assumed in the case of the large target) are clearly inconsistent with the

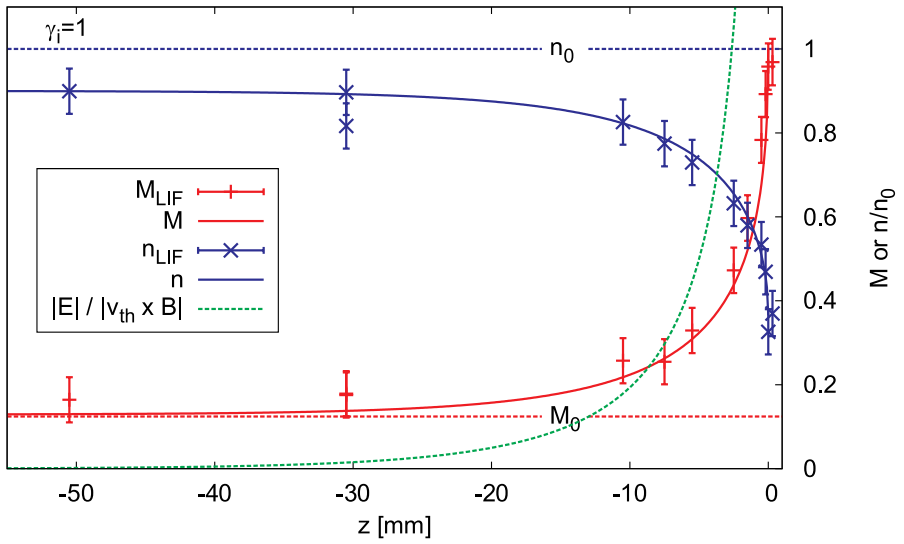

Figure 4.11: Axial profiles of Mach number and density in front of the small target evaluated from the ivdfs shown in Fig. 4.10. The target is located at $z = 0$. The solid lines show the modeling according to Eqs. 4.55-4.56. M_0 and n_0, the Mach number and density when the target is removed from the plasma, are indicated by the dashed horizontal lines.

data. The high collision frequencies assumed previously cannot explain this inconsistency either. Inserting $\nu_i = 8$ kHz and $\nu_{cx} = 20$ kHz, as estimated from the measured neutral gas pressure of $p_n = 24$ mPa (corresponding to a density of $n_n = 4.3 \times 10^{18}$ m^{-3}) leads to rather small changes in the computed profiles but the very short decay length of the Mach number cannot be reproduced this way.

It should be noted here that the ion gyro radius $\rho_i = 10$ mm is of the order of the target diameter ($r_0 = 7.5$ mm), violating the assumption ($\rho_i \ll r_0$) made by Hutchinson. Note that ions with a center of gyration in region (II) may then penetrate region (I) about 2 mm in front of the target. As indicated by the green curve in Fig. 4.11 the electric field force $e\left|\vec{E}\right|$ exceeds the Lorentz force $ev_{th,i}|\vec{B}|$ (of a thermal particle) there and the particle has a high probability of being deflected towards the surface.

In order to investigate in more detail the influence of a finite ratio ρ_i/r_0, information on the radial profiles of density and Mach number is required. Measurements of such profiles – here for the case of the medium target ($\varnothing = 30$ mm) – are shown in Fig. 4.12. For the sake of a simple and stable adjustment, the laser beam and the detection volume were kept at a fixed

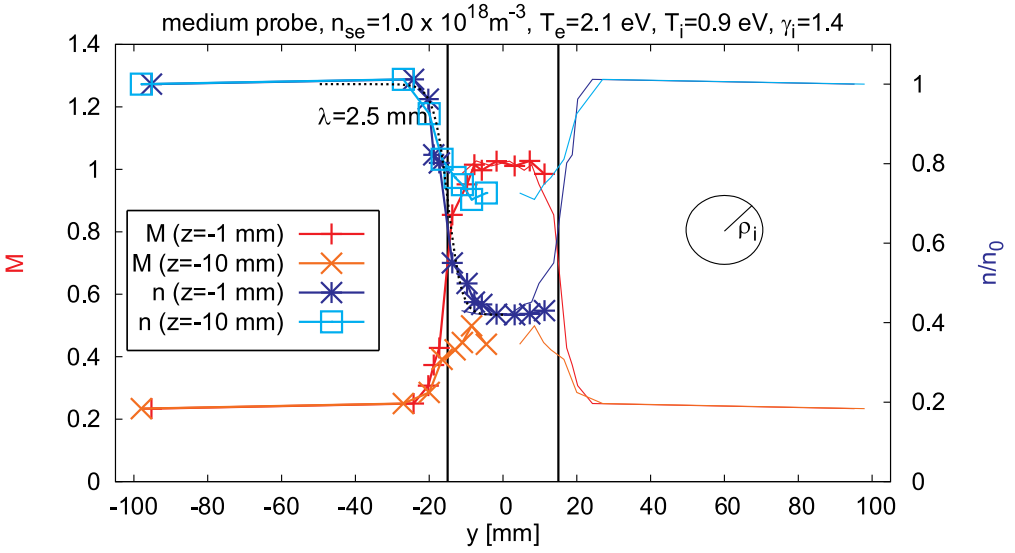

Figure 4.12: Radial profiles of density and Mach number measured by means of LIF.

position, while the target was moved in y direction (vertically).
The two dimensional normalized density and Mach number profiles found in the experiments can be approximated by

$$\widetilde{n}(z,r) = \frac{\widetilde{n}(z,0) - 1}{(r/r_0)^2 \exp\left(\frac{r-r_0}{\lambda_r}\right) + 1} + 1 \tag{4.58}$$

and

$$M(z,r) = \frac{M(z,0) - M_\infty}{(r/r_0)^2 \exp\left(\frac{r-r_0}{\lambda_r}\right) + 1} + M_\infty \ , \tag{4.59}$$

where $\lambda_r = 2.5$ mm is the radial decay length. The functions $\widetilde{n}(z,0)$ and $M(z,0)$ are determined by Eq. 4.55 and Eq. 4.56.

4.3.3 Fields in front of the target

In order to maintain the axial density profile of the electrons an electric field is required that balances the electron pressure gradient. In the stationary case

$$0 = \frac{\partial}{\partial z}\left[\phi(z,r) - \frac{T_e}{e}\ln \widetilde{n}(z,r)\right] \tag{4.60}$$

must hold. With the additional condition that the radial electric field far away from the surface vanishes, *i.e.* with $\phi(r, \infty) = \text{const.}$, the potential is defined (up to a constant which has no physical relevance) by the density within the whole volume[3]:

$$\phi(z, r) = \frac{T_e}{e} \ln \widetilde{n}(z, r) \ . \tag{4.61}$$

It can easily be verified that for any density profile $\widetilde{n}(z, 0)$ given at the axis Eq. 4.61 with Eq. 4.58 fulfills $\nabla \times (\nabla \phi) = 0$, a required condition for any electrostatic potential.
If the potential is given everywhere we can directly compute the electric field and the space charge density

$$\vec{E}(z, r) = -\nabla \phi(z, r) \text{ and } \rho(z, r) = -\epsilon_0 \Delta \phi(z, r) \ . \tag{4.62}$$

Writing the Laplacian in cylindrical coordinates it becomes clear why we introduced a factor $(r/r_0)^2$ in the denominator of Eq. 4.58. This factor assures that $|\lim_{r \to \infty} \Delta \phi| < \infty$ so that the space charge density has no singularity at $r = 0$.
Potential, electric field and space charge density are shown in Fig. 4.13. The three contour plots on the left show the present situation[4] ($D = 20$ m^2/s) whereas the plots on the right were computed assuming $D = 1$ m^2/s. In both cases the radial electric field becomes as large as $E_r = 500$ V/m close to the target surface. However, the extension of the region with such a high field is much larger in the latter case.

[3] We can prove this by allowing an additional potential ϕ' such that $\phi(z, r) = (T_e/e) \ln \widetilde{n}(z, r) + \phi'(z, r)$. Eq. 4.60 then prohibits any axial dependence and the condition $\phi(r, \infty) = \text{const.}$ any radial dependence of ϕ'. ϕ' can then only be a constant.

[4] Note that D here only has the meaning of a fitting parameter and not of a real diffusion coefficient

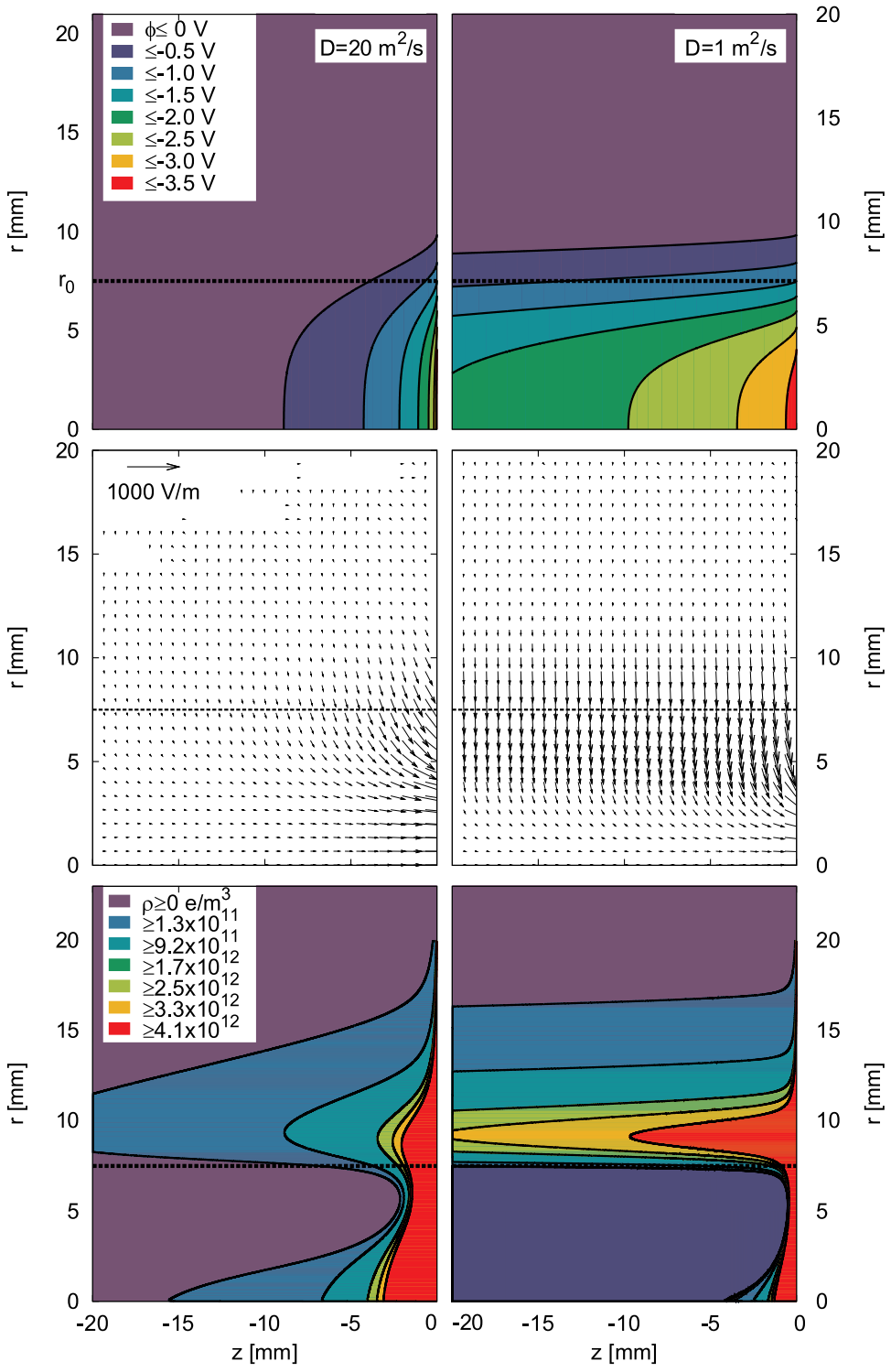

Figure 4.13: Potential, electric field and space charge density in front of the small target. Left: $D = 20$ m^2/s (present case), right: if D was 1 m^2/s. Note that the slope of the space charge density profile is very steep in front of the target surface and that it reaches values around $\rho = 10^{16}$ e/m^3 there.

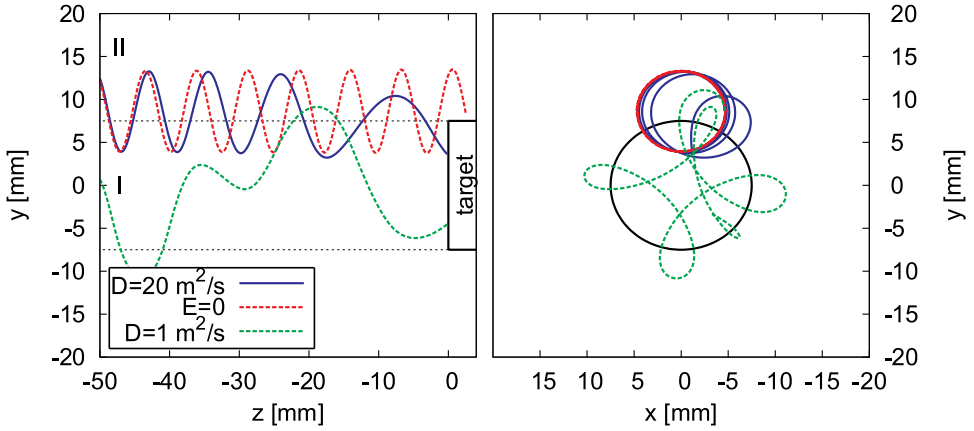

(a) Particle trajectory in the zy-plane (b) Particle trajectory in the xy-plane

Figure 4.14: Motion of a collisionless ion approaching the target (solid blue line). The red dashed line shows the trajectory if there was no potential drop in front of the target. The dashed green line is a particle trajectory in a potential computed with a parameter $D = 1$ m^2/s.

4.3.4 Particle trajectories

One might think that the radial electric field should not cause any radial transport, because the drift $\vec{E} \times \vec{B}/B^2$ points into poloidal direction. However, since the gyro radius is large with respect to the gradient length of the field, we cannot describe the motion in terms of drifts. With $\rho \approx r_0$ we cannot even linearize the equations and we have to compute the actual trajectory of the particle. For an arbitrary collisionless ion the equation of motion is given by

$$\frac{d^2\vec{x}}{dt^2} = \frac{e}{m_i}\left(\vec{E}(\vec{x}) + \frac{d\vec{x}}{dt} \times \vec{B}\right) . \tag{4.63}$$

In Fig. 4.14 the trajectory of an exemplary ion is shown (blue solid line) which hits the target surface under the influence of the electric field given by Eq. 4.62. If there was no electric field the same particle would miss the target (red dashed line). Computing the density profile according to Eqs. 4.55-4.56 with a parameter $D = 1$ m^2/s the radial electric field has a much larger axial extension and affects the ions even if they are still quite far away from the target. The trajectory for this case is indicated by the dashed green line.
In the light of these results the very short decay lengths for Mach number and density are far less surprising. If D was 1 m^2/s the ion trajectories would be completely disturbed and brisk exchange of particles between the two regions

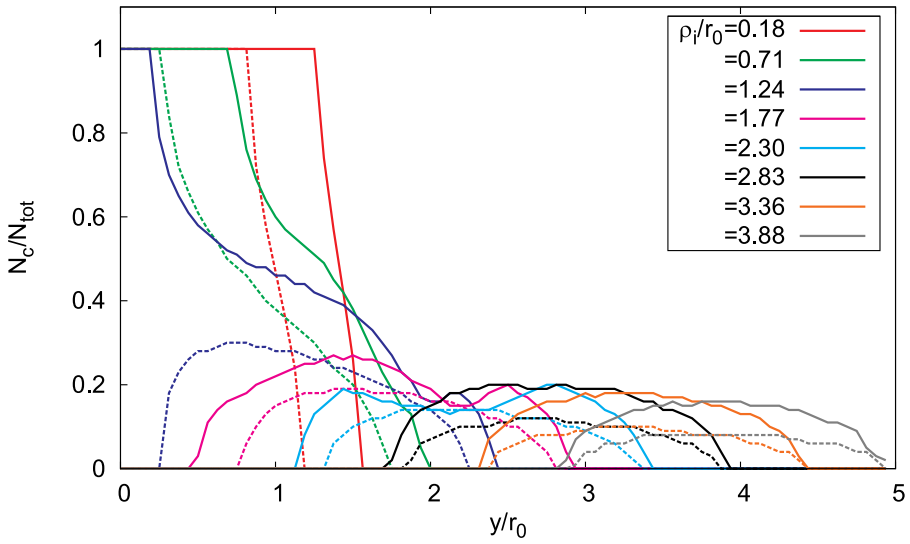

Figure 4.15: A number of particle trajectories were followed with (solid lines) and without (dashed lines) the electric field. The particles started at a distance of $|z| = 60$ mm at different positions y with different gyro radii ρ_i. N_c/N_{tot} is then the number of particles that hit the target over the total number of particles started.

(I) and (II) takes place.
Let us regard now the particle balance for the cylindrical volume in front of the target extended from the surface to a position z_f far away from there where the density is almost equal to that of region (II). For this volume

$$\Phi_z + \Phi_r = \Phi_{target} \tag{4.64}$$

must hold, where $\Phi_z = \pi r_0^2 c_s M_\infty n_\infty$ is the particle flux through the front side of the cylinder, Φ_r is the flux through the lateral surface. Finally, $\Phi_{target} = \pi r_0^2 c_s n_{se}$ is the flux onto the target surface. As the Mach number always increases from M_∞ to 1 and as the density always decreases from n_∞ to n_{se} over the interval $z_f \ldots 0$ independently of the parameter D, we can directly determine the total radial flux

$$\Phi_r = \pi r_0^2 c_s n_\infty \left(\tilde{n}_{se} - M_\infty\right) \ , \tag{4.65}$$

yielding a value of $\Phi_r = 2.8 \times 10^{17}$ s^{-1} particles per second in our case. As we have seen in Sec. 4.2 the diffusive contribution Φ_D is about $D/D_\perp = 20$ times smaller than this total flux Φ_r. The remaining flux $\Phi_{r'} = \Phi_r - \Phi_D$ is

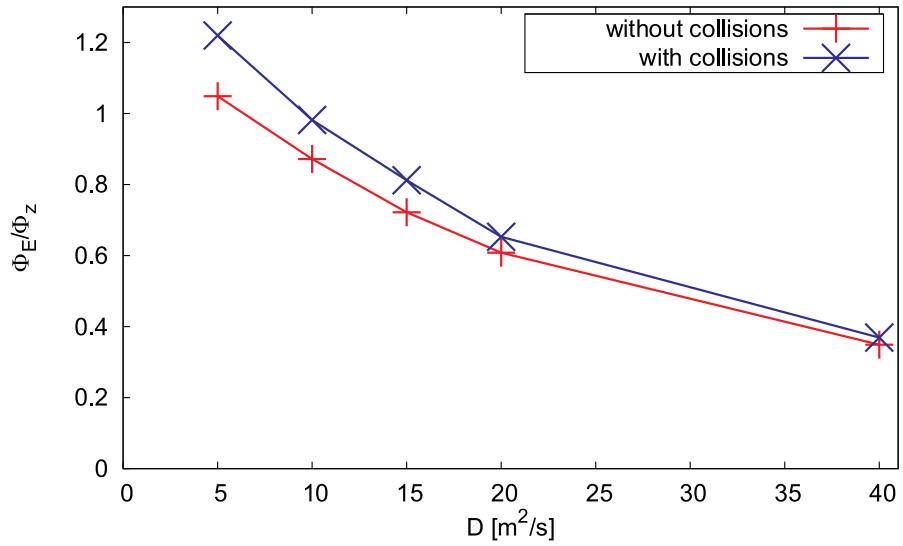

Figure 4.16: The ratio Φ_E/Φ_z computed for different values of D.

then about

$$\frac{\Phi_{r'}}{\Phi_z} = (1 - 1/20)\frac{\widetilde{n}_{se} - M_\infty}{M_\infty} = 1.9 \tag{4.66}$$

times larger than the axial particle influx Φ_z.
In order to quantify the radial transport caused by the electric field a statistical treatment is required. Since the electron flux adapts itself automatically to the flux of the ions in the stationary case, it is sufficient to simulate the ions.[5] We repeat the computation of the trajectory with test particles starting at positions

$$\vec{x} = \begin{pmatrix} \rho_i \sin\theta \\ \rho_i \cos\theta + y \\ -60 \text{ mm} \end{pmatrix} \text{ with the velocity } \vec{v} = \begin{pmatrix} \rho_i\omega\cos\theta \\ -\rho_i\omega\sin\theta \\ v_z \end{pmatrix}, \tag{4.67}$$

where $\omega = v_\perp/\rho_i$ is the gyro frequency. With the help of Eq. 4.63 we follow its trajectory until $z = 0$. If for the final position $x_1^2 + x_2^2 \leq r_0^2$ holds, the particle hits the surface, otherwise it misses it. We then set the label $l_f = 1$ otherwise it is $l_f = 0$. An equivalent label l_i is introduced for the initial position. The computation of the trajectory is then repeated (in total about

[5]Note that this radial transport of the ions is *not* ambipolar. However, as long as parallel net currents carry away the incoming charge from the volume in front of the target, the condition that no net currents flow on a global scale is satisfied.

2 million times) for different values for θ, y, ρ_i, and v_z. For a fixed value of v_z the raise in the number of particles hitting the target is shown in Fig. 4.15. Summing over all particles j we can compute the ratio of radial flux caused by the electric field Φ_E to the axial influx

$$\frac{\Phi_E}{\Phi_z} = \frac{\sum_j f(v_z^j) f(v_\perp^j) y^j v_z^j (l_f^j - l_i^j)}{\sum_j f(v_z^j) f(v_\perp^j) y^j v_z^j l_i^j} \ , \tag{4.68}$$

where $f(v) \propto \exp(-(v/v_{th})^2)$ and $v_\perp = \omega\rho_i$. As shown in Fig. 4.16 this ratio increases from $\Phi_E/\Phi_z = 0.35$ to $\Phi_E/\Phi_z = 1$ as D decreases from $D = 40$ m^2/s to $D = 5$ m^2/s but it is still significantly smaller than $\Phi_{r'}/\Phi_z$=1.9. So far, however, the particle simulation has not taken into account collisions and ionization nor temporal fluctuations of the potential. We can estimate the frequency of ion-ion collisions ν_{ii} from the general formula for momentum exchange of charged test particles α with background particles β

$$\nu_{\alpha\beta} = \frac{16\sqrt{\pi}}{3m_\alpha} \left(\frac{1}{m_\alpha} + \frac{1}{m_\beta} \right) \frac{q_\alpha^2 q_\beta^2 n_\beta \ln \Lambda_{\alpha\beta}}{(4\pi\epsilon_0)^2 \left(v_{th,\alpha}^2 + v_{th,\beta}^2 \right)^{3/2}} \tag{4.69}$$

which yields a value of about $\nu_{ii} = 20$ kHz. With the frequencies for charge exchange and ionization given above we can estimate the mean time between any of these collisions as $\tau_c = (\nu_i + \nu_{cx} + \nu_{el} + \nu_{ii})^{-1} = 18$ μs. This yields a Hall parameter of

$$H = \omega\tau_c = 4 \ . \tag{4.70}$$

An ion thus, on average, does not even complete a single gyration cycle between two collisions .

The collision processes were implemented in the particle simulation in a simple way: During a time step Δt the particle has a probability of $(\nu_i + \nu_{cx} + \nu_{el})\Delta t$ to collide with a neutral atom and a probability of $\nu_{ii}\Delta t$ to collide with an ion. After the collision the velocity vector of the ion points in a random direction and has the length of the thermal velocity of the collision-partner.

This simulation yields a slightly higher radial flux (cf. blue curve in Fig. 4.16) but does not explain the high value of $\Phi_{r'}/\Phi_z$=1.9 either. For this reason the most likely explanation for the high radial transport is that drift waves are excited in front of the target. These instabilities occur in particular in regions with large density gradients as it was in our case.

Nevertheless, a more elaborated simulation, taking into account all these processes and computing the fields and the plasma streaming self-consistently, would be desirable. Unfortunately that is beyond the scope of this thesis.

4.3.5 Macroscopic considerations

We can also describe the radial flux of ions in terms of macroscopic quantities by means of the perpendicular conductivity $\sigma_\perp$ as

$$\Gamma_r = \frac{j_r}{e} = \frac{\sigma_\perp}{e} E_r = -\frac{\sigma_\perp}{e} \frac{\partial \phi}{\partial r} \ . \tag{4.71}$$

With the logarithmic relation between density and potential found before (Eq. 4.61) we have

$$\Gamma_r = -\underbrace{\frac{\sigma_\perp}{e^2} T_e \frac{1}{n}}_{D_\perp} \frac{\partial n}{\partial r} \ , \tag{4.72}$$

which describes a flux. With the perpendicular conductivity given in [46]

$$\sigma_\perp = \frac{m_i n_i \nu_t}{B^2} \tag{4.73}$$

where $\nu_t = \nu_{cx} + \nu_{el} + \nu_i = 18$ kHz again is the total collision frequency, we can determine $D_\perp$ as

$$D_\perp = \frac{m_i T_e}{e^2 B^2} \nu_t \tag{4.74}$$

For our conditions ($T_e = 4.2$ eV and $|B| = 85$ mT) we obtain a value of $D_\perp = 4.5$ m^2/s. Due to the uncertainty of the neutral gas temperature (which is required to derive ν_t) this value might have a significantly different value. This diffusion coefficient is in agreement with the collisional particle model, although still significantly smaller than $D = 20$ m^2/s. In the previous section (Sec. 4.3.4) we saw that the electric field causes a radial transport even without collisions. We can explain such an effect in the macroscopic picture in terms of a polarization current

$$\vec{j}_{pol} = \chi_\perp \epsilon_0 \frac{d\vec{E}}{dt} \ . \tag{4.75}$$

where $\chi_\perp = m_i n/(\epsilon_0 B^2)$ is the (radial) electric susceptibility of the plasma. Although we excluded in our treatment an explicit time dependence of the

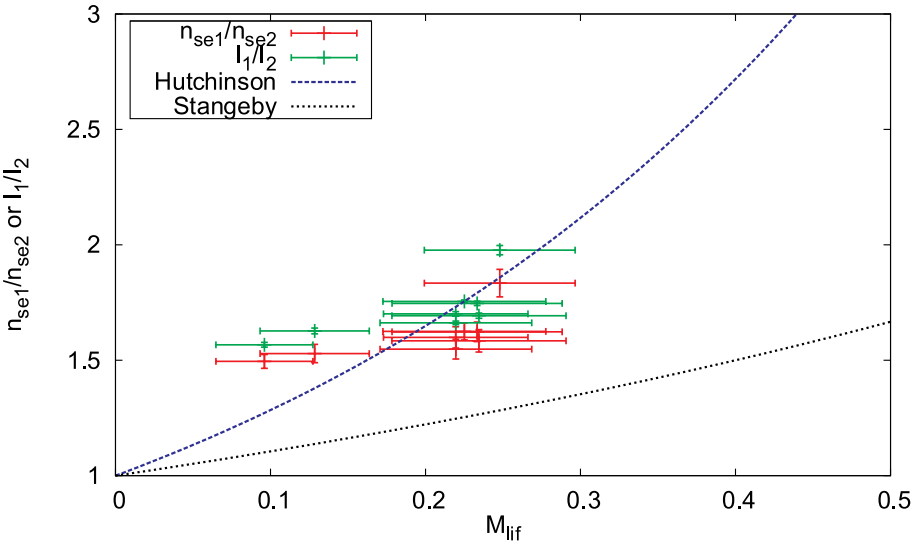

Figure 4.17: Mach numbers measured by LIF and by the electrical collectors on the two sides of the probe in comparison with the models developed by Hutchinson and Stangeby.

electric field, a fluid element moving along the z axis at the velocity u_z effectively 'sees' such a time dependent field:

$$\frac{dE_r}{dt} = u_z \frac{\partial E_r}{\partial z} = -u_z \frac{\partial^2 \phi}{\partial z \partial r} \ . \tag{4.76}$$

In the case where the collision frequency ν^{eff} is high, $\chi_\perp$ has to be replaced by an effective susceptibility:

$$\chi_\perp^{eff} = \frac{m_i n}{\epsilon_0 B^2} \exp\left(-\frac{\nu^{eff}}{\omega}\right) \ , \tag{4.77}$$

although for our conditions the exponential factor in Eq. 4.77 gives only a small correction of about $\exp(-1/15) \approx 0.9$. The radial flux density Γ_r caused by this current is then given by

$$\Gamma_r = -\chi_\perp^{eff} \epsilon_0 \frac{\partial^2 \phi}{\partial z \partial r} = -\frac{m_i n}{eB^2} \exp\left(-\frac{\nu^{eff}}{\omega}\right) u_z \frac{\partial^2 \phi}{\partial z \partial r} \ . \tag{4.78}$$

Dividing this by $\partial n/\partial r$ we obtain a formal Diffusion coefficient from $D = \Gamma_r/(\partial n/\partial r)$. However this value is not constant over z. In a distance of 20 mm it takes values $D \leq 10\,\mathrm{m}^2/\mathrm{s}$ slowly decreasing for large z. However, over the last few mm this value is diverging.

We thus notice that there are two substantial radial fluxes driven by the radial electric field. The first one is of a collisional nature and takes on the structure of a diffusive flux. Conversely, in the case of the polarization current, the collisions are rather damping the fluxes and the diffusion coefficient associated with expression 4.78 is just a quantifying number.
Finally, one may argue that such radial fluxes are not admitted because of the violation of ambipolarity. In fact, they are true ionic currents. There is, however, no need to postulate ambipolar radial fluxes. The only requirement that matters is div $\vec{j} = 0$ in order to avoid infinite charge accumulation. This condition can easily be satisfied by compensating axial electric currents.

4.3.6 Mach probes

In spite of the remaining problems we can answer here the important question of whether one can rely on Mach probe measurements even if the transport is not purely diffusive. Although the variation of the Mach number at different discharge regimes is relatively small, Fig. 4.17 shows that Eq. 4.57 (blue dashed curve) is satisfied fairly well. In contrast, the model given by Stangeby [61] is underestimating the data considerably (black dashed curve). Finally the question arises as to how this enhanced radial transport scales with the probe radius. Since the cross section of the plasma column is about 5 cm we cannot investigate the case of a target in a homogeneous plasma which is at the same time large with respect to the gyro radius. Measurements in front of the medium probe ($\varnothing = 30$ mm), however, show a similarly high D parameter as in the case of the small probe ($\varnothing = 15$ mm).

4.4 Electrostatic sheath region

In order to perform measurements with Laser induced fluorescence on ions in a plasma a couple of experimental difficulties have to be overcome. These were described in Chapter 2. For a long time it seemed impossible to measure a significant LIF signal with a diode laser in PSI-2 at all and so one of the most fascinating observations was that with a well aligned arrangement this signal could still be detected unambiguously even when the slit aperture was as small as $\Delta z' = 0.5$ mm and when the space angle was reduced by a factor of four at the same time. The spatial resolution then becomes as high as $\Delta z = 50$ μm and the electrostatic sheath, which has an extension of several Debye lengths $\lambda_D = 15$ μm (cf. Sec. 4.1), starts to become observable in the experiments.
However, when measuring at such a high spatial resolution new difficulties arise. First, the positioning accuracy of the belt-driven z-manipulator is not much better than $\Delta z' = 1$ mm due to its principle of construction. For this reason a second positioner with a 100 times higher accuracy was installed on the detector head. Another point that we are concerned with is the finite diameter of the laser beam. Even if the detection volume is adjusted perfectly to the center of the beam, LIF photons from the edge of the beam are collected from an interval of

$$\Delta z = \frac{r_l}{d_o} r_{las} = 100\,\mu\text{m} \ , \tag{4.79}$$

where $r_l = 5$ cm is the radius of the lens, $d_o = 50$ cm is the distance from the detection volume to the lens, and $2r_{las} = 2$ mm is the diameter of the laser beam. For this reason the lens radius was reduced to $r_l = 2.5$ cm by covering it with an aperture plate. This is a well known measure in photography to increase the depth of field.
Let us envisage now the behavior of the ion velocity distribution in the electrostatic sheath. As discussed in Sec. 4.1 the ions fall practically collisionless through the potential drop. The velocity of the particle v' is then given by the conservation of energy

$$\frac{1}{2} m_i v'^{\,2} + e\Phi(z) = \frac{1}{2} m_i v^2 + e\Phi_{se} \ , \tag{4.80}$$

where v is its velocity at the sheath edge. Furthermore conservation of the flux must hold and within the sheath and we can write

$$f(v', z) v' dv' = f_{se}(v) v dv \ , \tag{4.81}$$

where $f_{se}(v)$ is the distribution function at the sheath edge. With $vdv = v'dv'$ we obtain

$$f(z, v') = f_{se}\left(\sqrt{v'^2 + \frac{2e}{m_i}(\Phi(z) - \Phi_{se})}\right) \quad . \tag{4.82}$$

The maximum of the distribution function at the sheath edge is thus conserved.
Fig. 4.19 shows $f_{se}(v)$ measured at the position $z = -1$ mm (orange curve). It is fitted (red curve) by a smooth distribution function with $f(v = 0) = 0$. The other curves (blue, magenta, cyan and black) are the distributions computed from Eq. 4.82. A different representation of exactly the same distribution function $f(v, z)$ is shown underneath (Fig. 4.19, middle), but there v is kept constant and z is varied. Such profiles would be expected when measuring LIF with a spatial resolution of the order $\Delta z = 1$ μm keeping the wavelength constant and moving the detector. As mentioned at the beginning, however, the real spatial resolution is about $\Delta z = 50$ μm. We blur these profiles artificially over this interval and compare them to the measurements in the figure at the bottom. The peaks are less pronounced than in the figure above, but they are clearly recognizable[6]. Thus, the existence of the electrostatic sheath has been unambigously proved experimentally.

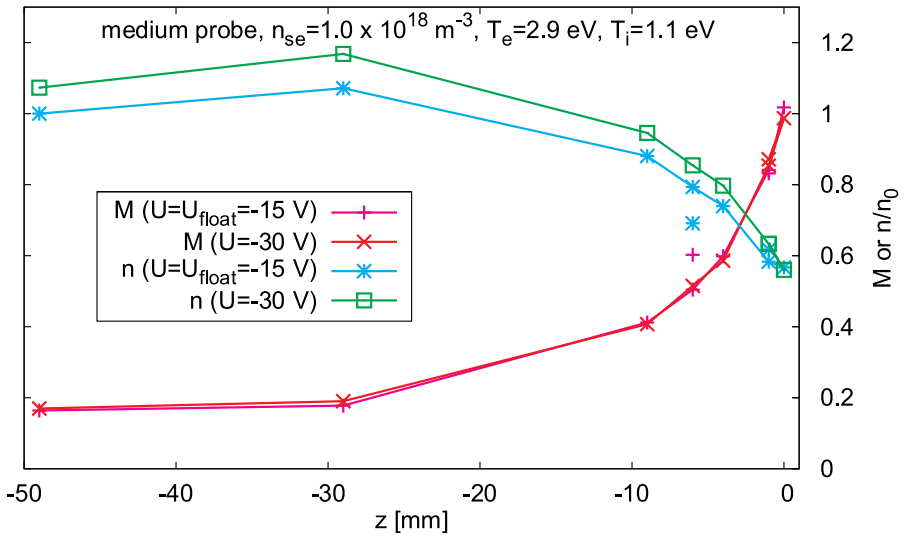

Figure 4.18: Evaluated Mach number and density profiles with (red and green curves) and without (magenta and cyan colored curves) biasing of the electric collector

[6]Note that during the measurement some positioning information was lost. The z position of the blue and the black curve were corrected by $-250\,\mu$m.

4.4.1 Biasing

Furthermore, we can consider Fig. 4.18 as a proof for the fact that the Debye screening is working efficiently. Here the ivdf was measured in front of the collector in the center of the probe while this was biased by $U = -30$ V. With respect to the floating case $U_f = -15$ V the biasing has no effect at all on the Mach number (cf. red and magenta colored curves). The density on the other hand seems to be influenced by the biasing (blue and cyan colored curves). However, the larger LIF signal could also be due to an increased population of the metastable level caused by a slightly increased electron temperature, *i.e.* by ohmic heating of the electrons when a current is drawn from the plasma.

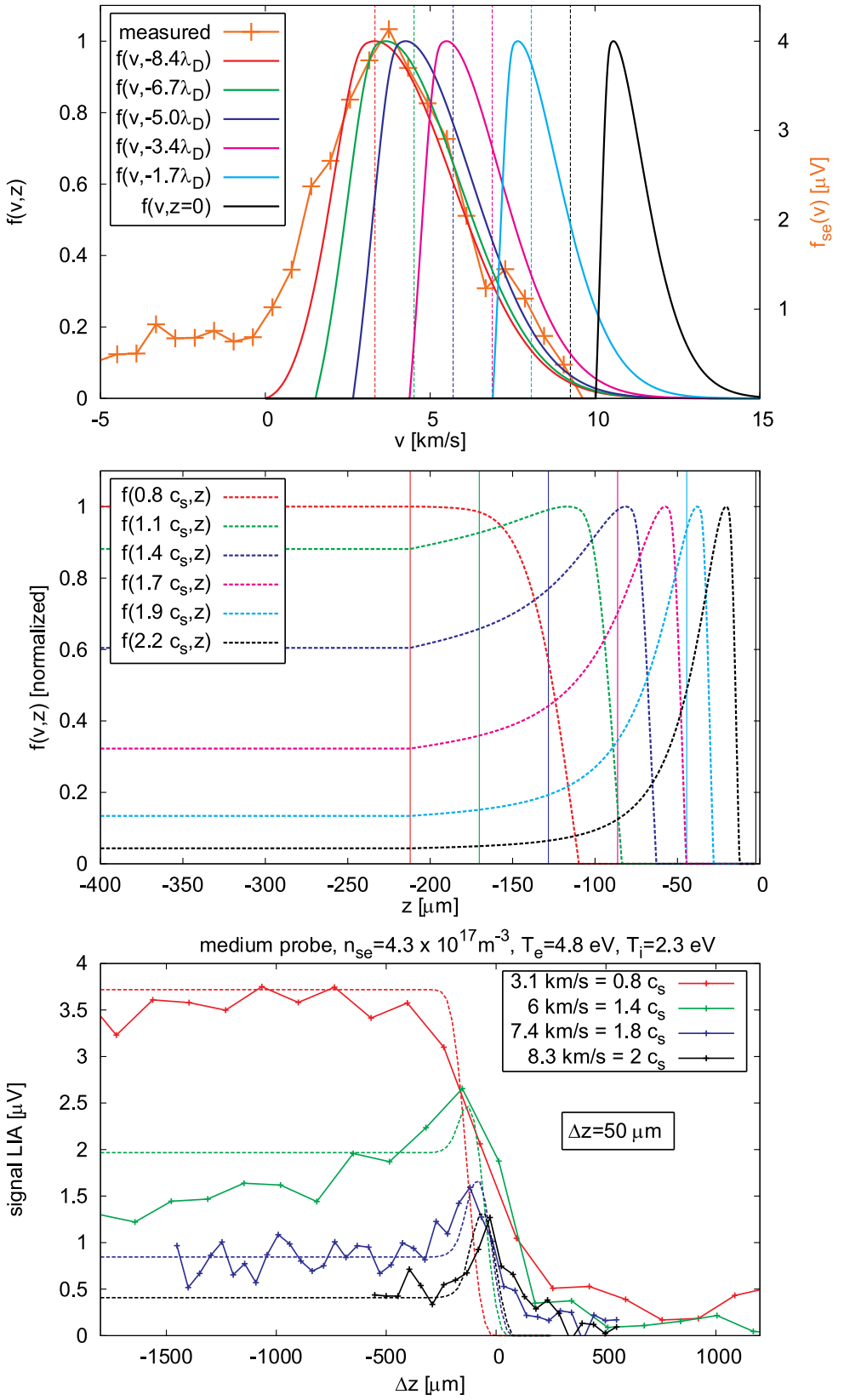

Figure 4.19: Top: Ion velocity distribution $f_z(v)$ at different positions z in the electrostatic sheath in front of the target. Middle: The same function $f_z(v)$ as above but for different fixed values of v. Bottom: $f_z(v)$ is blurred over an interval of $\Delta z = 50$ μm and compared to measured LIF signals when scanning the z position at a fixed wavelength.

4.5 Oblique incidence

So far we have only been concerned with the case where the magnetic field lines hit the target surface under normal incidence. In the divertor of a fusion device, however, it is desirable to spread the power load over a large area and so the case where the field lines impinge on the divertor tiles under shallow angles is of particular interest. We want to address this situation now, both experimentally and from the point of view of modeling.

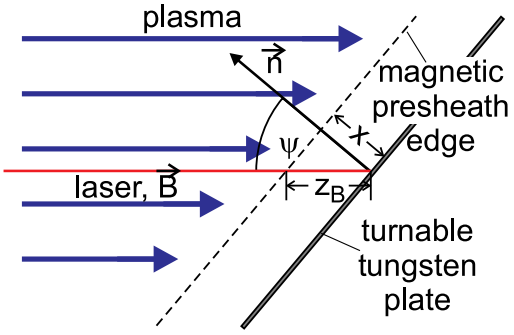

Figure 4.20: LIF measurements in the magnetic presheath of a turnable tungsten target

4.5.1 Modeling

The mathematical description of the situation changes significantly then. The magnetic field, previously taken into account only indirectly (when estimating the cross-field diffusion), now appears in the momentum equation. In 1982 Chodura [10] addressed this situation in terms of both a two-fluid and a particle-in-cell model. According to him, in addition to the usual sheath and presheath, a third region emerges in between when the magnetic field hits the surface under non-normal incidence. This region will be called the magnetic or 'Chodura' presheath in the following. When modeling this region it is useful to chose a coordinate system with one axis parallel to the surface normal. Like Chodura we chose x. Assuming the plasma is extended over a large region in y and z directions, we can make use of the symmetry and neglect derivatives $\partial/\partial y = \partial/\partial z = 0$ (and also $\partial/\partial t = 0$, assuming stationarity). The magnetic field vector in this coordinate system is given by

$$\vec{B} = \vec{e}_B B \text{ , where } \vec{e}_B = \begin{pmatrix} \cos\psi \\ 0 \\ \sin\psi \end{pmatrix} . \tag{4.83}$$

As we have seen in Sec. 4.2, sources and collisional friction are important for plasmas with conditions similar to those in PSI-2. So, in contrast to Chodura, we want to take these terms into account in the modeling. The

continuity equation then reads

$$(nu_x)' = n\nu_i \ , \ \frac{\partial}{\partial y}(nu_y) = \frac{\partial}{\partial z}(nu_z) = 0 \ , \tag{4.84}$$

where the abbreviation $' := \partial/\partial x$ is used. We express the electric field by the density gradient (applying the momentum equation of the electrons Eq. 4.20 the electric field is $e\vec{E} = -\gamma_e T_e(\nabla n)/n$) in order to obtain the momentum equation for the ions

$$u_x \vec{u}' = \frac{e}{m_i}\vec{u} \times \vec{B} + \frac{c_s^2}{u_x}\left(u_x' - \nu_i\right)\vec{e}_x - \nu_t \vec{u} \ , \tag{4.85}$$

where, as before, $\nu_t = \nu_i + \nu_{cx} + \nu_{el}$ is the total collision frequency and $\vec{e}_x$ is the unit vector in x-direction. We can then integrate this equation numerically by resolving with respect to $\vec{u}'$ (writing Eq. 4.85 component-wise) and then approximating ∂x by a finite element Δx:

$$\vec{u}(x + \Delta x) = \vec{u}(x) + \Delta x \vec{u}'(x) \ . \tag{4.86}$$

Before we can start this iteration it is necessary to find an adequate boundary condition. In the sheath the motion of the particles is dominated completely by the electric field so we can comfortably neglect the influence of the magnetic field there. All arguments for the derivation of Eq. 4.28 then still hold, therefore the Bohm criterion $u_x|_{se} \geq c_s$ must be fulfilled at the sheath edge. However, the other components of the vector (u_y and u_z) are not determined ab initio. Chodura found in his analysis another condition for a stable magnetic sheath, $u_x \geq c_s \cos\psi$. This condition must hold at the edge of the magnetic sheath where the plasma is still bound to the magnetic field lines and where $\vec{u}$ and $\vec{B}$ are parallel. We write $\vec{u}$ as

$$\vec{u} = c_s M_c \vec{e}_B \ . \tag{4.87}$$

Choosing $\nu_i = \nu_t = 0$ for the moment we can verify Chodura's criterion for a stable sheath. If we start the integration of Eq. 4.85 with values $M_c \geq 1$ solutions are always smooth (monotonically increasing), otherwise oscillations are observed. This is independent of the angle ψ.
Applying this condition we are then also able to reproduce Fig. 7 in [10] by integrating Eq. 4.85.
If we assume finite ionization and collision frequencies the situation changes significantly. In Fig. 4.21 the critical Mach number M_c (the smallest value found numerically for which the solution is not oscillating) is shown for different ionization and collision frequencies and for two different angles. It

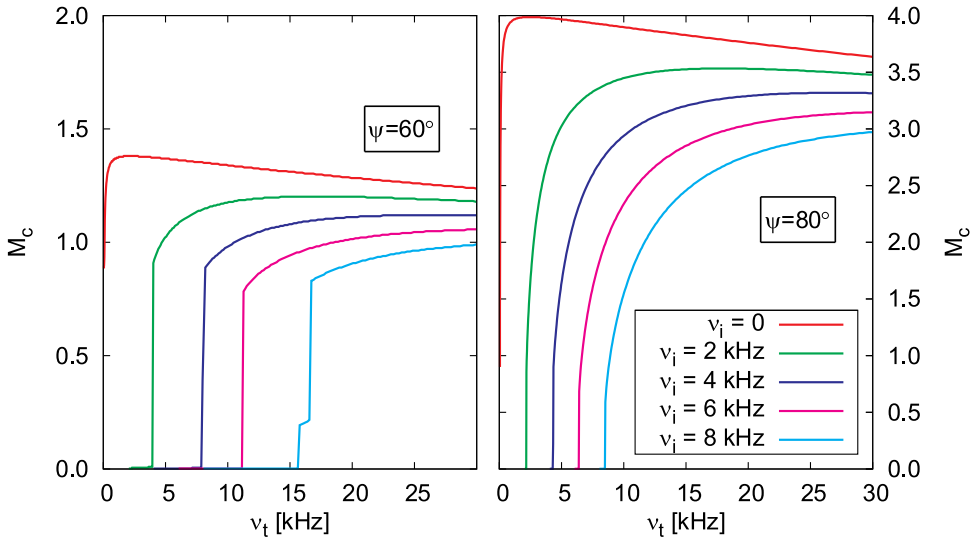

Figure 4.21: Critical Mach number M_c for different ionization and collision frequencies. Note the different scales in the left figure ($\psi = 60°$) and in the right figure ($\psi = 80°$)

turns out that a highly collisional regime requires high values of M_c, while ionization has a stabilizing effect and M_c may be smaller.
We want to compare the computed profiles to the measurements now. Since – here as before – the laser is launched into PSI-2 through the hollow cathode it is to good approximation parallel to the magnetic field lines, and we have to project $\vec{u}$ onto $\vec{e}_B$. The Mach number parallel to $\vec{B}$ is then

$$M_B = \frac{\vec{e}_B \cdot \vec{u}}{c_s} \ . \tag{4.88}$$

The distance z_B from a point on a plane $x =$ const. to the point where the field line hits the target surface is $z_B = x/\cos\psi$.

4.5.2 Measurements

In Fig. 4.22 measurements with Laser induced fluorescence are shown where the magnetic field lines and the laser hit the target under oblique incidence. In the first case Fig. 4.23(a) the large circular boron nitride target ($\varnothing = 100$ mm) under a fixed angle of about $\psi = 80°$ was used. The lower part of the figure (Fig. 4.23(b)) shows measurements where a turnable rectangular tungsten plate (130×80 mm^2) served as a target. During

the measurements with this target the window was coated with sputtered material from the target and so its transmission was not constant. As we cannot correct this effect in a simple way, we confine ourselves to showing only the Mach number here. Measurements at angles around 45° could not be performed successfully, since the very strong light emission from the discharge region was then reflected towards the detector and the background signal increased more than an order of magnitude. The measurements with $\psi = 50°$ and $\psi = 60°$ therefore have a large error bar.

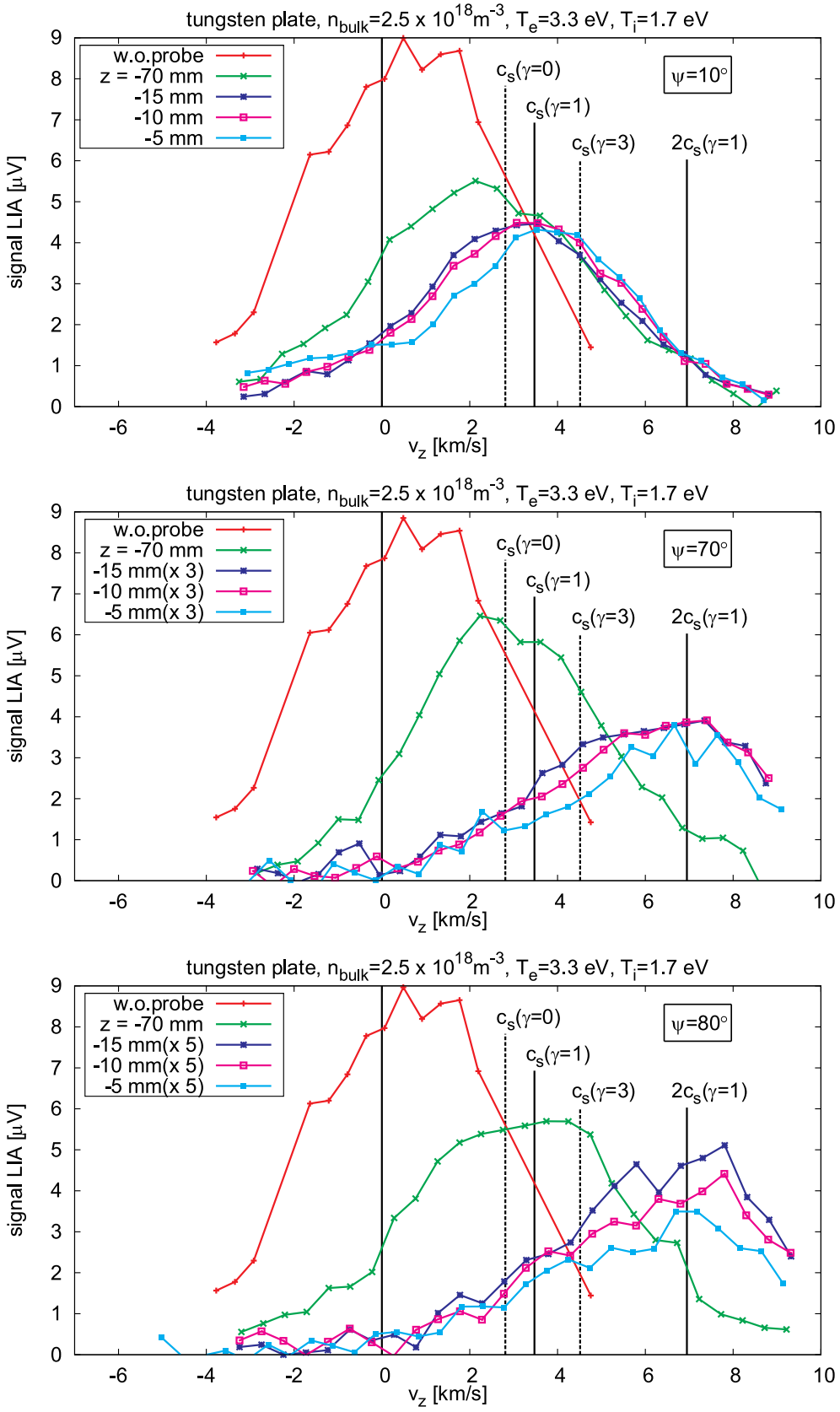

Figure 4.22: Ion velocity distributions measured at different axial positions in front of a turnable target. The three figures represent the turning angles 10°,70° and 80°

We observe that the streaming velocity becomes clearly supersonic in front of target. The Mach number and the extension of this region furthermore is increasing with increasing angles. Immediately in front of the surface the Mach number is predicted fairly well (to about 15%) by the original Chodura model (dashed lines). The size of the magnetic sheath and the profile of the Mach number within this region, however, deviate strongly from the computed values.
The attempt to fit the series of profiles with realistic ionization and collision frequencies was not very successful. According to Fig. 4.21 the condition for a non-oscillating magnetic presheath for an angle of $\psi = 80\ ^\circ$, an ionization frequency of $\nu_i = 3.3$ kHz, and a total collision frequency of $\nu_t = 27$ kHz is a critical Mach number of $M_c \geq 3.5$. Such high values were not found in the experiment. The most likely explanation for this is that the finite size of the target matters. In particular for angles around $\psi = 80\ ^\circ$ the target plate does not cover the whole plasma cross section and the symmetry along the y and z directions can hardly be assumed anymore. Furthermore, if the oscillation period of the solutions of Eq. 4.85 is larger than the z_B-extension of the target we may not be surprised to find sub-critical Mach numbers at the edge of the magnetic sheath edge.
However, as a qualitative result, we can summarize that clearly supersonic streaming velocities were found in a region of a few cm in front of the target, as predicted by the modeling.

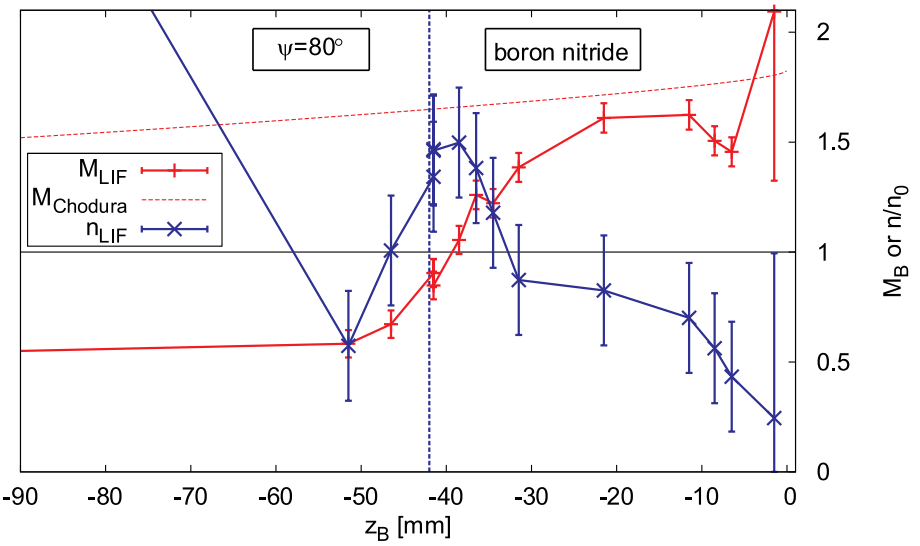

(a) Axial profiles of Mach number and density in front of a boron nitride target under 80° incidence. Dashed red line: Theoretical Mach numbers determined from Eq. 4.85 according to Chodura ($\nu_i = \nu_t = 0$). The dashed blue line indicates the edge of the target. Beyond this position the LIF signal (but also background signal) increases significantly.

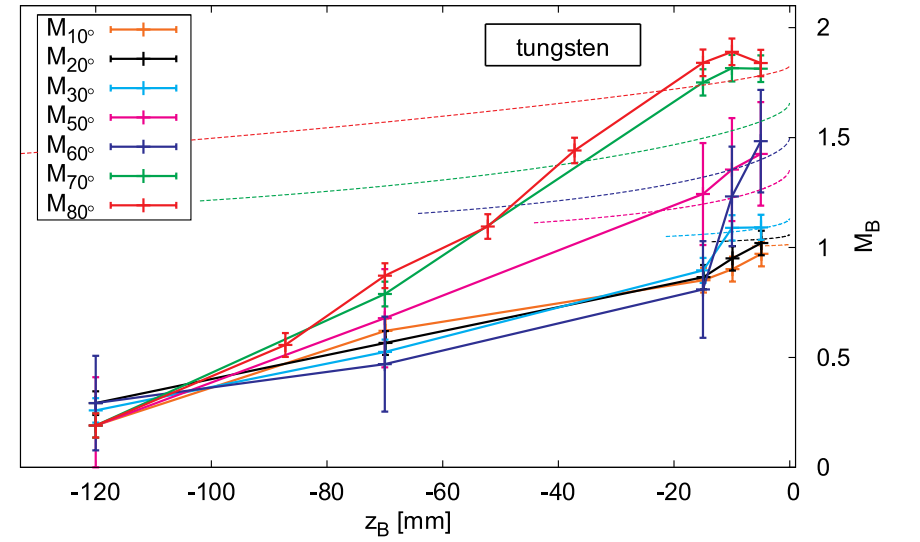

(b) Axial profiles of Mach number and density in front of a tungten target under oblique incidence evaluated from Fig. 4.22. As above the dashed lines represent the Chodura model. These lines also indicate the theoretical end of the magnetic presheath.

Figure 4.23: Plasma-Wall transition under oblique incidence.

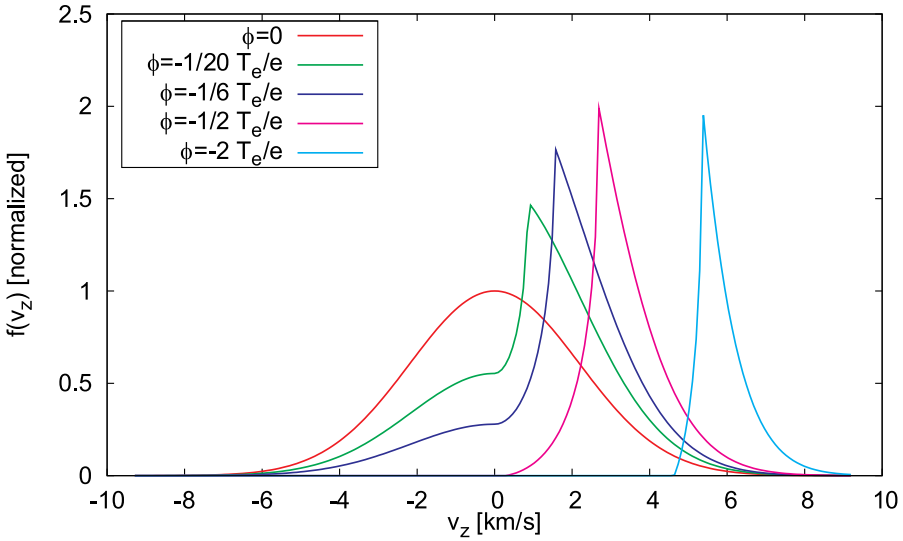

Figure 4.24: Change of the ion velocity distribution when approaching the wall according to Emmert *et al.* [15].

4.6 Non-Maxwellian velocity distributions

Ions recombine with electrons at surfaces of a solid obstacle very efficiently. As confirmed very well in previous sections, any obstacle can be assumed as an absolute sink for the plasma. In the immediate vicinity of the surface we can only find ions with positive velocities, *i.e.* velocity vectors directed towards the surface. Negative components of the ivdf are suppressed completely, $f_w(v < 0) = 0$.

As long as this part of the ivdf is not repopulated by collisions, we also expect non-Maxwellian velocity distributions at a certain distance to the wall, *i.e.* on a length scale of the order of the mean free path length for ion-ion collisions.

In the previous sections, where ion temperatures were moderate, the measured velocity distributions had a Gaussian shape even very close to the surface. Here, however, we want to address measurements with a strongly reduced gas inlet. Electron and ion temperatures are then significantly higher and the mean free path length for ion-ion collisions increases strongly. As shown in Fig. 4.25 the ivdfs become clearly non-Maxwellian under these conditions.

A model for the change of the distribution function in front of a surface was set up by Emmert *et al.* [15]. An important feature of this model is that ions

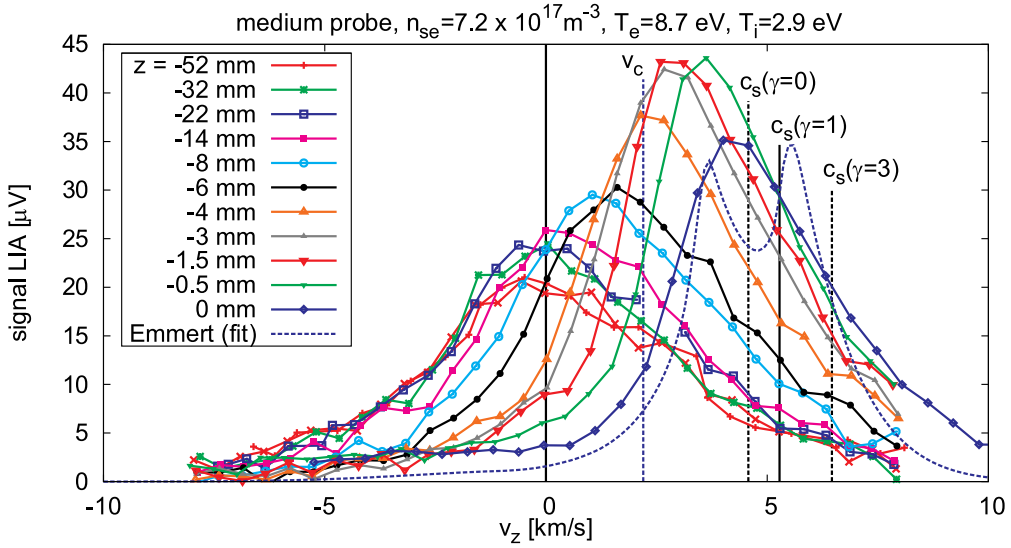

Figure 4.25: Non-Maxwellian velocity distributions in front of a target.

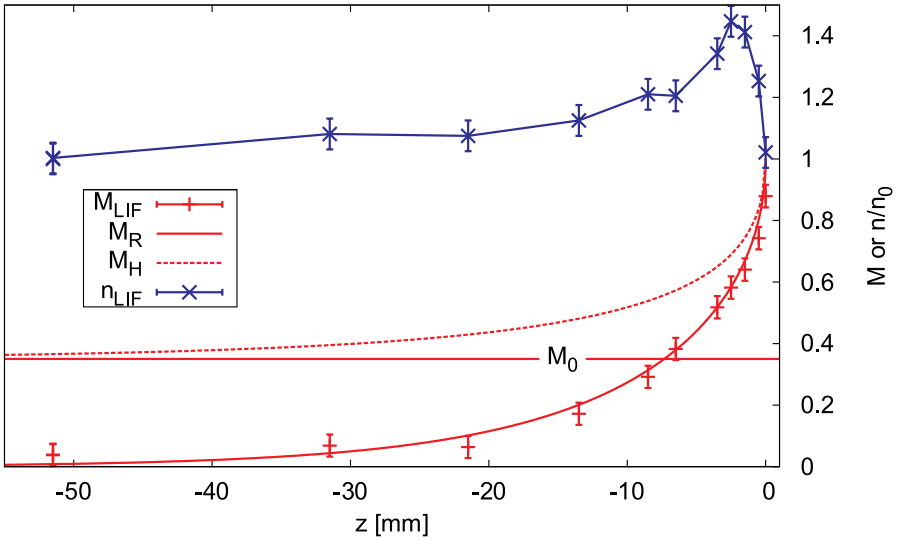

Figure 4.26: Axial profiles of Mach number and density in front of the medium size target evaluated from Fig. 4.25. M_R and M_H are the Mach numbers predicted by the recycling model (Eq. 4.45) and by Hutchinson's model Eqs. 4.55-4.56.

are 'born' with a finite temperature. The source function S is given by

$$S(z,E) = \frac{S_0 h(z)}{2T_i} \exp\left(\frac{q\phi(z)}{T_i}\right) \exp\left(-\frac{E}{T_i}\right) \ . \tag{4.89}$$

Although at least questionable in general, in our case this assumption might be justified, since thermalized ions may diffuse into the region in front of the (medium size) target.
Assuming only singly ionized particles, $Z = 1$, the ion velocity distribution according to Emmert *et al.* [15] is given as a function of the potential by

$$f(v_z, \phi, T_e, T_i) = n_0 \sqrt{\frac{m_i}{2\pi T_i}} \exp(\tau\psi_0)\, H(v_z, T_e, T_i, \psi) \ , \tag{4.90}$$

with the definitions

$$\psi = -\frac{e\phi}{T_e} \qquad \psi_0 = \psi - \frac{m_i v_z^2}{2T_i\tau} \qquad \tau = \frac{T_e}{T_i} \tag{4.91}$$

$$H = \begin{cases} 1 + F(\psi) & \text{if } v_0 < v_z \\ 1 + F(\psi) - 2F(\psi_0) & \text{if } 0 < v_z < v_0 \\ 1 - F(\psi) & \text{if } v_z < 0 \end{cases} \tag{4.92}$$

$$F = \operatorname{erf}\left(\sqrt{\tau\psi}\right) + \frac{2}{\sqrt{\pi\tau}} \exp(-(1+\tau)\psi)\, D\left(\sqrt{\psi}\right) \tag{4.93}$$

$$D(x) = \int_0^x \exp(t^2) dt \qquad v_0 = \sqrt{\frac{2T_i\psi}{m_i}} \ . \tag{4.94}$$

This function is shown in Fig. 6 in [15], which is reproduced in Fig. 4.24. For the time being we observe that the velocity distribution becomes narrower and higher when approaching the surface which is in qualitative agreement with Fig. 4.25. However, a deeper analysis shows that we cannot explain quantitatively the experiment with the Emmert model. The theoretical distribution function becomes so narrow that the Zeeman splitting should become observable. We can compute the expected LIF signal superposing two (or more accurately 16) shifted distribution functions similar to those in Fig. 3.6. As seen in Fig. 4.25 the agreement of $f(\phi = -1/2T_e/e)$ (blue dashed curve) with the measured ivdf close to the surface (blue solid curve) is poor. However, as we had seen in Fig. 4.1 in Sec. 4.2, the rate coefficient for ionization (Eq. 4.22) increases dramatically in the interval $T_e = 2 \ldots 9$ eV and therefore we cannot neglect the recycling anymore. Assuming that the neutrals are in thermal equilibrium with the target material ($T = 300 \ldots 1000$ K), *i.e.* that the velocity of the neutrals emitted from the surface is around $350 \ldots 650$ m/s, the mean free path for ionization becomes as small as $\lambda_n = 1.6 \ldots 3$ cm.

In Sec. 4.2 we introduced a simple model for the situation when the mean free path length is of the order or smaller than the target diameter. As shown there the Mach number and density profiles depend only on λ_n. Such profiles were plotted in Fig. 4.26 according to formula 4.45. As the ivdfs in Fig. 4.25 are strongly non-Maxwellian, the experimental data points for M_{LIF} and n_{LIF} are obtained by computing the moments[7]

$$n = \int f(v_z)dv_z \quad u = \frac{1}{n}\int v_z f(v_z)dv_z \quad T_i = \frac{2}{3}\langle E\rangle = \frac{1}{n}\int m_i(v_z-u)^2 f(v_z)dv_z \ . \tag{4.95}$$

Another particularity of the measurements shown here is that, due to the high electron temperatures, the total light emission of the plasma is orders of magnitude higher than before. Under these conditions nonlinear effects of the LIF detection were observed. The signal strength indicated by the lock-in-amplifier depends on the background emission of the plasma. If the detection volume is now moved between regions with different densities (and therefore background light emission) the LIF signal is detected with different sensitivities. The actual density might thus be significantly different than that shown by the blue curve in Fig. 4.26. We can trust the measurement of Mach number much more, however, since the evaluation of the mean velocity does not depend on the sensitivity of the lock-in amplifier.
Although the measurements in Fig. 4.25 are not fully understood up to now, we can note that the Hutchinson model is *not* able to describe the situation. The Mach number, evaluated according to Eq. 4.57 from the ratio of ion saturation currents is $M_0 = 0.35$, while the Mach number found far away from the surface is almost zero (cf. red dashed curve and red solid line).
Here as well as in previous sections the Mach number was found to be unity close to the target surface as predicted by the (hydrodynamic) Bohm criterion. In Sec. 4.1 we saw that the velocity distribution of the ions f_i has to fulfill another condition, the kinetic Bohm criterion, Eq. 4.32. An important question is whether $f_i(v_z)$ has actually a finite value for $v_z = 0$ at the sheath edge as we would infer from the measurements in Fig. 4.25. In this case the integral in Eq. 4.32 does not converge and the kinetic Bohm criterion would clearly be violated. In order to fulfill the kinetic Bohm criterion we must assume $f_i(v_z) = 0$ for $v_z \leq v_c$, where the critical velocity is $v_c = 2200$ m/s. v_c is indicated by the dashed vertical line in Fig. 4.25.

[7]Note that for a non-Maxwellian distribution a temperature is strictly speaking not defined. The evaluation of T_i is furthermore very sensitive to fluctuations in the wings of the distribution. Before applying Eq. 4.95 the distributions are therefore smoothed.

4.7 Particle and momentum fluxes – Measurement of the ion temperature

In this section we want to analyze the measurements from the current-force probe. The arrangement and the calibration were already described in detail in Sec. 2.3.

4.7.1 Expected forces to the probe heads

First, we want to address theoretically the expected forces to the probe heads. The force density $\vec{\mathcal{F}} = d\vec{F}/dV$ is defined by the divergence of the momentum flux tensor $\overleftrightarrow{P}$

$$\vec{\mathcal{F}} = -\nabla \cdot \overleftrightarrow{P}, \text{ whose elements are given by} \tag{4.96}$$

$$P_{ij} = \sum_\alpha P_{ij}^\alpha = \sum_\alpha \int m_\alpha v_i v_j f_\alpha d^3v \ . \tag{4.97}$$

The sum is taken over all particle species α and the integral extends over all velocity space.
In order to compute the total force acting on the probe we integrate $\mathcal{F}$ over a cylindrical volume. Its front side is identical to the probe surface (to be precise, we select an area located slightly underneath the probe head surface so that no plasma particles can pass it). For the moment we choose the opposite surface to be identical with the sheath edge. The Gaussian divergence theorem can then be applied:

$$\vec{F_p} = -\int \nabla \cdot \overleftrightarrow{P} d^3x = -\oint \overleftrightarrow{P} \cdot d\vec{f} = A_p P_{zz} \vec{e}_z|_{se} \ . \tag{4.98}$$

This means that the pressure force $\vec{F_p}$ can be determined from the momentum flux at the sheath edge. Momentum flux through the lateral surface (*e.g.* due to diffusion or the gyration motion of the ions) is clearly negligible. The distributions in Eq. 4.98 are assumed to be homogeneous in x and y and symmetric in v_x and v_y directions ($P_{xz} = P_{yz} = 0$).
With the common definitions of density n_α, streaming velocity u_α, pressure p_α, temperature T_α and the random velocity, introduced as $\vec{w} = \vec{v} - \vec{u}^\alpha$, the z-component of the force can be written as

$$F_p = A_p \sum_\alpha \int m_\alpha \left(u_\alpha + w_z\right)^2 f_\alpha(z_{se}, v_z) d^3v = A_p \sum_\alpha \left(m_\alpha n_\alpha u_\alpha^2 + p_\alpha\right)_{se} \ . \tag{4.99}$$

no	**0**	**1**	**2**	**3**	**4**	**5**	**6**	**7**
n_{e1} [10^{18} m^{-3}]	0.80	0.56	0.58	1.36	1.90	2.39	2.81	3.08
n_{e2} [10^{18} m^{-3}]	0.44	0.37	0.39	0.84	1.17	1.54	1.75	1.95
T_{e1} [eV]	3.1	5.0	6.1	2.6	2.8	3.1	3.1	2.5
T_{e1} [eV]	2.5	4.0	5.2	2.2	2.3	2.5	2.6	2.1
T_i [eV]	1.3	3.2	4.0	0.8	0.9	1.2	1.5	0.7
F_{p1}/A_p [Pa]	1.23	1.55	2.00	1.64	2.50	3.58	4.55	3.51
F_{p2}/A_p [Pa]	-0.57	-0.89	-1.20	-0.86	-1.30	-1.98	-2.48	-1.91
F_1/A_p [Pa]	0.89	0.88	1.01	1.10	1.63	2.18	2.91	2.49
F_2/A_p [Pa]	-0.15	-0.16	-0.22	-0.28	-0.40	-0.56	-0.74	-0.64

Table 4.2: Quantities measured by the current-force probe and by LIF. The values are rounded according to their errors.

Due to ambipolarity $\Gamma_i = \Gamma_e$ and quasineutrality $n_i = n_e = n$, the streaming velocities of electrons and ions are equal $u_e = u_i$, and as such the electron streaming term in Eq. 4.99 can be neglected because of their small mass. Applying the Bohm condition, $u_i = c_s$, the force on the plate becomes

$$F_p = A_p n_{se} \left(m_i c_s^2 + T_e + T_i + m_i |u_n| c_s \right) \Big|_{se} \tag{4.100}$$

where we assumed equality of fluxes, $|n_n u_n| = |n_{se} c_s|$, close to the target surface. For the case $\gamma_i = 1$, and assuming the density falls from n_∞ to $n_\infty/2$ when approaching the target (and $u_n = 0$), this leads to the intuitively expected result $F = A_p (p_i + p_e)$, where p_i and p_e are the pressures far away from the probe.
This must also hold if we chose a much larger cylindrical volume, provided that the radial momentum transport, *i.e.* viscosity, can be neglected. However, as we have seen in Sec. 4.3 the radial transport of particles and momentum is very high and so Eq. 4.100 is the most adequate formula to determine the force on the probe.
Since all quantities can be measured with the present arrangement (n_{se}, T_e, F_p by the current-force probe and T_i by means of LIF) we want to compare the experimental results now and test the validity of formula 4.100

4.7.2 Measurements

Fig. 4.27 shows a typical measurement of the force sensor performed in PSI-2. In order to calibrate U_{offs} in Eq. 2.23 the discharge was turned off temporally. The absolute value of the forces measured by the two pendulums (red and

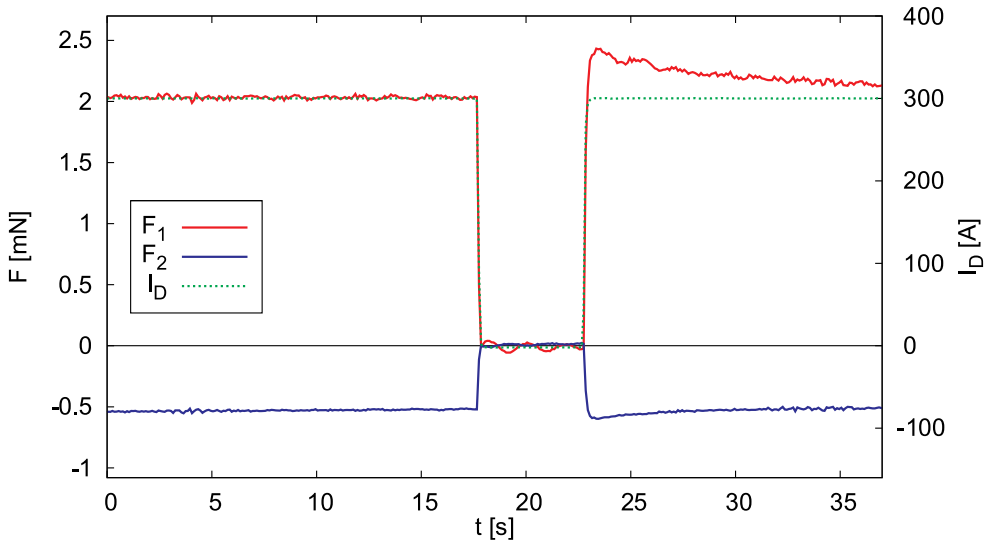

Figure 4.27: Measurement of the pressure forces F_1 and F_2 exerted on the two heads of the current-force probe by the plasma. The discharge is temporally switched off during 17 s $\leq t \leq$ 22 s (green curve: discharge current).

blue curves) follow the discharge current (dashed green curve) in general very well. However, when the plasma is switched on again, the force is slightly higher than before switching off. This is due to the temperature decrease of the cathode during the off period which causes a higher discharge voltage and therefore a larger discharge power. In order to be able to compare the data, the pressure force and the current-voltage characteristics are always measured before switching off the plasma.
Tab. 4.2 shows the quantities measured by the current-force probe and with LIF for eight different discharge conditions, where F_1,F_2,n_{se1},n_{se2},T_{e1} and T_{e2} are determined by the former and T_i by the latter[8]. From this data the pressure forces were evaluated and plotted in Fig. 4.28. Fig. 4.28(a) shows the comparison of F/A_p with $n_{se}(m_i c_s^2 + T_e + T_i + |u_n| c_s m_i)$. The red and the magenta colored curves and the blue and the cyan colored curves are clearly different.
The most likely explanation for this is that the two probe heads affect each other by an additional internal repulsive force F_{int}. Due to action = reaction F_{int} affects the heads symmetrically and so the measured forces F_1 and F_2 are related to the actual pressure forces F_{p1} and F_{p2} by

$$F_1 = F_{p1} - F_{int} \text{ and } F_2 = F_{p2} + F_{int} \ . \tag{4.101}$$

[8]The ion temperature was measured when the probe was removed from the plasma.

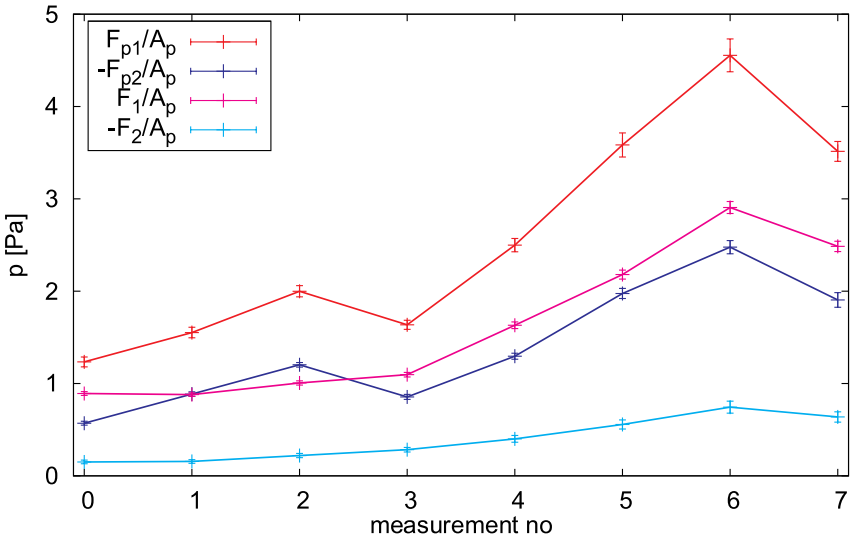

(a) Comparison of the plasma pressure forces F_{p1} and F_{p2} affecting the two heads (1) and (2) determined from the electrical and the LIF measurements with the mechanical force measurement of F_1 and F_2.

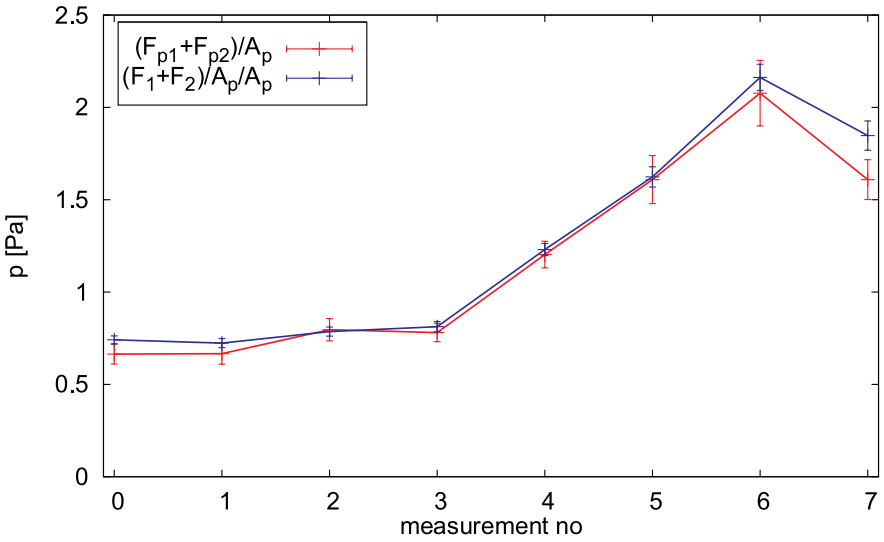

(b) Comparison of the sum forces $F_{p1} + F_{p2}$ and $F_1 + F_2$.

Figure 4.28: Measurements with the current-force probe and with LIF.

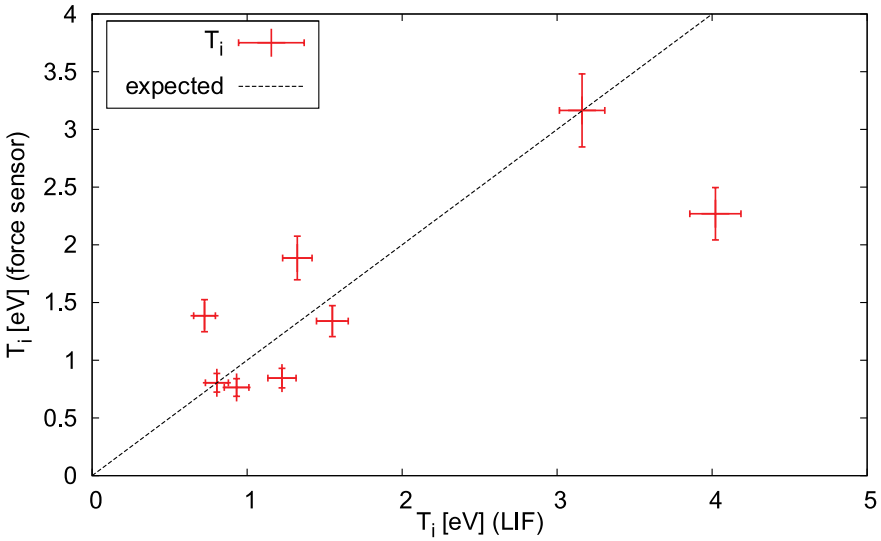

Figure 4.29: Ion temperature evaluated from the current-force probe and those measured by LIF.

Note that F_{p2} is negative since the force affects the second probe head in the opposite direction to F_{p1}. We will discuss in Sec. 4.7.4 what might be the reason for this repulsive force. Although a possible effect can be identified there, up to now we cannot quantify accurately the value of F_{int} and so we have to accept that we cannot say much about the individual forces F_{p1} and F_{p2} for the moment. However, we can determine the total force on the two heads by adding the signals

$$F \equiv F_{p1} + F_{p2} = F_1 + F_2 \ , \tag{4.102}$$

since this total force is not influenced by F_{int}. Fig. 4.28(b) shows that in this case the electrical, the LIF and the force measurements agree quite well.

4.7.3 Ion temperature

As aforementioned the motivation for investigating the current-force probe was its possible application as an ion sensitive probe. If we knew F_p, T_e and I_{sat} (and u_n) of a single probe head, we would be able to determine unambiguously T_i from Eq. 4.100. However, as we lost the information about the individual forces F_{p1} and F_{p2} we need to make an additional assumption, $T_{i1} = T_{i2} = T_i$, in order to make use of the measured data. We express the two forces in Eq. 4.102 by Eq. 4.100, substitute c_s and I_{sat} by means of

Eq. 4.29 and Eq. 4.38 and obtain an equation that contains T_i as the only unknown variable

$$F_1 + F_2 = \frac{A_p\sqrt{m_i}}{eA_c}\left[|I_{sat1}|\left(\frac{2T_{e1}+(1+\gamma_i)T_i}{\sqrt{T_{e1}+\gamma_i T_i}}+u_{n1}\sqrt{m_i}\right)-\right.$$
$$\left.|I_{sat2}|\left(\frac{2T_{e2}+(1+\gamma_i)T_i}{\sqrt{T_{e2}+\gamma_i T_i}}+u_{n2}\sqrt{m_i}\right)\right] . \qquad (4.103)$$

Resolving this with respect to T_i yields extremely long expressions which are not shown here for the sake of brevity. Here, it is only important to note that the value of T_i can be determined unambiguously (*e.g.* numerically) from Eq. 4.103.
In Fig. 4.29 this was done for the eight sets of F_j,$T_{e,j}$ and $I_{sat,j}$ shown in Tab. 4.2 (y axis). The results are compared again with the T_i values measured by LIF (x axis). $\gamma_i = 1.2$ was chosen and a slightly larger escaping velocity of the neutrals of the first head was assumed ($u_{n1} = 500$ m/s and $u_{n2} = 400$ m/s) in order to fit the data. As seen in the figure, a reasonable agreement is achieved between the two techniques. However, due to the uncertainties of the different quantities the force depends on (*e.g.* γ_i), we can hardly rely on this device as a robust diagnostics. Nevertheless, it was shown that such a device could work in principle, given that the repulsive force between the two heads is either suppressed and/or completely understood. In contrast to other ion sensitive probes, like Katsumata probes [30], Plug probes [13] or Retarding field analyzers [49]), the probe is not as sensitive to strength and orientation of the magnetic field.
The mechanical properties of the pendulum can be studied with sufficient accuracy to reconstruct changes of the force faster than the oscillation frequency of the pendulum (about 100 ms). This was of particular importance in [45] where a similar probe was tested in the tokamak ISTTOK in Lisbon, since the duration of the plasma pulses in this device is about 30 ms only.

4.7.4 Forces between the two heads

We want to address now the question of what produces a repulsive force between the two probe heads. Probably the first candidate that comes into mind is an electrostatic repulsion due to charges that might accumulate on the heads. Indeed in the electrostatic sheaths in front of the probe head surfaces, a number of the order 10^{10} elementary charges accumulate. We can compute the exact amount of charge integrating ρ over the sheath

$$Q_s(n_e, T_e, T_i) = A_p \int_{se}^{w} \rho(\Phi) dz = \epsilon_0 A_p \left(E_w - E_{se}\right) , \qquad (4.104)$$

where in the last step Poisson's equation (4.7) was applied. The electric field at the sheath edge E_{se} is usually orders of magnitude smaller than that at the wall E_w and can therefore be neglected. We can compute the electric field at the wall analytically by multiplying Eq. 4.35 by $d\Phi/dz$ (choosing $\Phi_{se} = 0$) and integrating over z. An analytic expression for Q_s is then obtained

$$Q_s = A_p \sqrt{2 n_{se} \epsilon_0 \left[T_e \left(\exp\left(\frac{eU_f}{T_e} \right) - 1 \right) + m_i c_s^2 \left(\sqrt{1 - \frac{2eU_f}{m_i c_s^2}} - 1 \right) \right]} \,, \tag{4.105}$$

where the floating potential $U_f = U_f(n_e, T_e, T_i)$ is given by Eq. 4.37 with $\Phi_{se} = 0$. The repulsive force between (only) these charges in the two sheaths in front of the probe heads can be estimated by

$$F_{es} = \eta \frac{Q_{s1} Q_{s2}}{2\epsilon_0 A} \tag{4.106}$$

which is basically the formula for the force between two capacitor plates. η is a factor $0 < \eta \leq 1$ that takes into account the finite distance d between the sheaths. If η was about 0.9 this could explain the observation very well. However, this consideration is wrong. The positive charge contained in the sheath can only be kept so close together, since (almost) the same amount of negative charge is located in a thin layer underneath the probe head surface. The dipole field created by these two layers has a very short range and should be practically zero in a few mm distance. The amount of charge contained in the probe head should be about $Q = C_{PH} U_f \approx 10^7$ e, where $C_{PH} \approx 0.2$ pF is the capacity of the probe head.

Since it was carefully checked that there was no mechanical interaction between the two pendulums, the most likely explanation is that plasma penetrates into the small space between the heads (about 3 mm). Fig. 4.30(b) (right) shows the probe head (actually a former version where the two heads were in a distance of about 5 mm) in a xenon discharge. Between the heads the light emission is even stronger than in the plasma bulk. Furthermore, it was found that the rear sides of the probe were covered by a black-silver coating (cf. Fig. 4.30(b) (left)), an indication that, in fact, material is transported into this volume.

From the measurements we can estimate that the internal force F_{int} is approximately proportional to F_{p1} with

$$|F_{int}| = 0.3 F_{p1} \,. \tag{4.107}$$

At first view this value seems to be surprisingly high. However, if we assume as a simple model that the pressure in the space between the two probe

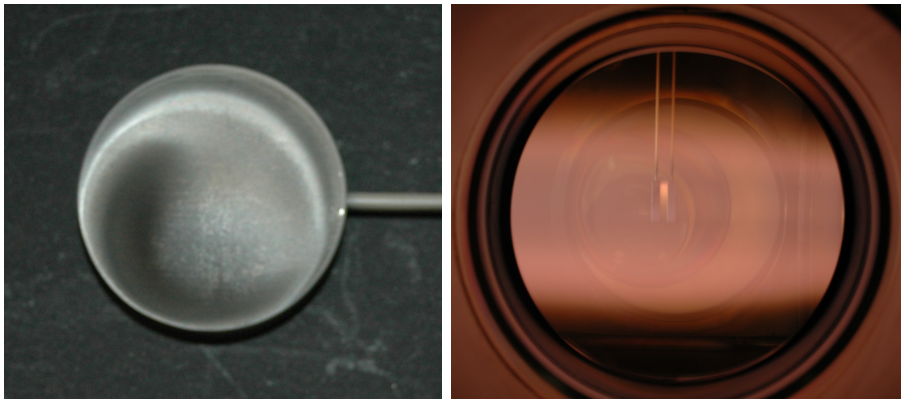

(a) Coating of the probe heads. (b) Probe heads in a xenon discharge.

heads has an exponential decay $p(r) = p_0 \exp\left(-\frac{ro-r}{\lambda_p}\right)$, where r_0 is the probe radius, and that the pressure on the front side of the head is also p_0, we can compute the penetration length λ_p according to

$$0.3 = \frac{2\pi \int_0^{r_0} p_0 \exp\left(-\frac{ro-r}{\lambda_p}\right) r dr}{2\pi \int_0^{r_0} p_0 r dr} = \frac{2\lambda_p^2}{r_0}\left(\exp\left(-\frac{ro}{\lambda_p}\right) - 1\right) + \frac{2\lambda_p}{r_0} \quad (4.108)$$

which yields a value of about $\lambda_p = 3$ mm. In view of the large diffusion coefficient found in Eq. 4.3 ($D = 20$ m^2/s) this does not seem to be an unrealistic value.

Chapter 5

Summary

In order to carry out the measurements shown in Chapter 4 a completely new laser induced fluorescence (LIF) diagnostic system was arranged. The experimental difficulties which had to be overcome to run this diagnostics were described in Chapter 2.
Expectations concerning the possible spatial resolution of this new LIF diagnostics were clearly surpassed. While in [42, 44] the spatial resolution was about $\Delta z = 50$ mm, in Sec. 4.4 we saw that the LIF signal could still be detected unambiguously at a spatial resolution three orders of magnitude better, *i.e.* $\Delta z = 50$ μm.

With this diagnostic improvement the ion velocity distribution was measured as a function of the distance to a target surface under different conditions. In all cases the streaming velocity u_i attains at least the speed of sound c_s at the closest position to the surface. According to my knowledge this is the first direct experimental proof of the Bohm criterion under fusion relevant plasma conditions.

Another remarkable result is the short scale length on which the final acceleration to the speed of sound takes place. In the case of the large target this characteristic length was about $\lambda_M = 30$ mm. Since this is much shorter than the spatial resolution in [42, 44] it becomes clear, why Mach numbers $M = u_i/c_s$ of only about 0.5 were found there. A model, which takes sources, charge-exchange and elastic collisions as well as cross-field diffusion into account was finally able to explain the observation (cf. Sec. 4.2). The agreement, however, could only be achieved by assuming a rather low temperature ($T_n \approx 400$ K) of the neutrals.

Motivated in particular by its relevance to fusion research, the plasma-wall

transition in front of a turnable tungsten target (also large) was investigated too (Sec. 4.5). Mach number and density profiles were measured for different incidence angles of the magnetic field lines. As predicted by Chodura [10], supersonic streaming velocities are found in the 'magnetic presheath' in front of the plate. While the Mach numbers in the immediate vicinity of the surface are predicted fairly well by the Chodura model, the extension of the 'magnetic presheath' was found to be significantly shorter. Numerical calculations were carried out taking into account sources and collisions. In contrast to the situation without these additional terms, the critical Mach number at the edge of the magnetic presheath can then be different to unity. Mach numbers around 3.5, as predicted for the estimated ionization and collision frequencies, however, were not observed in the experiment.

In addition to the situation where practically the whole plasma streams onto such 'large' targets, the plasma-wall transition in front of a 'small' target was investigated. This situation has to be described by a significantly different model, one, which takes into account the particle and momentum diffusion into the plasma volume perturbated by the target.
The scale length, where the Mach number increases from $M \approx 0.5$ to unity, was found to be even smaller, $\lambda_M = 5$ mm. Since the closest position to the target measured by Gulick *et al.* [23] was $z = -5$ mm this explains why these authors were unable to observe this 'sudden acceleration', which led them to infer a violated Bohm criterion.
The measured Mach numbers and densities were compared to the presheath-model set up by Hutchinson[27]. An excellent agreement is achieved when assuming a cross-field transport coefficient as high as $D = 20$ m^2/s. It appears unrealistic to explain such a high value of D by true diffusion. Taking into account ionization and collisional friction in the modeling the profiles slightly change but a realistic diffusion coefficient of $D = 1$ m^2/s is in clear disagreement with the data. A Monte Carlo particle simulation as well as simple fluid models showed that part of this enhanced cross-field transport is driven by the radial electric fields that build up in front of the target. However, the computed flux is still too small to explain the profiles completely. It is likely that dynamic effects, such as drift waves, have to be taken into account as well.
Nevertheless it is shown in Sec. 4.3 that the Mach number can be derived fairly well from the ratio of saturation currents (Eq. 4.57). However, caution has to be taken, when the mean free path length for ionization becomes sufficiently small that recycling plays a dominant role. It was shown experimentally in Sec. 4.6 that Eq. 4.57 might be violated under these conditions.
In Sec. 4.7 we saw that the forces F_1 and F_2 that affect the two probe heads of the current-force probe can be measured in a plasma discharge. However, we were not yet able to determine unambiguously the individual plasma pressure forces F_{p1} and F_{p2} on the (the front side of) each head, due to an

unknown internal force between them. Nevertheless, we could deduce the ion temperature T_i from the sum force $F_1 + F_2 = F_{p1} + F_{p2}$ (and the current measurement) since this is not affected by this internal force. Although this proof-of-principle as an ion sensitive probe was successful we cannot yet rely on such a device as a robust diagnostics for T_i.

5.1 Outlook

Due to the extensive experimental preparations, the demanding vacuum conditions, and the long acquisition cycles the LIF measurements were very time consuming. For this reason only selected situations could be investigated. In this section some examples are given what else could be done in future experiments and what improvements could be made.

First, it would be interesting to measure the high transport coefficient of $D = 20$ m^2/s directly, instead of obtaining this quantity from a presheath model. In order to do so it would be necessary to launch the laser beam vertically into the target chamber through a window at the bottom of the machine. Measuring the ion velocity distribution at different radial positions the radial flux density $\Gamma_\perp = nv_\perp$ and the radial density gradient $\nabla_\perp n$ can then be determined. The relation $\Gamma_\perp = -D\nabla_\perp n$ then yields directly the value of D. If D is actually of the order 20 m^2/s this effect should be clearly observable.

Without any modifications of the experimental arrangement, the plasma-wall transition can be investigated in a plasma composed of different ion species. This would answer the question of whether the findings concerning the multi ion-species Bohm criterion (Eq. 4.31) in [57, 71, 39] also hold for high density plasmas.

The measurements in Sec. 4.7 with respect to the current-force probe could be improved by modifying the probe heads such that the radial flux of plasma into the space between the probe heads is avoided. Furthermore a completely different target should be used for the measurements described in Sec. 4.4, one, which is fixed rigidly to the target chamber.

Finally it would be desirable to reduce the Zeeman effect. As it is not possible to reduce the magnetic field significantly in PSI-2, the only possible way to do so is to suppress either the $\Delta M_j = +1$ or the $\Delta M_j = -1$ components (cf. Fig. 3.6). For this purpose it would be necessary to polarize the light circularly.

Concerning the modeling of the plasma streaming onto a large target it would be desirable to apply a two dimensional fluid code like 'B2' in combination with a Monte Carlo model like 'Eirene'. Such a comparison with the modeling would also be a benchmark for these codes.

Bibliography

[1] Anders, A.: *A Formulary for Plasma Physics*. Berlin : Akademie-Verlag, 1990

[2] Baudach, M. ; Welzel, S. ; Krenz, G. ; Markin, A.: Decomposition measurements of hydrocarbons in PSI-II. (2006), P-5.161. http://crpppc42.epfl.ch/Roma/pdf/P5_161.pdf. – 33rd EPS Conference on Plasma Physics, Rome/Italy

[3] Bohm, D.: *The Characteristics of Electrical Discharges in Magnetic Fields*. Mc Graw-Hill, New York, 1949. – 77–86 S.

[4] Bohmeyer, W. ; Markin, A. ; Koch, B. ; Krenz, G. ; Fussmann, G.: Study of Gas Balance by Injection of Hydrocarbons into the Plasma Generator PSI-2. In: *AIP Conference Proceedings, Opole/Poland* 812 (2005), September, S. 215–218

[5] Bohmeyer, W. ; Markin, A. ; Naujoks, D. ; Koch, B. ; Krenz, G. ; Baudach, M. ; Fussmann, G.: Decomposition and sticking of hydrocarbons in the plasma generator PSI-2. In: *Journal of Nuclear Materials* 363–365 (2007), June, 127–130. http://dx.doi.org/10.1016/j.jnucmat.2007.01.163

[6] Bohmeyer, W. ; Naujoks, D. ; Markin, A. ; Arkhipov, I. ; Koch, B. ; Schröder, D. ; Fussmann, G.: Transport and deposition of injected hydrocarbons in plasma generator PSI-2. In: *Journal of Nuclear Materials* 337–339 (2005), March, 89–93. http://dx.doi.org/10.1016/j.jnucmat.2004.10.107

[7] Braams, B.J.: *Computational studies in tokamak equilibrium and transport*. Utrecht, Rijksuniversitet Utrecht, Diss., 1986

[8] Brix, M.: *Messung von Elektronentemperatur und -dichte mittels Heliumstrahldiagnostik im Randschichtplasma eines Tokamaks*. Bochum, Ruhr Universität, Diss., 1998

[9] Chavers, D.G. ; Chang-Díaz, F.R.: Momentum flux measuring instrument for neutral and charged particle flows. In: *Review of Scientific Instruments* 73 (2002), 10, Nr. 10, 3500–3507. http://dx.doi.org/10.1063/1.1505107

[10] Chodura, R.: Plasma-wall transition in an oblique magnetic field. In: *Physics of fluids* 25 (1982), Nr. 9, 1628–1633. http://dx.doi.org/10.1063/1.863955

[11] Claire, N. ; Bachet, G. ; Stroth, U. ; Doveil, F.: Laser-induced-fluorescence observation of ion velocity distribution functions in a plasma sheath. In: *Physics of Plasmas* 13 (2006), June, 062103. http://dx.doi.org/10.1063/1.2206786

[12] Coster, David P.: *Tokamak divertor modeling with fluid and kinetic codes*. Princeton, Princeton University, Diss., 1993. http://www.rzg.mpg.de/~dpc/thesis_single.pdf

[13] Demidov, V.I. ; Raynskaia, S.V. ; Rypdal, K.: Electric probes for plasmas: The link between theory and instrument. In: *Review of Scientific Instruments* 73 (2002), Nr. 10, 3409–3439. http://dx.doi.org/10.1063/1.1505099

[14] Demtröder, W.: *Laserspektroskopie*. 4th. Berlin, Heidelberg, New York : Springer-Verlag, 2000

[15] Emmert, G.A. ; Wieland, R.M. ; Mense, A.T. ; Davidson, J.N.: Electric sheath and presheath in a collisionless, finite ion temperature plasma. In: *Physics of Fluids* 23 (1980), April, 803–812. http://dx.doi.org/10.1063/1.863062

[16] Fastie, W. G.: Image forming properties of the Ebert monochromator. In: *J. Opt. Soc. Am.* 42 (1952), S. 647

[17] Fussmann, G ; Baudach, M. ; Bohmeyer, W. ; Koch, B. ; Krenz, G. ; Markin, A. ; Naujoks, D. ; Lunt, T. ; Waldmann, O. ; Welzel, S.: Studies of Hydrocarbon Formation and Redeposition in ITER-Relevant Divertor Chamber Conditions / European Fusion Development Agreement (EFDA), Task: Erosion and Redeposition in ITER, Technology Task TW4-TPP-TRIDEP. Version: 2006. http://plasma.physik.hu-berlin.de/publications/EFDA_report2006.pdf. 2006. – Forschungsbericht. – 1–81 S.

[18] Fussmann, G. ; Bohmeyer, W. ; Kiss'ovski, Zh. ; Koch, B.: Flow of Magnetized Plasma in a Linear Device. In: *AIP Conf. Proc.,ICPP2002* 669 (2003), June, 149–153. http://dx.doi.org/10.1063/1.1593888

[19] Goeckner, M.J. ; Goree, J.: Laser-induced fluorescence measurement of plasma ion temperature: Corrections for power saturation. In: *Journal of Vacuum Science & Technology A* 7 (1989), May, S. 977–981

[20] Goeckner, M.J. ; Goree, J. ; Sheridan, T.E.: Measurements of ion velocity and density in the plasma sheath. In: *Phys. Fluids B* 4 (1992), June, 1663–1670. http://dx.doi.org/10.1063/1.860074

[21] Griem, H.R.: *Spectral Line Broadening by Plasmas*. 1st. New York and London : Academic Press, 1974

[22] Griem, H.R.: *Principles of Plasma Specroscopy*. 1st. Cambridge : Cambridge University Press, 1997

[23] Gulick, S.L. ; Stansfield, B.L. ; Abou-Assaleh, Z. ; Boucher, C. ; Matte, J.P. ; Johnston, T.W. ; Marchand, R.: Measurement of pre-sheath flow velocities by laser-induced fluorescence. In: *Journal of Nuclear Materials* 176 & 177 (1990), December, 1064–1069. http://dx.doi.org/10.1016/0022-3115(90)90192-P

[24] Harrison, E.R. ; Thompson, W.B.: Harrison-Thompson Generalization of Bohm's Sheath Condition. In: *Proceedings of the Physical Society* 80 (1962), July, 309–311. http://dx.doi.org/10.1088/0370-1328/80/1/137

[25] Hodgkinson, D.P. ; Briggs, J.S.: Resonant charge exchange at low velocities. In: *Journal of Physics B: Atomic and Molecular Physics* 9 (1976), 255–267. http://dx.doi.org/10.1088/0022-3700/9/2/013

[26] Hornbeck, J.A.: Charge Transfer and the Mobility of Rare Gas Ions. In: *Journal of Physical Chemistry* 56 (1952), 829–831. http://dx.doi.org/10.1021/j150499a003

[27] Hutchinson, Ian H.: Ion collection by probes in strong magnetic fields with plasma flow. In: *Physical Review A* 37 (1988), Nr. 11, 4358–4366. http://link.aps.org/abstract/PRA/v37/p4358

[28] Hutchinson, I.H.: *Principles of Plasma Diagnostics*. Cambridge : Press Syndicate of the University of Cambridge, 1987

[29] Kastelewicz, H. ; Fussmann, G.: Plasma Modelling for the PSI Linear Plasma Device. In: *Contributions to Plasma Physics* 44 (2004), 352–360. http://dx.doi.org/10.1002/ctpp.200410053

[30] Katsumata, I. ; Okazaki, M.: Ion Sensitive Probe-A New Diagnostic Method for Plasma in Magnetic Fields. In: *Japanese Journal of Applied Physics* 6 (1967), January, Nr. 1, 123–124. http://dx.doi.org/10.1143/JJAP.6.123

[31] Klose, S.: *Untersuchung der Driftinstabilität an der rotierenden magnetisierten Plasmasäule des PSI-1 im Falle eines Plasmahohlprofils und großer endlicher Ionengyroradieneffekte*. Berlin, Humboldt Universität, Diss., 2000. http://nbn-resolving.de/urn:nbn:de:kobv:11-10012808

[32] Klose, S. ; Bohmeyer, W. ; Laux, M. ; Meyer, H. ; Fussmann, G. ; PSI-Team: Investigation of ion drift waves in the PSI-2 using Langmuir-probes. In: *Contributions To Plasma Physics* 41 (2001), Nr. 5, 467–472. http://dx.doi.org/10.1002/1521-3986(200109)41:5<467::AID-CTPP467>3.0.CO;2-X

[33] Koch, B.: *Angular Resolved Measurements of Particle and Energy Fluxes to Surfaces in Magnetized Plasmas*. Berlin, Humboldt Universität, Diss., 2004. http://nbn-resolving.de/urn:nbn:de:kobv:11-10034619

[34] Koch, B. ; Bohmeyer, W. ; Fussmann, G.: Angular dependence of the floating potential in a magnetized plasma. In: *Journal of Nuclear Materials* 313–316 (2003), March, 1114–1118. http://dx.doi.org/10.1016/S0022-3115(02)01547-7

[35] Koch, B. ; Bohmeyer, W. ; Fussmann, G.: Angular dependence of energy and particle fluxes in a magnetized plasma. In: *Journal of Nuclear Materials* 337–339 (2005), March, 211–215. http://dx.doi.org/10.1016/j.jnucmat.2004.10.028

[36] Kornejew, P.: *Bestimmung der Elektronenparameter in Randschichtplasmen unter Verwendung eines thermischen Heliumstrahls*. Berlin, Humboldt Universität, Diss., 1996

[37] Kornejew, P ; Bohmeyer, W ; Reiner, H.D.: Measurements of Chemical Erosion in the Plasmagenerator PSI-1. In: *Physica Scripta* (1999), 40–42. http://dx.doi.org/10.1238/Physica.Topical.081a00040

[38] Kornejew, P ; Bohmeyer, W ; Reiner, H.D. ; Wu, C.H.: Chemical erosion of CFC at high ion flux densities. In: *Physica Scripta* (2001), 29–32. http://dx.doi.org/10.1238/Physica.Topical.091a00029

[39] Lee, D. ; Hershkowitz, N.: Measurements of Ar^+ and Xe^+ velocities near the sheath boundary of Ar-Xe plasma using two diode lasers. In: *APPLIED PHYSICS LETTERS* 91 (2007), July, 041505. http://dx.doi.org/10.1063/1.2760149

[40] Lieberman, M.A. ; Lichtenberg, A.J.: *Principles of Plasma Discharges and Materials Processing*. Bd. 1. 1st. New York, NY : John Wiley & Sons, Inc., 1994

[41] Lotz, W.: Electron-impact ionization cross-sections for atoms up to Z=108. In: *Zeitschrift für Physik A Hadrons and Nuclei* 232 (1970), April, Nr. 2, 216-241. http://dx.doi.org/10.1007/BF01393132

[42] Lunt, T.: *Experimental Investigation on the Bohm Criterion Behind a Magnetic Laval Nozzle*. Berlin, Humboldt Universität, Diploma thesis, 2003

[43] Lunt, T. ; Calderón, E. ; Fussmann, G. ; Hidalgo, C. ; Pedrosa, M.A.: Ion temperature measurements by means of a combined force - Mach - Langmuir probe. In: *32th EPS Conference on Plasma Physics, 27 June - 1 July 2005, Tarragona, Spain*. Tarragona, Spain : European Physical Society, June 2005

[44] Lunt, T. ; Ezumi, N. ; Bohmeyer, W. ; Fussmann, G.: Experimental investigations with respect to the applicability of the Bohm criterion. In: *Journal of Nuclear Materials* 337–339 (1997), 201–205. http://dx.doi.org/10.1016/j.jnucmat.2004.10.147

[45] Lunt, T. ; Silva, C. ; Fernandes, H. ; Hidalgo, C. ; Pedrosa, M.A. ; Duarte, P. ; Figueiredo, H. ; Pereira, T.: Edge plasma pressure measurements using a mechanical force sensor on the tokamak ISTTOK. In: *Plasma Physics and Controlled Fusion* 49 (2007), September, 1783–1790. http://dx.doi.org/10.1088/0741-3335/49/11/003

[46] Meyer, H. ; Klose, S. ; Pasch, E. ; Fussmann, G.: Plasma rotation in a plasma generator. In: *Physical Review E* 61 (2000), Nr. 4, 4347–4356. http://dx.doi.org/10.1103/PhysRevE.61.4347

[47] Meyer, Hendrik: *Analyse der Plasmarotation in einer linearen Magnetfeldkonfiguration*. Berlin, Humboldt Universität, Diss., 1998

[48] Oksuz, L. ; Hershkowitz, N.: Plasma, presheath, collisional sheath and collisionless sheath potential profiles in weakly ionized, weakly collisional plasma. In: *Plasma Sources Science and Technology* 14 (2005),

February, 201-208. http://dx.doi.org/10.1088/0963-0252/14/1/022

[49] Pitts, R.A. ; I.Duran ; Erents, S.K. ; J.Horacek ; Matthews, G.F.: Retarding Field Analyser Measurements in the JET Plasma Boundary. In: *30th EPS Conference on Contr. Fusion and Plasma Phys.* Bd. 27A, P-2.84. St.Petersburg : European Physical Society, 7 2003

[50] Pots, B.F.M.: *Turbulence And Transport in a Magnetized Argon Plasma*. Eindhoven, TU, Diss., 1979

[51] P.Schef ; A.Derkatch ; P.Lundin ; S.Mannervik ; L.-O.Norlin ; D.Rostohar ; P.Royen ; E.Bi´emont: Lifetimes of metastable levels in Ar II. In: *The European Physical Journal D* 29 (2004), 195–199. http://dx.doi.org/10.1140/epjd/e2004-00043-1

[52] Pullins, S.H. ; Dressler, R.A. ; Torrents, R. ; Gerlich, D.: Guided-Ion Beam Measurements of Ar^+ + Ar Symmetric Charge-transfer Cross Sections at Ion Energies Ranging from 0.2 to 300 eV. In: *Zeitschrift für Physikalische Chemie* 214 (2000), S. 1279–1297

[53] Ralchenko, Yu. ; Jou, F.-C. ; Kelleher, D.E. ; Kramida, A.E. ; Musgrove, A. ; Reader, J. ; Wiese, W.L. ; Olsen, K.: *NIST Atomic Spectra Database (version 3.0)*. Version 3.0.2. Online, 2005. – http://physics.nist.gov/asd

[54] Riemann, K.U.: Theory of the Plasma-Sheath Transition. In: *Journal of Technical Physics* 41, Special Issue (2000), S. 89–121

[55] Saha, B. ; Fritzsche, S.: M1 and E2 transitions in Ar II. In: *Journal of Physics B: Atomic, Molecular and Optical Physics* 38 (2005), 1161–1171. http://dx.doi.org/10.1088/0953-4075/38/8/007

[56] Saloman, E. B. ; Sansonetti, C. J.: Wavelengths, Energy Level Classifications, and Energy Levels for the Spectrum of Neutral Neon. In: *J. Phys. Chem. Ref. Data* 33 (2004), S. 1113

[57] Severn, G.D. ; Wang, X. ; Ko, E. ; Hershkowitz, N. ; Turner, M.M. ; McWilliams, R.: Ion flow and sheath physics studies in multiple ion species plasmas using diode laser based laser-induced fluorescence. In: *Thin Solid Films* 506–507 (2006), May, 674–678. http://dx.doi.org/10.1016/j.tsf.2005.08.114

[58] Sheridan, T.E. ; Goree, J.A.: Analytic Expression For the Electric Potential in the Plasma Sheath. In: *IEEE Transactions on Plasma Science* 17 (1989), 12, Nr. 6, S. 884–888

[59] Smirnov, B.M.: *Physics of Weakly Ionized Gases*. Moscow : Mir Publishers, 1981. – 253 S.

[60] Sobelman, I.I.: *Atomic Spectra and Radiative Transitions*. Bd. 1. 2nd. Berlin, Heidelberg, New York : Springer Verlag, 1992. – 193 S.

[61] Stangeby, P.C.: Measuring plasma drift velocities in tokamak edge plasmas using probes. In: *Physics of Fluids* 27 (1984), 2699–2704. http://dx.doi.org/10.1063/1.864573

[62] Stangeby, P.C.: *The Plasma Boundary of Magnetic Fusion Devices*. 1st. London : Institue of Physics Publishing, 2000 (Plasma Physics Series)

[63] Stark, Albrecht: *Ion dynamics in magnetized plasmas*. Greifswald, Ernst-Moritz-Arndt-Universit¨at Greifswald, Diss., 2006

[64] Versteegh, A.: *Analysis of a Long Living Atmospheric Plasmoid*. Eindhoven, Technische Universiteit Eindhoven, Factulteit Technische Natuurkunde, diploma thesis, 11 2007

[65] Vestal, M.L. ; Blakley, C.R. ; Futrell, J.H.: Crossed-beam measurements of differential cross-sections for elastic scattering and charge exchange in low energy Ar^--Ar collisions. In: *Physical Review A* 17 (1978), Nr. 4, 1337–1342. http://dx.doi.org/10.1103/PhysRevA.17.1337

[66] Waelbroeck, F. ; Leloup, C. ; Poffé, J.P. ; Evrard, P. ; Der Agobian, R. ; Véron, D.: Electrodeless Plasma Gun. In: *Nuclear Fusion* (1962), Nr. Supplement, Part 2, S. 675–685

[67] Waldmann, O. ; Fussmann, G.: Influence of the Langmuir probe shaft on measuring plasma parameters. In: *7th International Workshop on Electrical Probes in Magnetized Plasmas*. Prague : European Physical Society, July 2007. – Talk. Accepted for publication in Contributions to Plasma Physics.

[68] Waldmann, O. ; Fussmann, G.: Ion mass spectrometry in a magnetized plasma. In: *34th European Physical Society Conference on Plasma Physics, Warsaw, Poland*. Warsaw, Poland : European Physical Society, July 2007, P5.108. – Poster

[69] Waldmann, O. ; Koch, B. ; Fussmann, G.: Langmuir Probe Measurements in Plasma Shadows. (2005), September. http://link.aip.org/link/?APCPCS/812/443/1. – International Conference PLASMA 2005 combined with 3rd German-Polish Conference on Plasma Diagnostics for Fusion and Applications and French-Polish on Thermal Plasma in Space and Laboratory. AIP Conference Proceedings Vol. 812, Opole/Poland

[70] Waldmann, O. ; Meyer, H. ; Fussmann, G.: Anomalous Diffusion in a Linear Plasma Generator. In: *Contributions to Plasma Physics* 47 (2007), 691–702. http://dx.doi.org/10.1002/ctpp.200710079

[71] Wang, X. ; Hershkowitz, N.: Experimental studies of the two-ion species flow in the plasma presheath. In: *Physics of Plasmas* 13 (2006), May, 053503. http://dx.doi.org/10.1063/1.2193927

[72] Wischmeier, M.: *Simulating Divertor Detachment in the TCV and JET Tokamaks.* Lausanne, École Polytechnique Fédérale de Lausanne, Diss., 2004. http://biblion.epfl.ch/EPFL/theses/2004/3176/3176_abs.pdf

Appendix A

Tables

i	level	E_i [eV]	n_I	n_{II}	n_{III}
0	$3s^2 3p^5 [^2P]_{3/2}$	0.0000000	1.000	0.992	0.754
1	$3s^2 3p^5 [^2P]_{1/2}$	0.1774937	$2.6 \cdot 10^{-4}$	$7.8 \cdot 10^{-3}$	0.215
2	$3s^2 3p^6 [^2S]_{1/2}$	13.4797506	$2.1 \cdot 10^{-8}$	$5.7 \cdot 10^{-7}$	$2.1 \cdot 10^{-5}$
3	$3d\ ^4D_{7/2}$	16.4065018	$4.7 \cdot 10^{-9}$	$5.4 \cdot 10^{-7}$	$3.7 \cdot 10^{-5}$
4	$3d\ ^4D_{5/2}$	16.4255753	$3.8 \cdot 10^{-9}$	$4.1 \cdot 10^{-7}$	$2.8 \cdot 10^{-5}$
5	$3d\ ^4D_{3/2}$	16.4441128	$2.9 \cdot 10^{-9}$	$2.8 \cdot 10^{-7}$	$1.9 \cdot 10^{-5}$
6	$3d\ ^4D_{1/2}$	16.4573765	$1.6 \cdot 10^{-9}$	$1.5 \cdot 10^{-7}$	$10.0 \cdot 10^{-6}$
7	$4s\ ^4P_{5/2}$	16.6438541	$9.6 \cdot 10^{-10}$	$7.3 \cdot 10^{-8}$	$4.8 \cdot 10^{-6}$
8	$4s\ ^4P_{3/2}$	16.7485275	$1.1 \cdot 10^{-9}$	$5.8 \cdot 10^{-8}$	$2.8 \cdot 10^{-6}$
9	$4s\ ^4P_{1/2}$	16.8124714	$2.1 \cdot 10^{-10}$	$1.3 \cdot 10^{-8}$	$1.3 \cdot 10^{-6}$
10	$4s\ ^2P_{3/2}$	17.1400261	$8.1 \cdot 10^{-10}$	$4.8 \cdot 10^{-8}$	$2.4 \cdot 10^{-6}$
11	$4s\ ^2P_{1/2}$	17.2658329	$1.5 \cdot 10^{-10}$	$9.3 \cdot 10^{-9}$	$9.1 \cdot 10^{-7}$
12	$3d\ ^4F_{9/2}$	17.6288548	$8.9 \cdot 10^{-10}$	$1.1 \cdot 10^{-7}$	$8.7 \cdot 10^{-6}$
13	$3d\ ^4F_{7/2}$	17.6946640	$1.4 \cdot 10^{-9}$	$1.2 \cdot 10^{-7}$	$7.0 \cdot 10^{-6}$
14	$3d\ ^4F_{5/2}$	17.7430897	$8.7 \cdot 10^{-10}$	$7.3 \cdot 10^{-8}$	$5.0 \cdot 10^{-6}$
15	$3d\ ^4F_{3/2}$	17.7757912	$3.7 \cdot 10^{-10}$	$3.5 \cdot 10^{-8}$	$3.4 \cdot 10^{-6}$
16	$3d\ ^2P_{1/2}$	17.9417496	$3.2 \cdot 10^{-10}$	$2.9 \cdot 10^{-8}$	$2.3 \cdot 10^{-6}$
17	$3d\ ^2P_{3/2}$	18.0606384	$3.5 \cdot 10^{-10}$	$3.7 \cdot 10^{-8}$	$3.8 \cdot 10^{-6}$
18	$3d\ ^4P_{1/2}$	18.2539501	$9.3 \cdot 10^{-11}$	$1.1 \cdot 10^{-8}$	$1.4 \cdot 10^{-6}$
19	$3d\ ^4P_{3/2}$	18.2880535	$1.6 \cdot 10^{-10}$	$2.0 \cdot 10^{-8}$	$2.1 \cdot 10^{-6}$
20	$3d\ ^4P_{5/2}$	18.3342800	$2.5 \cdot 10^{-10}$	$3.0 \cdot 10^{-8}$	$3.2 \cdot 10^{-6}$
21	$4s'\ ^2D_{3/2}$	18.4265480	$4.4 \cdot 10^{-11}$	$7.0 \cdot 10^{-9}$	$1.0 \cdot 10^{-6}$
22	$4s'\ ^2D_{5/2}$	18.4541130	$6.6 \cdot 10^{-11}$	$1.0 \cdot 10^{-8}$	$1.4 \cdot 10^{-6}$
23	$3d\ ^2F_{7/2}$	18.4958687	$1.8 \cdot 10^{-11}$	$9.9 \cdot 10^{-9}$	$4.0 \cdot 10^{-6}$
24	$3d\ ^2F_{5/2}$	18.6159420	$6.2 \cdot 10^{-11}$	$2.1 \cdot 10^{-8}$	$4.4 \cdot 10^{-6}$
25	$3d\ ^2D_{3/2}$	18.6565189	$1.3 \cdot 10^{-10}$	$2.4 \cdot 10^{-8}$	$3.7 \cdot 10^{-6}$
26	$3d\ ^2D_{5/2}$	18.7324390	$1.4 \cdot 10^{-10}$	$3.0 \cdot 10^{-8}$	$4.6 \cdot 10^{-6}$
27	$3d'\ ^2G_{9/2}$	19.1160679	$9.3 \cdot 10^{-11}$	$2.3 \cdot 10^{-8}$	$3.8 \cdot 10^{-6}$
28	$3d'\ ^2G_{7/2}$	19.1188602	$7.4 \cdot 10^{-11}$	$2.0 \cdot 10^{-8}$	$3.4 \cdot 10^{-6}$
29	$4p\ ^4P_{5/2}$	19.2229004	$1.9 \cdot 10^{-12}$	$3.9 \cdot 10^{-10}$	$2.5 \cdot 10^{-7}$
30	$4p\ ^4P_{3/2}$	19.2610836	$1.2 \cdot 10^{-12}$	$2.4 \cdot 10^{-10}$	$1.6 \cdot 10^{-7}$
31	$4p\ ^4P_{1/2}$	19.3053436	$8.8 \cdot 10^{-13}$	$1.4 \cdot 10^{-10}$	$8.3 \cdot 10^{-8}$
32	$4p\ ^4D_{7/2}$	19.4945335	$1.6 \cdot 10^{-12}$	$3.5 \cdot 10^{-10}$	$2.4 \cdot 10^{-7}$
33	$4p\ ^4D_{5/2}$	19.5490112	$2.0 \cdot 10^{-12}$	$3.3 \cdot 10^{-10}$	$1.8 \cdot 10^{-7}$
34	$4p\ ^4D_{3/2}$	19.6103058	$9.5 \cdot 10^{-13}$	$1.6 \cdot 10^{-10}$	$1.1 \cdot 10^{-7}$
35	$4p\ ^4D_{1/2}$	19.6425800	$3.2 \cdot 10^{-13}$	$5.8 \cdot 10^{-11}$	$5.5 \cdot 10^{-8}$
36	$4p\ ^2D_{5/2}$	19.6800480	$2.4 \cdot 10^{-12}$	$3.8 \cdot 10^{-10}$	$1.9 \cdot 10^{-7}$
37	$4p\ ^2D_{3/2}$	19.7622604	$1.2 \cdot 10^{-12}$	$1.9 \cdot 10^{-10}$	$1.2 \cdot 10^{-7}$
38	$4p\ ^2P_{1/2}$	19.8010845	$6.5 \cdot 10^{-13}$	$1.1 \cdot 10^{-10}$	$6.3 \cdot 10^{-8}$

Table A.1: Selected energy levels of the Ar^+ ion according to [53]. For all levels apart from 0,1,2 and 83 the notation introduced in Sec. 3 is used. The levels marked in red are metastable and the underlined levels are those used for LIF. The occupation densities for three different plasma conditions are given, I: $n_e = 5 \times 10^{17}$ m^{-3}, $T_e = 2$ eV, II: $n_e = 10^{18}$ m^{-3}, $T_e = 3.5$ eV, and III: $n_e = 10^{19}$ m^{-3}, $T_e = 6$ eV.

i	level	E_i [eV]	n_I	n_{II}	n_{III}
39	$4p\ ^2P_{3/2}$	19.8671551	$8.9 \cdot 10^{-13}$	$1.5 \cdot 10^{-10}$	$9.9 \cdot 10^{-8}$
40	$4p\ ^4S_{3/2}$	19.9674969	$5.3 \cdot 10^{-13}$	$1.1 \cdot 10^{-10}$	$8.0 \cdot 10^{-8}$
41	$4p\ ^2S_{1/2}$	19.9725361	$3.1 \cdot 10^{-13}$	$5.5 \cdot 10^{-11}$	$4.9 \cdot 10^{-8}$
42	$4s''\ ^2S_{1/2}$	20.7435455	$4.3 \cdot 10^{-12}$	$2.3 \cdot 10^{-9}$	$4.6 \cdot 10^{-7}$
43	$4p'\ ^2F_{5/2}$	21.1270313	$1.0 \cdot 10^{-13}$	$4.7 \cdot 10^{-11}$	$7.2 \cdot 10^{-8}$
44	$4p'\ ^2F_{7/2}$	21.1430740	$1.3 \cdot 10^{-13}$	$5.8 \cdot 10^{-11}$	$8.4 \cdot 10^{-8}$
45	$4p'\ ^2P_{3/2}$	21.3517990	$8.8 \cdot 10^{-14}$	$2.7 \cdot 10^{-11}$	$3.2 \cdot 10^{-8}$
46	$4p'\ ^2P_{1/2}$	21.4264889	$3.1 \cdot 10^{-14}$	$1.1 \cdot 10^{-11}$	$1.6 \cdot 10^{-8}$
47	$4p'\ ^2D_{3/2}$	21.4924011	$4.0 \cdot 10^{-14}$	$2.0 \cdot 10^{-11}$	$3.2 \cdot 10^{-8}$
48	$4p'\ ^2D_{5/2}$	21.4980488	$5.4 \cdot 10^{-14}$	$2.7 \cdot 10^{-11}$	$4.4 \cdot 10^{-8}$
49	$5s\ ^4P_{5/2}$	22.5148029	$4.3 \cdot 10^{-16}$	$3.8 \cdot 10^{-13}$	$1.7 \cdot 10^{-9}$
50	$5s\ ^4P_{3/2}$	22.5926628	$5.3 \cdot 10^{-16}$	$5.3 \cdot 10^{-13}$	$1.7 \cdot 10^{-9}$
51	$5s\ ^4P_{1/2}$	22.6830635	$2.4 \cdot 10^{-16}$	$2.6 \cdot 10^{-13}$	$8.4 \cdot 10^{-10}$
52	$5s\ ^2P_{3/2}$	22.7003765	$5.2 \cdot 10^{-16}$	$4.2 \cdot 10^{-13}$	$1.5 \cdot 10^{-9}$
53	$4d\ ^4D_{7/2}$	22.7728786	$1.4 \cdot 10^{-15}$	$10.0 \cdot 10^{-13}$	$6.5 \cdot 10^{-9}$
54	$4d\ ^4D_{5/2}$	22.7879772	$1.1 \cdot 10^{-15}$	$7.9 \cdot 10^{-13}$	$4.9 \cdot 10^{-9}$
55	$5s\ ^2P_{1/2}$	22.8025074	$3.8 \cdot 10^{-16}$	$4.1 \cdot 10^{-13}$	$1.2 \cdot 10^{-9}$
56	$4d\ ^4D_{3/2}$	22.8113575	$8.3 \cdot 10^{-16}$	$5.9 \cdot 10^{-13}$	$3.4 \cdot 10^{-9}$
57	$4d\ ^4D_{1/2}$	22.8368702	$5.6 \cdot 10^{-16}$	$4.1 \cdot 10^{-13}$	$2.0 \cdot 10^{-9}$
58	$4d\ ^4F_{9/2}$	22.9486465	$1.2 \cdot 10^{-15}$	$9.7 \cdot 10^{-13}$	$6.5 \cdot 10^{-9}$
59	$4d\ ^4F_{7/2}$	23.0145435	$1.6 \cdot 10^{-15}$	$9.5 \cdot 10^{-13}$	$5.1 \cdot 10^{-9}$
60	$4d\ ^4F_{5/2}$	23.0702877	$9.8 \cdot 10^{-16}$	$6.2 \cdot 10^{-13}$	$3.6 \cdot 10^{-9}$
61	$4d\ ^4P_{1/2}$	23.0823021	$4.1 \cdot 10^{-16}$	$3.7 \cdot 10^{-13}$	$1.7 \cdot 10^{-9}$
62	$4d\ ^4F_{3/2}$	23.1032829	$5.5 \cdot 10^{-16}$	$4.1 \cdot 10^{-13}$	$2.5 \cdot 10^{-9}$
63	$4d\ ^4P_{3/2}$	23.1193771	$6.3 \cdot 10^{-16}$	$4.9 \cdot 10^{-13}$	$2.7 \cdot 10^{-9}$
64	$4d\ ^2F_{7/2}$	23.1622372	$1.9 \cdot 10^{-15}$	$1.0 \cdot 10^{-12}$	$5.3 \cdot 10^{-9}$
65	$4d\ ^4P_{5/2}$	23.1715336	$7.8 \cdot 10^{-16}$	$6.0 \cdot 10^{-13}$	$3.6 \cdot 10^{-9}$
66	$4d\ ^2F_{5/2}$	23.2581120	$1.0 \cdot 10^{-15}$	$6.2 \cdot 10^{-13}$	$3.6 \cdot 10^{-9}$
67	$4d\ ^2P_{1/2}$	23.5488911	$3.3 \cdot 10^{-16}$	$2.5 \cdot 10^{-13}$	$1.2 \cdot 10^{-9}$
68	$4d\ ^2P_{3/2}$	23.6304226	$4.0 \cdot 10^{-16}$	$2.9 \cdot 10^{-13}$	$1.8 \cdot 10^{-9}$
69	$4p''\ ^2P_{3/2}$	23.8018131	$7.8 \cdot 10^{-15}$	$1.2 \cdot 10^{-11}$	$2.4 \cdot 10^{-8}$
70	$4p''\ ^2P_{1/2}$	23.8463135	$4.1 \cdot 10^{-15}$	$6.5 \cdot 10^{-12}$	$1.4 \cdot 10^{-8}$
71	$4d\ ^2D_{5/2}$	23.8740139	$4.4 \cdot 10^{-16}$	$3.2 \cdot 10^{-13}$	$2.0 \cdot 10^{-9}$
72	$4d\ ^2D_{3/2}$	23.8932476	$3.3 \cdot 10^{-16}$	$2.4 \cdot 10^{-13}$	$1.5 \cdot 10^{-9}$
73	$5s'\ ^2D_{5/2}$	24.2841301	$1.6 \cdot 10^{-16}$	$2.0 \cdot 10^{-13}$	$7.6 \cdot 10^{-10}$
74	$5s'\ ^2D_{3/2}$	24.2843933	$2.1 \cdot 10^{-16}$	$2.7 \cdot 10^{-13}$	$8.3 \cdot 10^{-10}$
75	$4d'\ ^2G_{7/2}$	24.6226406	$1.5 \cdot 10^{-16}$	$2.1 \cdot 10^{-13}$	$2.0 \cdot 10^{-9}$
76	$4d'\ ^2G_{9/2}$	24.6237736	$1.7 \cdot 10^{-16}$	$2.3 \cdot 10^{-13}$	$2.3 \cdot 10^{-9}$
77	$4d'\ ^2P_{1/2}$	24.7282295	$4.6 \cdot 10^{-16}$	$5.8 \cdot 10^{-13}$	$1.5 \cdot 10^{-9}$
78	$4d'\ ^2P_{3/2}$	24.7379761	$1.5 \cdot 10^{-16}$	$1.8 \cdot 10^{-13}$	$9.8 \cdot 10^{-10}$
79	$4d'\ ^2D_{5/2}$	24.7571430	$1.4 \cdot 10^{-16}$	$1.8 \cdot 10^{-13}$	$1.3 \cdot 10^{-9}$
80	$4d'\ ^2D_{3/2}$	24.7946091	$2.4 \cdot 10^{-16}$	$3.0 \cdot 10^{-13}$	$1.2 \cdot 10^{-9}$
81	$4d'\ ^2F_{7/2}$	24.8140640	$1.3 \cdot 10^{-16}$	$1.8 \cdot 10^{-13}$	$1.6 \cdot 10^{-9}$
82	$4d'\ ^2F_{5/2}$	24.8259697	$1.1 \cdot 10^{-16}$	$1.6 \cdot 10^{-13}$	$1.3 \cdot 10^{-9}$
83	Ar III $(3s^2 3p^4[^3P]_2)$	27.6296501	$8.2 \cdot 10^{-8}$	$8.3 \cdot 10^{-5}$	0.030

Table A.2: Continuation of Tab. A.1.

f	i	A_{if} [s^{-1}]	f	i	A_{if}[s^{-1}]	f	i	A_{if} [s^{-1}]	f	i	A_{if} [s^{-1}]
0	8	$3.1 \cdot 10^7$	10	48	$2 \cdot 10^5$	24	44	$3.7 \cdot 10^6$	36	59	$5.2 \cdot 10^6$
0	10	$2.3 \cdot 10^9$	10	33	$1.1 \cdot 10^7$	24	48	$5.7 \cdot 10^6$	36	56	$3.8 \cdot 10^6$
0	9	$3.8 \cdot 10^6$	10	30	$3.8 \cdot 10^4$	24	45	$2.1 \cdot 10^6$	36	54	$4.1 \cdot 10^6$
0	11	$9.5 \cdot 10^8$	10	45	$5.3 \cdot 10^7$	25	43	$2.1 \cdot 10^7$	36	52	$1.3 \cdot 10^8$
0	1	$5.3 \cdot 10^{-2}$	10	46	$1.8 \cdot 10^7$	25	41	$3.9 \cdot 10^5$	36	50	$2.1 \cdot 10^6$
0	2	$1.4 \cdot 10^8$	10	35	$6 \cdot 10^5$	25	48	$5.5 \cdot 10^6$	36	66	$3.7 \cdot 10^7$
1	11	$1.9 \cdot 10^9$	10	36	$8.2 \cdot 10^7$	25	47	$6.6 \cdot 10^7$	36	65	$2.6 \cdot 10^6$
1	10	$4.5 \cdot 10^8$	10	29	$7 \cdot 10^4$	25	46	$2.9 \cdot 10^7$	36	64	$2.9 \cdot 10^8$
1	9	$7.3 \cdot 10^6$	10	41	$2.1 \cdot 10^7$	25	45	$6.7 \cdot 10^6$	37	62	$4.7 \cdot 10^6$
1	2	$6.7 \cdot 10^7$	11	40	$3 \cdot 10^5$	26	48	$4.6 \cdot 10^7$	37	60	$2.1 \cdot 10^6$
1	8	$5.9 \cdot 10^6$	11	31	$4 \cdot 10^5$	26	47	$4.6 \cdot 10^6$	37	57	$7.5 \cdot 10^6$
3	36	$1.5 \cdot 10^6$	11	30	$2.1 \cdot 10^3$	26	45	$6.7 \cdot 10^6$	37	56	$1.1 \cdot 10^6$
3	33	$4.1 \cdot 10^6$	11	34	$2 \cdot 10^5$	26	44	$8.1 \cdot 10^6$	37	55	$9.9 \cdot 10^7$
3	29	$3 \cdot 10^7$	11	41	$8 \cdot 10^7$	26	43	$1.7 \cdot 10^6$	37	52	$3.6 \cdot 10^7$
3	32	$1.1 \cdot 10^7$	11	39	$6.4 \cdot 10^7$	27	44	$2 \cdot 10^7$	37	72	$1.5 \cdot 10^8$
4	36	$1 \cdot 10^6$	11	35	$1.6 \cdot 10^4$	28	43	$2 \cdot 10^7$	37	68	$4 \cdot 10^7$
4	30	$2.2 \cdot 10^7$	11	38	$1.9 \cdot 10^7$	28	44	$9 \cdot 10^5$	37	67	$3.7 \cdot 10^7$
4	39	$2 \cdot 10^5$	11	45	$9.9 \cdot 10^6$	29	64	$3 \cdot 10^5$	37	66	$3.4 \cdot 10^8$
4	29	$1.1 \cdot 10^7$	11	37	$3.9 \cdot 10^7$	29	63	$3.7 \cdot 10^7$	38	61	$1.1 \cdot 10^6$
4	32	$1.2 \cdot 10^6$	11	47	$8 \cdot 10^5$	29	62	$2.4 \cdot 10^7$	38	52	$2.6 \cdot 10^7$
4	37	$2 \cdot 10^5$	11	46	$4.2 \cdot 10^7$	29	60	$1.8 \cdot 10^6$	38	72	$2.3 \cdot 10^8$
4	40	$3 \cdot 10^5$	12	32	$1.5 \cdot 10^7$	29	65	$5.2 \cdot 10^7$	38	68	$5.2 \cdot 10^7$
4	33	$4.8 \cdot 10^6$	13	36	$3 \cdot 10^6$	29	56	$3.1 \cdot 10^7$	38	67	$3.4 \cdot 10^8$
4	34	$6.3 \cdot 10^6$	13	33	$1.1 \cdot 10^7$	29	54	$1.3 \cdot 10^8$	39	61	$1.5 \cdot 10^6$
5	29	$1.5 \cdot 10^6$	13	32	$9 \cdot 10^5$	29	53	$2.3 \cdot 10^8$	39	60	$6 \cdot 10^5$
5	35	$8.2 \cdot 10^6$	14	32	$1 \cdot 10^5$	29	50	$2.5 \cdot 10^7$	39	56	$1.8 \cdot 10^5$
5	36	$4 \cdot 10^5$	14	34	$1.4 \cdot 10^7$	29	49	$9.8 \cdot 10^7$	39	55	$6.9 \cdot 10^7$
5	31	$1.9 \cdot 10^7$	14	33	$2.5 \cdot 10^6$	30	63	$5.2 \cdot 10^6$	39	54	$2 \cdot 10^5$
5	40	$7 \cdot 10^4$	14	37	$1.2 \cdot 10^6$	30	62	$2.1 \cdot 10^6$	39	50	$7.7 \cdot 10^6$
5	37	$3 \cdot 10^5$	14	36	$6 \cdot 10^5$	30	61	$1.1 \cdot 10^8$	39	71	$4.4 \cdot 10^8$
5	33	$1.6 \cdot 10^6$	15	35	$1.7 \cdot 10^7$	30	60	$9 \cdot 10^5$	39	68	$1.7 \cdot 10^8$
5	34	$3.7 \cdot 10^6$	15	34	$2 \cdot 10^6$	30	56	$1.8 \cdot 10^8$	39	67	$4.1 \cdot 10^7$
5	30	$1.6 \cdot 10^7$	15	37	$2 \cdot 10^5$	30	54	$1.4 \cdot 10^8$	39	66	$2.3 \cdot 10^7$
6	34	$2 \cdot 10^6$	15	33	$2 \cdot 10^5$	30	51	$6.4 \cdot 10^7$	40	63	$9.3 \cdot 10^7$
6	38	$2 \cdot 10^5$	15	36	$1 \cdot 10^4$	30	50	$1.7 \cdot 10^7$	40	62	$2.1 \cdot 10^7$
6	30	$3.1 \cdot 10^6$	15	41	$2 \cdot 10^5$	30	49	$4.4 \cdot 10^7$	40	61	$9.8 \cdot 10^7$
6	31	$2.1 \cdot 10^7$	16	41	$1.7 \cdot 10^6$	30	65	$4.9 \cdot 10^7$	40	56	$1.8 \cdot 10^5$
6	37	$1 \cdot 10^5$	16	40	$1 \cdot 10^5$	31	63	$6.3 \cdot 10^7$	40	54	$6 \cdot 10^5$
6	35	$4.3 \cdot 10^6$	16	39	$2 \cdot 10^5$	31	62	$1.5 \cdot 10^7$	40	52	$7.4 \cdot 10^6$

Table A.3: Einstein coefficients for spontaneous emission according to [53]

f	i	A_{if} [s^{-1}]	f	i	A_{if}[s^{-1}]	f	i	A_{if} [s^{-1}]	f	i	A_{if} [s^{-1}]
7	36	$2.9 \cdot 10^6$	16	38	$8.8 \cdot 10^6$	31	61	$4.2 \cdot 10^7$	40	51	$2.9 \cdot 10^7$
7	34	$1.2 \cdot 10^6$	16	37	$7 \cdot 10^5$	31	57	$2.6 \cdot 10^8$	40	50	$1.5 \cdot 10^7$
7	40	$4.8 \cdot 10^7$	16	46	$5 \cdot 10^6$	31	56	$5.7 \cdot 10^7$	40	49	$1.5 \cdot 10^7$
7	30	$5.8 \cdot 10^7$	16	45	$9 \cdot 10^5$	31	52	$1.2 \cdot 10^7$	40	65	$1.4 \cdot 10^8$
7	33	$1.6 \cdot 10^7$	17	41	$1.1 \cdot 10^7$	31	51	$1.3 \cdot 10^7$	41	72	$1.8 \cdot 10^8$
7	29	$7.8 \cdot 10^7$	17	40	$3 \cdot 10^5$	31	50	$4.1 \cdot 10^7$	41	68	$1.9 \cdot 10^8$
7	37	$9 \cdot 10^5$	17	39	$2.4 \cdot 10^6$	32	60	$3 \cdot 10^6$	42	70	$1.6 \cdot 10^8$
7	39	$1.6 \cdot 10^6$	17	38	$5 \cdot 10^5$	32	59	$2.3 \cdot 10^7$	42	69	$6.7 \cdot 10^7$
7	32	$1.2 \cdot 10^8$	17	47	$6 \cdot 10^5$	32	58	$3 \cdot 10^8$	43	82	$1.5 \cdot 10^8$
7	44	$2 \cdot 10^5$	17	46	$1.7 \cdot 10^6$	32	54	$1.8 \cdot 10^7$	43	81	$3.9 \cdot 10^6$
8	30	$1.4 \cdot 10^7$	17	48	$4.4 \cdot 10^6$	32	53	$7.7 \cdot 10^7$	43	80	$3.2 \cdot 10^7$
8	35	$1.3 \cdot 10^7$	17	45	$7.4 \cdot 10^6$	32	49	$1.2 \cdot 10^8$	43	79	$7.7 \cdot 10^6$
8	37	$1.1 \cdot 10^6$	17	43	$4 \cdot 10^5$	32	65	$5.9 \cdot 10^6$	43	75	$3.9 \cdot 10^8$
8	31	$8.5 \cdot 10^7$	18	40	$3.7 \cdot 10^6$	32	64	$2 \cdot 10^6$	43	74	$1.4 \cdot 10^8$
8	40	$3.9 \cdot 10^7$	18	45	$6 \cdot 10^5$	33	64	$6.2 \cdot 10^6$	44	82	$1.3 \cdot 10^7$
8	33	$8.2 \cdot 10^7$	18	35	$6 \cdot 10^5$	33	62	$2.7 \cdot 10^6$	44	81	$1.5 \cdot 10^8$
8	39	$2 \cdot 10^6$	19	41	$2 \cdot 10^5$	33	60	$5.2 \cdot 10^7$	44	79	$2.2 \cdot 10^7$
8	34	$5.7 \cdot 10^7$	19	35	$4.5 \cdot 10^5$	33	59	$2.8 \cdot 10^8$	44	76	$4 \cdot 10^8$
8	41	$3 \cdot 10^5$	19	40	$5.6 \cdot 10^6$	33	56	$1.7 \cdot 10^7$	44	75	$1.5 \cdot 10^7$
8	29	$1.5 \cdot 10^7$	19	45	$1.6 \cdot 10^6$	33	54	$2.8 \cdot 10^7$	44	73	$1.4 \cdot 10^8$
8	45	$5 \cdot 10^5$	20	40	$1.1 \cdot 10^7$	33	53	$4.8 \cdot 10^6$	45	79	$1.4 \cdot 10^8$
8	38	$3.2 \cdot 10^3$	20	48	$1 \cdot 10^5$	33	49	$1.3 \cdot 10^7$	45	78	$2.2 \cdot 10^8$
8	36	$1.3 \cdot 10^7$	20	44	$6.1 \cdot 10^6$	33	65	$9.3 \cdot 10^6$	45	77	$7.1 \cdot 10^7$
9	37	$2.1 \cdot 10^6$	21	41	$9 \cdot 10^5$	34	62	$8.7 \cdot 10^7$	45	73	$4.1 \cdot 10^7$
9	31	$9.7 \cdot 10^6$	21	48	$4.4 \cdot 10^6$	34	60	$2.5 \cdot 10^8$	46	80	$1.2 \cdot 10^8$
9	35	$1 \cdot 10^8$	21	47	$4.1 \cdot 10^7$	34	57	$2.7 \cdot 10^7$	46	74	$3.4 \cdot 10^7$
9	39	$2 \cdot 10^4$	21	46	$8.5 \cdot 10^7$	34	56	$1.5 \cdot 10^7$	47	82	$2 \cdot 10^8$
9	40	$2.4 \cdot 10^7$	21	45	$1.1 \cdot 10^7$	34	54	$7.2 \cdot 10^6$	47	79	$2.5 \cdot 10^7$
9	38	$1.8 \cdot 10^4$	21	43	$6.6 \cdot 10^7$	34	52	$3.1 \cdot 10^6$	47	78	$3.6 \cdot 10^5$
9	41	$3 \cdot 10^5$	22	43	$7.1 \cdot 10^6$	34	51	$9.8 \cdot 10^7$	48	82	$3.4 \cdot 10^7$
9	30	$2.2 \cdot 10^7$	22	69	$1.4 \cdot 10^7$	34	50	$3.9 \cdot 10^7$	48	81	$2.3 \cdot 10^8$
9	34	$5.7 \cdot 10^7$	22	48	$5.8 \cdot 10^7$	34	66	$2.7 \cdot 10^6$	48	79	$1.5 \cdot 10^8$
10	39	$4.7 \cdot 10^7$	22	47	$1.2 \cdot 10^7$	35	63	$5.5 \cdot 10^7$	48	78	$7.6 \cdot 10^7$
10	34	$1.1 \cdot 10^6$	22	45	$8 \cdot 10^7$	35	62	$1.8 \cdot 10^8$	48	73	$6.5 \cdot 10^7$
10	31	$4 \cdot 10^5$	22	44	$7.9 \cdot 10^7$	35	61	$6.5 \cdot 10^6$			
10	40	$1.1 \cdot 10^6$	23	48	$1.4 \cdot 10^6$	35	57	$2.3 \cdot 10^7$			
10	47	$3 \cdot 10^5$	23	44	$8 \cdot 10^5$	35	56	$7.7 \cdot 10^6$			
10	38	$8.9 \cdot 10^7$	23	43	$5 \cdot 10^5$	35	51	$8 \cdot 10^7$			
10	37	$5.9 \cdot 10^7$	24	43	$7 \cdot 10^5$	36	60	$7.6 \cdot 10^6$			

Table A.4: Continuation of Tab. A.3

λ [nm]	u_{IS} [mW/(cm^2 sr μm)]		λ [nm]	u_{IS} [mW/(cm^2 sr μm)]
0.300	0.24		0.800	102.20
0.310	0.39		0.900	102.40
0.320	0.62		1.050	97.70
0.330	0.92		1.150	86.60
0.340	1.30		1.200	79.50
0.350	1.77		1.300	69.20
0.400	6.50		1.540	35.40
0.450	15.55		1.600	33.30
0.500	28.70		1.700	29.60
0.555	45.60		2.000	10.59
0.600	60.10		2.100	9.05
0.655	76.10		2.300	6.09
0.700	87.40		2.400	4.97

Table A.6: Spectral radiance of the integrating sphere USS 1200, labsphere.

i	$\sum$A [s^{-1}] (M1)	$\sum$A [s^{-1}] (E2)	τ [s]
12	$3.135{\cdot}10^{-2}$	$1.984{\cdot}10^{-1}$	4.35
13	$2.455{\cdot}10^{-2}$	$2.000{\cdot}10^{-1}$	4.45
23	$8.386{\cdot}10^{-2}$	$7.173{\cdot}10^{-1}$	1.25
28	$1.304{\cdot}10^{-1}$	$3.343{\cdot}10^{-2}$	6.10
27	$1.812{\cdot}10^{-1}$	$2.291{\cdot}10^{-2}$	4.90

Table A.5: Total magnetic dipole (M1) and electric quadrupole (E2) rate coefficients of selected metastable levels according to Schef *et al.* [51]

Appendix B

Checklist for LIF measurements

- **Adjust the optics well**: Do not cherish the illusion to find the LIF signal just by trying. Scanning the detector position (two dimensions) and the laser wavelength (one dimension) takes too much time. Use a Langmuir probe or any other object to adjust the excitation and the detection volume. To do so it is very helpful to place a lamp at the position where the photomultiplier is located. When adjusting the laser wavelength use an emission spectrum from the plasma as reference. Note that narrow band width interference filters are very sensitive to the incidence angle of the light. As such the incidence angle must be well adjusted. Due to this effect a lot of photons are lost, if the filter is too close to the lens.

- **Choose the right plasma volume**: Search the LIF signal in a plasma region where most of the light originates from the detection volume. For PSI-2 Fig. 2.7 shows very clearly that it is much more favorable to measure at the hot and dense edge of the plasma column than in the center.

- **Use a good detection optics**: If aberration errors are large it is very difficult to find the LIF signal.

- **Avoid ground loops**: Lock-in-amplifiers are *very* sensitive instruments. A mass loop can very easily act as an antenna collecting the modulation signal even if the signal generator is far away from the amplifier. In some cases it is also very helpful to use BNC cables wrapped around a ring core in order to damp these signals.

- **Measure the laser wavelength relative to a stable reference line**: In order to measure quantitatively the very small Doppler shift

of the ions moving in the plasma it is necessary to know the wavelength of the laser very accurately. Even drifts of the refractive index of the air due to atmospheric pressure and/or temperature changes play an important role.

- **Minimize the Zeeman splitting/broadening** As shown in Fig. 3.6 (for the present conditions) the Zeeman effect starts to play an important role for magnetic fields around 90 mT. If the experimental constraints allow so, it might be favorable to measure at a lower magnetic field.

- **Choose an integration time at least 10 times larger than the time constant of the LIA**: If the integration time (the time where the laser wavelength is kept constant) is shorter than 10 times the time constant of the Lock-in-amplifier, stationarity is not reached and a systematic error can effect the evaluation of the ivdf.

Danksagung

An dieser Stelle möchte ich mich bei allen herzlich bedanken, die mich bei der Anfertigung dieser Arbeit unterstützt haben und meine Wertschätzung dem gegenüber zum Ausdruck bringen, was ich in meinem Arbeitsumfeld vorgefunden habe. Ich denke, dass ich trotz des bevorstehenden Umzuges der Arbeitsgruppe an eine andere Berliner Universität gute Voraussetzungen für die Durchführung der Experimente aber auch für deren wissenschaftliche Diskussion hatte.
Zunächst gilt mein Dank Prof. Dr. G. Fußmann, der diese Arbeit betreut hat. Er stand mir mit seiner lebenslangen Erfahrung auf dem Gebiet der Plasmaphysik stets mit Rat zur Seite, gab mir in den zahlreichen wissenschaftlichen Diskussionen viele Anregungen und orientierte mich bei der thematischen Schwerpunktsetzung meiner Dissertation.
Herrn Dr. Bohmeyer möchte ich für die Leitung der PSI-2 Gruppe danken. Nicht nur von der experimentellen, sondern auch von der menschlichen Seite sehe ich ihn dazu in besonderem Maße befähigt. Es gelingt ihm sehr gut die Experimente zu koordinieren und gleichzeitig den Arbeitsalltag auf eine gewisse humorvolle Basis zu stellen, was diesen – auch wenn man dabei natürlich so manche 'Pfeilspitze' einzustecken hat – ungemein viel erträglicher macht.
Vermutlich gerät jeder Doktorand mindestens einmal in die Situation, in der die Promotion in unerreichbare Ferne zu rücken scheint. Für mich gab es eine solche Situation, als auch nach monatelangem intensiven Justierens und Probierens es nicht gelungen war, das LIF Signal eindeutig nachzuweisen und dann auch noch mein wichtigstes Messgerät kaputt ging. An dieser Stelle möchte ich meinen ausdrücklichen Dank an Herrn Mans zum Ausdruck bringen, der das Kunststück vollbracht hat, das Gerät innerhalb weniger Tage wieder zu reparieren. In Situationen wie der geschilderten, wird einem bewusst, wie wichtig es ist, von gutem technischen Personal unterstützt zu werden, wozu ich auch unseren Feinmechaniker Herrn Mettchen zähle.
Trotz seines Engagements ist natürlich der Hunger der Experimentatoren nach neuen Apparaturen und Aufbauten schwer zu stillen und so habe ich

mich auch bei der mechanischen Werkstatt der Humboldt-Universität unter der Leitung von Herrn Rausche zu bedanken, die ebenfalls viele Aufgaben übernommen hat.
Meinen Doktorandenkollegen Ole Waldmann und Mandy Baudach danke ich für ihre Bereitschaft, den einen oder anderen Tag lang werden zu lassen, was mir ermöglichte, die Messperioden voll auszunutzen. Bernd Koch bin ich sehr für die intensive Auseinandersetzung mit meiner Arbeit verbunden, die mir noch einige kritische Punkte aufgezeigt hat.
Mein Dank reicht allerdings auch über dieses Institut hinaus, wenn ich diesen an Dr. Albrecht Stark aus Greifswald richte. Von seinen Aufbauten, die er mir bereitwillig und offen gezeigt und erklärt hat, konnte ich für meine eigenen selbst viel lernen.

For the good collaboration on the current-force probe I would like to thank in particular my collegues Dr. Hidalgo and Dr. Pedrosa from Ciemat in Madrid and Dr. Silva and Dr. Fernandes from IST in Lisbon. My six-months sojourn at the Ciemat was funded by the Deutscher Akademischer Austausch Dienst (DAAD). Last but not least I thank Caroline Faria for English-proofreading.

Selbständigkeitserklärung

Hiermit erkläre ich, die vorliegende Arbeit selbständig ohne fremde Hilfe verfaßt und nur die angegebene Literatur und Hilfsmittel verwendet zu haben.

Tilmann Lunt
Berlin, den 14.02.2008